Organometallic Synthesis of Nanomaterials for Catalytic Carbon Dioxide Conversion

Lisa Häfele

Trinity College

Department of Inorganic Chemistry

University of Oxford

March 2022

A thesis submitted in partial fulfilment of the requirements for the degree of Doctor of Philosophy in Chemistry

DECLARATION

The work described in this thesis was conducted between October 2018 and March 2022 at the University of Oxford. This is the work of the author unless otherwise stated.

Lisa Häfele

ABSTRACT

This thesis investigates a series of organometallic reactions to produce colloidal nanoparticles (Cu and Cu_2O) and layered metal hydroxides (Zn or Cu). The general synthesis involves reacting an organometallic precursor, with a ligand (e.g. a carboxylic acid) and either exposure to hydrogen gas, water or air. The synthesis occurs in organic solvents at temperatures from room temperature to 110 °C. These reactions produce nanomaterials which are soluble in various organic solvents.

Chapter 1: The first chapter introduces the research topics of this thesis by outlining the relevant literature. The characteristics and properties of nanomaterials are described, alongside their roles in various catalyses, with a focus on carbon dioxide utilisation.

Chapter 2: This chapter describes the synthesis and characterisation of colloidal Cu and Cu_2O nanoparticles, capped with oxygen-containing anionic, bidentate carboxylate ligands (i.e. nonanoate, 2-[2-(2-methoxyethoxy)ethoxy]acetate) or a sulphur-containing anionic, bidentate dithicarboxylate ligand (i.e. dithiononanoate). The effects of ligand substituents on the solubility and stability of the resulting nanoparticles in common organic solvents (toluene, THF, acetone and methanol), as well as their ease of removal from the particle surface by thermal ligand degradation was evaluated. Ligand exchange reactivity of the carboxylate and dithiocarboxylate ligands is probed to evaluate the relationship between colloidal nanoparticle stability and ligand binding-group identity. This research provides understanding of the conditions required for colloidal nanoparticle synthesis and a means to make colloidal inks for solution-phase thin film deposition.

Chapter 3: This chapter will describe efforts to synthesise a hydrotalcite-like catalyst precursor for the conversion of CO_2 to methanol. Efforts to isolate copper-containing Layered Metal Hydroxides (LMH) *via* the controlled hydrolysis of organometallic precursors is discussed. The synthesis routes tested thus far have been unsuccessful leading to separated phases over the copper-based material.

Chapter 4: This chapter describes the use of colloidal Layered Zinc Hydroxides (LZH) as a novel catalytic stystem for the ring opening copolymerisation (ROCOP) of propylene oxide (PO) and CO_2 to

provide polypropylene carbonate (PPC). The synthesis and characterisation of the catalysts is outlined. Then the catalytic performance, under varying temperatures, pressures and catalyst loading, is discussed.

Chapter 5: This chapter summarises the results and outlines various future directions for this research.

Chapter 6: The final chapter details the experimental protocols and methods used to produce and characterise the products.

ACKNOWLEDGEMENTS

First, I would like to thank my first supervisor, Professor Charlotte Williams, for warmly welcoming me to her research group and allowing me the opportunity carrying out my DPhil. Many thanks also to Professor Milo S. P. Shaffer at Imperial College London who supported me on this journey as my second supervisor. I am deeply grateful for both of their motivation, insight and support. Many thanks.

I would also like to take this opportunity to acknowledge the researchers who have lent their expertise in data collection including: Dr Anna Regoutz (University College London), Floriana Moruzzi (University of Oxford), David M. Stringer (Imperial College of London).

Furthermore, I'd like to extend my thanks to all past and present group members at the Williams group, who contributed to my research and made working in the Williams Lab a great experience. A special thanks to Brad, Said, Arron and George.

I also want to thank my friends for their companionship, unfailing support, and continuous encouragement throughout my years of study.

Moreover, I want to express my gratitude towards my family for their untiring support, especially during difficult times. This accomplishment would not have been possible without them.

Lastly, I would like to thank Shell Global for financially sponsoring this work.

PUBLICATIONS

Colloidal Cu, Cu_2O and Cu_2S Nanoparticles via an Organometallic Route, and an Investigation into the Relationship Between Ligand Identity and Colloidal Stability

Bradley E. Cowie, Lisa Häfele, Said A. Said, Ja Kyung Lee, Anna Regoutz, Andreas Phanopoulos, Milo S. P. Shaffer, Charlotte K. Williams, *manuscript in preparation*

Layered Zinc Hydroxides for the Ring-Opening Copolymerisation of CO_2 and Propylene Oxide

Lisa Häfele, Arron C. Deacy, Sumesh K. Raman, Charlotte K. Williams, *manuscript in preparation*

LIST OF ABBREVIATIONS

$[L_1^{O2}]^-$	Nonanoate
$[L_1^{S2}]^-$	Dithiononanoate
$[L_2^{O2}]^-$	2-[2-(2-methoxyethoxy)ethoxy]acetate
$[L_3^{O2}]^-$	Oleate
$[L_4^{O2}]^-$	2-(2-methoxyethoxy)acetate
$[L_5^{O2}]^-$	Hexanoate
0D	Zero-dimensional
1D	One-dimensional
2D	Two-dimensional
3D	Three-dimensional
Å	Angström
ALD	Atomic Layer Deposition
asym.	Asymmetric
CB	Conduction band
CCS	Carbon Capture and Storage
CCU	Carbon Capture and Utilisation
cm	Centimetre
CVD	Chemical Vapour Deposition
Đ	Dispersity
D	Particle size using Scherrer equation
d_{Cu}	Average Cu particle size
D_{Cu}	Copper dispersion
DMC	Double Metal Cyanide
E	Half-cell redox potential
e.g.	Exempli gratia
EDX	Energy-Dispersive X-ray Spectroscopy
E_F	Fermi level
E_g	Band gap
equiv.	Equivalent
eV	Electronvolt
fcc	Face-centred cubic
FFT	Fast Fourier Transformation
FT-IR	Fourier-Transform Infrared Spectroscopy
g	Gram
G = GHSV	Volume flow rate/bed volume
GPC	Gel Permeation Chromatography
Gt	Gigaton
h	Hours
HH	Head to Head
HL_1^{O2}	Nonanoic acid
HL_1^{S2}	Dithiononanoic acid
HL_2^{O2}	2-[2-(2-methoxyethoxy)ethoxy]acetic acid
HL_3^{O2}	Oleic acid
HL_4^{O2}	2-(2-methoxyethoxy)acetic acid
HL_5^{O2}	Hexanoic acid
HOMO	Highest Occupied Molecular Orbital
HPLC-grade	High Performance Liquid Chromatography grade
HSAB	Hard and Soft Acids and Bases
HT	Head to Tail

htl	Hydrotalcite-like
ICP-MS	Inductively Coupled Plasma Mass Spectrometry
kcal	Kilocalories
kg	kilogram
L	Ligand
LED	Light Emitting Diode
LMH	Layered Metal Hydroxides
LSH	Layered Single Metal Hydroxides
LUMO	Lowest Unoccupied Molecular Orbital
LZH	Layered Zinc Hydroxides
M	Molar
MEA	Monoethanolamine
Mes	1,3,5-Trimethylbenzene
mL	Millilitre
mM	Millimolar
M_n	Number average molar mass
Mt	Megaton
n.d	Not determined
NHE	Normal Hydrogen Electrode
nm	Nanometre
NMR	Nuclear Magnetic Resonance
Nº	Number
NP	Nanoparticle
~~θ~~	Oxophilicity
p	Pressure
PC	Propylene Carbonate
pm	Picometre
PO	Propylene oxide
PO	Propylene oxide
PPC	Poly(propylene carbonate)
PPC	Poly(propylene carbonate)
ppm	Parts per million
PVD	Physical Vapour Deposition
pXRD	Powder X-ray Diffraction
r	Radius
Ref.	Reference
ROCOP	Ring Opening Copolymerisation
rpm	Rounds per minute
RWGS	Reverse Water Gas Shift
~~ζ~~	Thiophilicity
SCXRD	Single Crystal X-ray Diffraction
SEM	Scanning Electron Microscope
SPR	Surface Plasmon Resonance
STY	Space Time Yield
SWCNT	Single Walled Carbon Nanotubes
sym.	Symmetric
T	Temperature
$T_{d,5\%}$	Degradation temperature (5% mass loss)
TEM	Transmission electron microscopy
T_g	Glass-transition temperature
TGA	Thermal Gravimetric Analysis
THF	Tetrahydrofuran

TOF	Turnover frequency
TT	Tail to Tail
UV-Vis	UltraViolet-Visible Spectroscopy
V	Volt
VB	Valence band
W = WHSV	Mass flow rate/catalyst mass
wt.	Weight
XPS	X-ray Photoelectron Spectroscopy
ZnGA	Zinc glutarate
δ_{Cu}	Copper surface area
ν	Frequenz

LIST OF FIGURES, SCHEMES AND TABLES

Chapter 1: Introduction

Figure 2.17 A) Powder XRD pattern of isolated precipitate formed when stirring Cu@L_1^{S2} in air overnight. Indexed against Cu_2O as vertical bars (JCPDS card no.: 00-002-1067). B) Stacked FT-IR spectra: a) HL_1^{S2} and b) isolated precipitate.

Figure 2.18 Ligand exchange reactivity on the surface of Cu (1., top) and Cu_2O nanoparticles (2., bottom).

Figure 2.19 A) Superimposed UV-Vis spectra of Cu@$(L_1^{X2})_{0.1}$ (X = O or S), Cu@$(L_1^{O2})_{0.1}$ + 0.1 equiv. HL_1^{S2} and Cu@$(L_1^{S2})_{0.1}$ + 0.1 equiv. HL_1^{O2} B) Stacked FT-IR spectra of a) Cu@$(L_1^{O2})_{0.1}$, b) Cu@$(L_1^{S2})_{0.1}$, c) Cu@$(L_1^{S2})_{0.1}$ + 0.1 equiv. HL_1^{O2}, d) Cu@$(L_1^{O2})_{0.1}$ + 0.1 equiv. HL_1^{S2}.

Figure 2.20 A) UV-Vis spectrum of Cu@$(L_1^{S2})_{0.1}$ + 0.5 equiv. HL_1^{O2}. B) Stacked FT-IR spectra of: a) Cu@$(L_1^{S2})_{0.1}$ + 0.1 equiv. HL_1^{O2} and b) Cu@$(L_1^{S2})_{0.1}$ + 0.5 equiv. HL_1^{O2}.

Figure 2.21 FT-IR spectra of Cu_2O@$(L_1^{O2})_{0.1}$ (top) and Cu_2O@$(L_1^{O2})_{0.1}$ + 0.1 equiv. HL_1^{S2} (bottom).

Figure 2.22 Solubility of Cu_2O nanoparticles coordinated by 0.1 equiv. L_n^{O2} (n = 1 or 2) in various organic solvents [g/mL].

Figure 2.23 Powder X-ray diffraction of Cu_2O nanoparticles. A) Cu_2O@L_2^{O2} (top) and Cu_2O@L_1^{O2} (bottom) from THF, B) Cu_2O@L_2^{O2} from acetone, and C) Cu_2O@L_2^{O2} from methanol. Indexed against Cu_2O as vertical bars (JCPDS card no.: 00-002-1067).

Scheme 2.4 Simplified formation of electrons (–) and holes (+) via photonic excitation (sun) of a nanoparticle (oval, grey). Table showing products and half-cell redox potential (E) that occurs during CO_2 reduction at pH 7. Picture of reaction cell used for photocatalytic testing under irradiation (left). Preliminary results for photocatalytic testing of Cu_2O@L_2^{O2} and Cu_2O nanoparticles in comparison to standard P25 TiO_2. Data collected by Floriana Moruzzi, Dr Ludmilla Steier Group (right).

Scheme 2.5 Using Cu_2O NPs as co-catalysts in photocatalytic organic single semi-conducting polymers, such as p(^{t}Bu)TA-Ph (band gap 2.72 eV with HOMO at -5.64 eV and LUMO at -2.92 eV).

Figure 3.5 The reaction mixture of $ZnEt_2$, $AlEt_3$ and HL_4^{O2} were found to form a mixture of very small crystalline particles of ZnO@L_4^{O2} NPs alongside amorphous Al_2O_3@L_4^{O2}. The synthesis of ZnAl LDH-L_4^{O2} was not achieved. (i) Toluene, 25 °C, 16 h, (ii) H_2O, 25 °C, 3 h. HL_4^{O2} = 2-(2-methoxyethoxy)acetic acid and L_4^{O2} = 2-(2-methoxyethoxy)acetate.

Scheme 3.3 Overview of the synthetic routes to Cu(I) or Cu(II) doped LZHs ($Cu^m{}_xLZH\text{-}R_n$ with m = I or II). (i) Toluene, room temperature, overnight (ii) H_2O, room temperature, overnight.

Scheme 3.4 Synthesis of CuMes from mesitylbromide. (i) Mg, Tetrahydrofuran, room temperature, 4 h; (ii) CuCl, Tetrahydrofuran, –20 °C – room temperature.

Scheme 3.5 Synthesis of bis(oleate)copper. (i) Ethanol, 50 °C; (ii) $CuCl_2$, H_2O; (iii) Toluene, 120 °C, 5 h. HL_3^{O2} = oleic acid and $[L_3^{O2}]^-$ = oleate.

Scheme 3.6 Syntheses of zinc carboxylates. A) First attempt to synthesise bis(2-(2-methoxyethoxy)acetyl)zinc ($Zn(L_4^{O2})_2$), following a modified literature procedure to bis(oleate)zinc[14] B) Second attempt to synthesise $Zn(L_4^{O2})_2$, following a modified literature protocol for preparing bis(hexanoate)zinc[15] C) Synthesis of bis(oleate)zinc (($Zn(L_3^{O2})_2$) according to Ref.[14] . i) 1 h, 60 °C, Ethanol, ii) $ZnCl_2$ in H_2O, and B iii) H_2O, iv) n-Octane or Toluene, reflux, 2 h, v) ethanol, 50 °C, vi) $ZnCl_2$, H_2O HL_3^{O2} = oleic acid; HL_4^{O2} = bis(2-(2-methoxyethoxy)acetic acid.

Figure 3.6 ^1H NMR spectrum of (2-(2-methoxyethoxy)acetic acid, HL_4^{O2}, in $CDCl_3$ (bottom) and bis(2-(2-methoxyethoxy)acetyl)zinc, $Zn(L_4^{O2})_2$, from dichloromethane extraction (top).

Scheme 3.7 Two step synthesis of $ZnMes_2$.

Figure 3.7 X-ray crystal structure of $ZnMes_2$ (Structure measured and analysed by Dr Andreas Phanopoulos). In line with associated bond lengths and angles reported to the literature.

Figure 3.8 Powder X-ray diffraction pattern of LZH-L_3^{O2} synthesised from $ZnEt_2$ (bottom) and from $ZnMes_2$ (top).

Chapter 4: Novel Catalysts for CO_2/PO Ring Opening Copolymerisation

Figure 6.1 Representative example of crude ^{1}H NMR spectrum of a typical PO-CO_2 ring opening copolymerisation formation both poly(carbonate ether) and propylene carbonate. Mesitylene is used as an internal standard.

TABLE OF CONTENTS

Chapter 1:

Literature Review

1 LITERATURE REVIEW

1.1 NANOTECHNOLOGY

"There's Plenty of Room at the Bottom" [1]

In 1959, Richard Feynman outlined the ideas and concepts of miniaturization to the atomic and nanoscale.[1] His lecture is considered as the founding document of nanoscience and ever since there has been a growing effort on the scientific front to conduct research at the nanoscale.

The term "nanotechnology" was defined over a decade later by Taniguchi, describing the development and study of matter with at least one dimension sized from 1 to 100 nm.[2] At these size ranges chemical and physical properties are unique and the 'quantum size effect', in which the electronic properties of solids change with reduction in particle size, becomes relevant.[3]

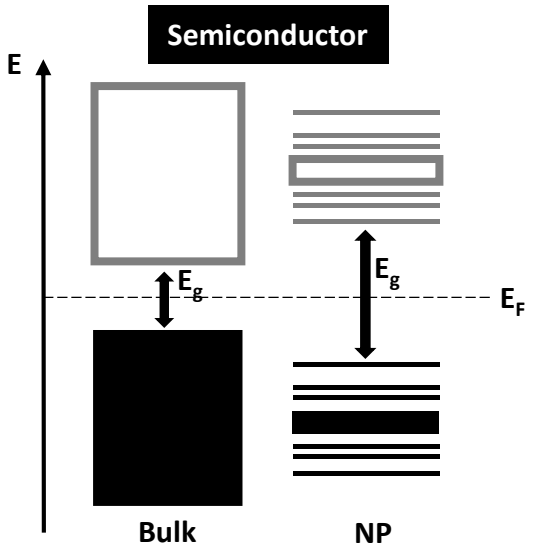

Figure 1.1. Illustration of the increase in band gap (E_g) from a bulk semiconductor to a nanoparticle semiconductor. E_F = fermi level.[4]

The phenomenon is observed in semiconductor crystals that are smaller than the exciton Bohr radius as electronic states become discrete at the edges of the band structure with decreasing particle size.[5] In addition, the separation between the energy levels, known as the bandgap (E_g), increases with

decreasing particle sizes.[3] Consequently, optical properties of a nanoparticle can be fine-tuned by its particle size, which is a beneficial characteristic for the design of efficient photocatalytic systems.

Another important property of nanoparticulate materials is the large surface-area-to-volume ratio in comparison to bulk material. This is of particular interest for the design of catalysts as an increase in total surface area may improve the rate of chemical reactivity due to more accessible catalytic active sites .[6] Therefore, it is not surprising that nanoscaled materials are widely used in catalysis.[7]

The synthesis of materials at the nanoscale can be achieved by either top-down or bottom-up approaches. The top-down approach is a process which entails starting from bulk materials and breaking them down into smaller particles.[4] Commonly used techniques for this approach are lithography and ball milling.[8] Major infrastructures, clean rooms and vacuum environments are often required, making this approach technologically and economically challenging.[4] Moreover, defects may be introduced during the processing due to significant crystal damage.[4] In contrast, the bottom-up approach forms complex nanostructures by assembling atoms or molecules together, potentially enabling the fabrication of nanoparticles with fewer defects, higher homogeneous chemical compositions and better short- and long-range ordering.[4] Low costs, high throughput and the possibility of large-scale industrial syntheses are further advantages of the bottom-up approach.[4] A wide variety of synthetic techniques may be deployed for this approach, such as co-precipitation, sol-gel processes, solvothermal processes, physical vapour deposition, and chemical vapour deposition.[4] The advantages are better control over size, morphology and uniformity of the nanomaterials.[4] Solution-based chemical routes are of particular interest as specific architectures and properties can be obtained by controlling the reaction temperature, concentration and chemical interaction (Coulombic and potentially Van der Waals).[4,9]

Depending on the dimensionality, shape and chemical composition of nanomaterials they are classified into four groups:[10,11] (1) zero-dimensional nanomaterials (0D), which are sized below 100 nm in all dimensions and consist of nanoparticles (solid, hollow or core-shell), clusters or quantum dots,[8,10] (2) one-dimensional nanomaterials (1D), which are nanoscaled in two dimensions but show sizes

beyond 100 nm in the third dimension; ceramics, nanotubes, nanorods and nanowires,[8,10] and (3) two-dimensional nanomaterials (2D), which are nanoscaled in their thickness only;[8] examples include single- and multi-layered thin films and nanoplates.[10] (4) Three-dimensional materials (3D) comprise of multiple nanomaterials forming composite structures with one phase in the nanometre regime and the others with various dimensions larger than 100 nm.[10]

1.2 (GREEN) NANOTECHNOLOGY AS A TOOL FOR A SUSTAINABLE FUTURE

According to the International Energy Agency (IEA), 33.0 Gt of CO_2 were emitted into the earth's atmosphere during 2021.[12] The record high was reached in 2018 with an emission of 33.5 Gt of CO_2 which strongly contributes to the current global warming crisis. The generation of heat and electricity was identified as the main source of CO_2 emissions and assigned across all sectors; industry, responsible for nearly 40 % of the global CO_2 emissions, is the largest producer.[12] The latest data for the first half of 2020 shows a decrease of 8.8 % in global CO_2 emissions (–1551 Mt CO_2) in contrast to the same period in 2019 as a result of newly implemented governmental policies during COVID-19 pandemic.[13] However, economic downturn is not a sustainable strategy for reducing CO_2 emission as it creates numerous other economic and social problems.[14,15] One important future technology need is to develop methods to transform CO_2 to valuable products.

1.2.1 CARBON CAPTURE & STORAGE (CCS)/UTILISATION (CCU)

Carbon capture and storage (CCS) is the process of catching and storing waste CO_2 released from industrial plants in order to prevent its emission into the atmosphere and thus its contribution to climate change.[16] At present, industry primarily uses monoethanolamine (MEA) based solvents in columns for CO_2 capture.[16,17] The most well-developed approach to store CO_2 is injecting it into empty oil and gas reservoirs, porous geological formations or saline aquifers.[18] However, the field struggles with meeting the growing demand for CO_2 capture and storage while making it economically profitable. As a result, energy systems with greater efficiency are currently under exploration. Nanomaterials have attracted enormous attention in this field due to their outstanding high active surface area, and their cost-efficiency.[16,19,20]

While CO_2 capture and storage is imperative, equally crucial is the development of efficient technologies for converting CO_2 into useful products (carbon capture and utilisation, CCU), since CCS is a short-to-medium term option only.[19] Moreover, using CO_2 as a renewable carbon feedstock might

offset costs created by CO_2 capture processes, making it more economically attractive.[21] As a result, converting CO_2 into useful products such as fuels, chemicals and plastics has become an important focus in the scientific community.[22-24]

1.2.2 METHANOL FROM CO_2

Methanol is a clean burning, liquid transport fuel which can be blended with gasoline, offering an attractive, 'drop-in' substitute with the existing fuel infrastructure.[25] Moreover, it is an excellent energy vector, providing a transportable, energy dense storage medium that is well suited for renewable electricity production.[25,26]

1.2.3 PHOTOCATALYTIC FORMATION OF MEOH FROM CO_2

The conversion of CO_2 into useful energy in the presence of water and sunlight is an attractive prospect. To realise this, efficient light harvesting catalysts are required. Given that sunlight is comprised of ~43% visible light, these catalysts should exhibit efficient absorptivity across the visible spectrum.[27] In this respect, semiconducting nanoparticles with a narrow band gap, suitable band edge potential, enhanced charge separation and transport and reduced charge recombination are of particular interest.[28]

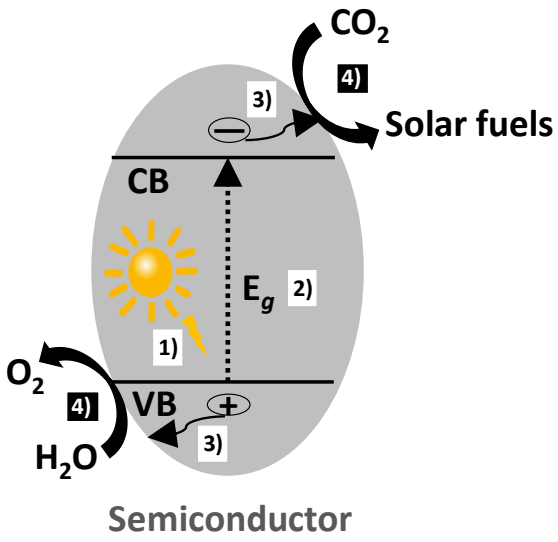

Figure 1.2. Schematic illustration of photocatalytic fuel production from CO_2 and water using solar energy: 1) Absorption of light, 2) charge separation, 3) charge transport to the catalyst surface and 4) redox reactivity. CB, conduction band; VB, valence band; Eg, band gap.

Photocatalytic solar fuel generation is comprised of four steps: 1) generation of an exciton by the absorption of light (photon energy ≥ E_g of the semiconductor), 2) charge separation of electron and hole, 3) transport of charges to the surface of the catalyst, and 4) reduction of CO_2 into fuel precursors such as formate, carbon monoxide, methanol and methane by the generated electrons with concomitant oxidation of water by the generated holes to provide O_2.[29,30]

Thin films (i.e. 2D materials) of such semiconductors deposited onto substrates are excellent candidates as they allow for more efficient light absorption compared to suspended powders in

solution.[31] Moreover, they may be more cost effective since less material is required.[32] Also, the catalyst handling and its recyclability/recovery is simplified.[32] However, one of the major challenges is the formation of inexpensive, high quality films with a large surface area.

1.2.3.1 Nanostructured large area device fabrication

Conventional thin nanostructured solid films may be generated *via* atomic layer deposition (ALD), chemical vapour deposition (CVC) or physical vapour deposition (PVD), but these techniques are energy intensive and may require high cost equipment and precursors.[32-34] Alternatively, the formation of thin films *via* solution-based techniques from pre-prepared NPs of a controllable size, shape and composition might enable low cost and efficient device processing with the possibility for roll-to-roll device fabrication.[35]

Efficient device fabrication *via* solution-based techniques, such as spin-coating, inject printing or drop casting, require high quality nanoparticles that form stable colloidal dispersions (i.e inks). As colloidal systems have a high NP surface they tend to aggregate to minimise their high surface energies; ligands can avoid this happening by passivating the surface of the NP.[36]

1.2.3.2 Nanoparticle stabilisation

Nanoparticles can be stabilised and solubilised by ligands coordinated at the particle surface. This strategy may prevent agglomeration and precipitation from solution. Three different strategies are applied to achieve NP stabilisation:[36]

(1) *Electrostatic stabilisation* (**Figure 1.3**, A) is achieved *via* repulsive forces between solvent molecules and NPs with highly charged but weakly coordinating ionic ligands, such as sodium citrate, ascorbic acid or tertiary butyl ammonium. This nanoparticle stabilisation is beneficial if post-synthetic ligand exchange is desired, but problematic if long-term stabilisation is necessary as electrostatically stabilised NP solutions are prone to irreversible aggregation with changes in pH, concentration and temperature.[36]

(2) *Steric stabilisation* (Figure 1.3, B) is achieved by using long-chain or sterically hindered ligands. The thickness of the ligand 'shell' around the NP has a direct influence on its stability. Depending on the chain length and type of ligand the stability of these solutions may vary. However, steric stabilisation may limit the free movement of the NPs in solution.[36]

(3) *Electrostatic and steric stabilisation* (Figure 1.3, C) is achieved when ligands with a polar head group and a long chain are utilised as this introduces a electrical double layer for electronic stabilisation, and steric stabilisation, respectively.[36]

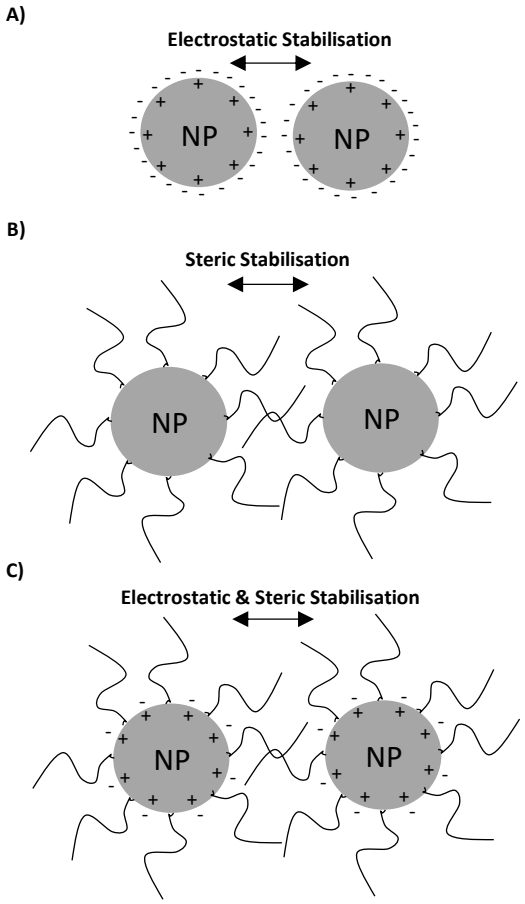

Figure 1.3. A) Electrostatic, B) steric and C) a combination of electrostatic and steric stabilisation of NPs in colloidal dispersions.

1.2.3.3 Ligand classification

Ligands are usually comprised of an alkyl chain that enables solubility in organic solvents, and an anchoring headgroup that dictates the binding fashion and strength onto the NP surface.[35] In analogy to coordination chemistry, Green's covalent bond classification can be used to classify ligands as either X-, L- or Z-type ligands, depending on their mode of coordination to the surface of the NPs.[35,37,38] X-type ligands are anionic and form a covalent metal-ligand bond by donating one electron to the metallic NP; examples include carboxylate (i.e. RCO_2^-) or alkoxide (i.e. R_3CO^-) ligands. L-type ligands (i.e. neutral Lewis bases) donate two electrons towards the metal ion forming a dative covalent bond; examples include amines (i.e. NR_3) or phosphines (i.e. PR_3). Z-type ligands (i.e. σ-Lewis acids) accept two electrons from the metal ion; examples include H^+ or boranes (i.e. BR_3; **Figure 1.4**).[35,39]

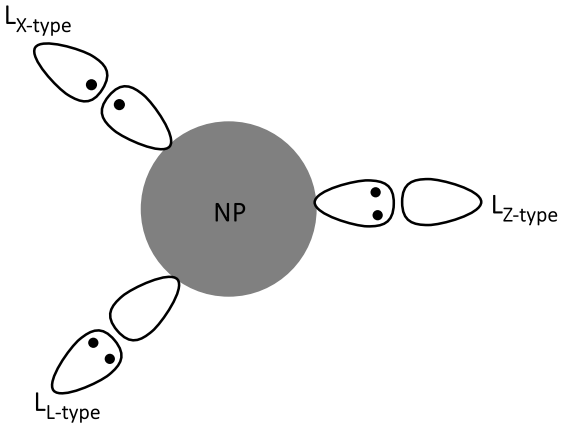

Figure 1.4. Coordination of different ligand types onto the NP surface, and classified using Green's covalent bond classification. Modified from Ref.[39]

The metal-ligand bond strength depends on the position of HOMO and LUMO of the ligands with respect to the NP Fermi level.[37] In this context, Hard-Soft Acid-Base (HSAB) theory is frequently applied to qualitatively predict the strength of the NP-ligand bonding interaction. In general, soft metal ions (i.e. late d-block metals in low oxidation states) coordinate more strongly to soft ligands (i.e. phosphines or thioethers), and hard metal ions (i.e. early d-block metals in high oxidation states) coordinate more strongly to hard ligands (i.e. oxides or halides).[37] The modified electron density and charge distribution on the NP surface was observed experimentally by changes to the surface plasmon resonance (SPR) of Au nanoparticles, capped with ligands of varied donor moieties (i.e. dodecanol,

dodecylamine and dodecylthiol).[40] Stronger ligand coordination to the NP surface resulted in a greater red shift of the SPR band maximum in the order of Au-S > Au-N > Au-O, in accordance with HSAB theory. Despite the relative utility of HSAB theory to predict the strength of metal-ligand coordination, it does not always reflect the experimental results correctly.[37]

Kepp reported a quantitative scale of oxophilicity and thiophilicity to empirically predict whether a metal ion will preferentially coordinate to an oxygen- (i.e. oxophilic metal) or sulphur-containing ligand (i.e. thiophilic metal).[41] The study demonstrates that oxophilicity is correlated to the metal ion electronegativity, Θ. The scale was found to provide an accurate measure of various types of reactions. For example, highly oxophilic Ce (Θ = 0.9) demonstrates a poor release of oxygenated products formed in catalytic diesel soot oxidation. However, doping CeO_2 with moderately oxophilic metals, such as copper (Θ = 0.2) and manganese (Θ = 0.4), facilitated the release of gasificated soot and thus increased catalytic activity and selectivity.[42] Applying the concept of oxophilicity and thiophilicity for NP metal ions to ligand selection for NP stabilisation may help to predict and rationalise ligand selection for a particular NP.

1.2.3.4 Synthesis of colloidal NP dispersions

Surface functionalities that form stable NP colloidals can be installed after NP synthesis *via* ligand exchange processes.[35] Ligands present during the NP formation generally lead to stable colloidal nanoparticles.[35] Co-precipation[43], solvothermal[44], hydrothermal[45], sol-gel,[46] hot-injection[47] and microemulsion[48] processes, all rely on solution phase nucleation with ligands to form colloidal NPs.

The formation of ligated NPs is often described as a two-step process: (1) Nucleation, which is defined as the assembly of atoms or nanoclusters from a reduced and/or decomposed metal precursor. The initial reaction rate of nucleation can be dependent on the reducibility of the metal precursors, the capping ability of the ligand and the reaction temperature, all of which being responsible for dictating the nucleation structure. (2) Growth, which represents the step in which nuclei grow into different sizes and shapes.[36]

Most often NP synthetic routes rely on the use of excess ligands. This may be problematic for catalysis as excess ligands may block active sites and therefore reduce activity.[36] Synthetic routes that make use of organometallic reactivity to access colloidal NPs are an attractive way to prepare stable colloidal NPs as they are typically stabilised by substoichiometric amounts of surface-capping ligands.

This method for colloidal NP synthesis was pioneered by Chaudret and co-workers who took advantage of the highly reactive nature of organometallic precursors, such as $Zn(c\text{-}C_6H_{11})_2$, to form stable ZnO NPs under thermochemical conditions.[49] Such organometallic reactions occur at low reaction temperatures and ligands were found to significantly influence the size and shape of the isolated nanoparticles.[49]

The controlled synthesis of colloidal Cu(0) NPs can be achieved in organic solvents *via* hydrogenolysis of a copper precursor in the presence of substoichiometric amounts of ligands. Isobutyrate copper(II), $[Cu(CHCOO(CH_3)_2)_2]$; mesitylcopper(I), $[CuMes]_5$ or *N,N'*-diisopropylacetamidinato copper(I), $[Cu_2\{(^iPrNH)_2(CHCH_3)\}_2]$ are reported as suitable metal precursors and alkylamine or a carboxylic acid can serve as ligands.[50]

Scheme 1.1. Synthesis of stable colloidal Cu(0) NPs capped with an alkylamine using CuMes as the copper precursor; i) toluene, ii) H_2.

The treatment of a toluene solution of mesitylcopper(I) with substoichiometric amounts of a long chain primary amine (i.e. dodecylamine or octylamine) and H_2 (4 bar) at 100 °C, yielded colloidal Cu(0) NPs that ranged from 3 to 5.5 nm in size.[34] The *in-situ* generated copper(I) amide intermediate was presumably reduced to Cu(0) to yield the metallic NP dispersion (Scheme 1.1).

1.2.3.5 The versatile role of ligands on NP surfaces

Nanoparticle surface-coordinating ligands must be carefully selected as they influence colloidal stability as well as the solubility, morphology, and stability of the resulting nanoparticles, which are properties essential for many applications.[35,36] For instance, ligands may alter the position of the energy levels in semiconducting NPs, which dictates whether such nanomaterials are useful as light-emitting diodes (LED).[35] Understanding the effects of surface ligands on NP luminescence and emission is crucial for improving device efficiency. LEDs that incorporate oleate ligands (size = 1.7 nm) exhibited a 1000 cd/m^2 greater luminance and 1.5 times higher efficiency relative to LEDs that contained the shorter tri-*n*-octylphosphine oxide (TOPO) ligand (size = 1.1 nm).[35] The chain length of the surface ligand was responsible for the enhanced properties since the lower surface area results in an increased injection of holes and electrons into the NP.

If the NPs are considered for electronic and optoelectronic applications the active element is often not the individual particle itself, but a macroscopic assembly of NPs. Good inter-particle electronic and optical communication is key to overall efficiency which again strongly depends on the nature of the ligand and its surface coverage.[35] For example, ligands with short chains form close-packed films, which is considered beneficial for photoconductivity as well as minimising carrier recombination.[51] Another approach is the use of conducting capping ligands such as benzenedithiolate for more effective electron transfer.[52] On the other hand, particles pack in close proximity following ligand removal, enabling electron transfer *via* an inter-particle hopping process.[53] However, ligand removal is often accompanied by undesired NP growth, agglomeration, sintering or morphology changes.[35]

Excess surface coverage blocks active sites or hinders reactants from reaching the NP surface, which is believed to reduce or even inhibit catalytic activity.[35,54] In contrast, recent studies illustrate an improvement in catalytic performance through the metal-ligand interface, as well as a boost in selectivity. The promotional effect of surface-coordinating ligands is caused by either one or a

combination of the following factors, however, differentiating or obtaining an understanding of each factor or promoting a single mechanism is still very challenging.[36]

(1) *Sterics*; the selective blocking of metal surface sites to allow access of only specific small molecule reagents or dictating the orientation of the reactants on the NP surface were found to improve selectivity.[36]

(2) *Electronics*; charge transfer between the ligand and surface atoms of the NP alters the electronic properties, promoting adsorption and reactant activation in order to increase catalytic activity. A study on Pt NPs demonstrated that with increasing electron donor ability of surface-bound ligands the NP surface became more electron-rich, which rendered the adsorption of electron-deficient reactants more feasible.[55]

(3) *Solubility*; when a reaction is conducted in the solution state, ligand polarity must be considered in order to form a stable colloidal solution in the reaction medium.[54] Moreover, polar or nonpolar ligand chains introduce hydrophilic and hydrophobic environments, respectively, which enhance the solubility of certain reagents during catalytic reactivity.[36] This is especially important for gaseous reagents like O_2 and CO_2 where a hydrophobic environment enhances their solubility and subsequent catalytic activity.[56]

Generally, the importance of metal-ligand coordination in NP chemistry is not well understood, therefore more fundamental research may improve future ligand selection.

1.2.4 THERMAL FORMATION OF MEOH FROM CO_2

$$CO + 2H_2 \rightarrow CH_3OH \qquad \Delta H_{298K} = -49.5\ kJ \cdot mol^{-1} \qquad (eq.\ 1)$$

Since the 1960s, methanol has been synthesised from syngas (a CO/H_2 mixture) which is formed from fossil resources *via* the gasification of coal and steam reforming of natural gas (eq. 1).[57,58] To balance the ratio of C/H the feedstock also contains small amounts of CO_2.[59] The current industrially deployed catalyst consists of copper and zinc-oxide nanoparticles with an alumina support ($Cu/ZnO/Al_2O_3$) and produces methanol at moderate pressures (50 to 100 bar) and temperatures (200 ˚C to 300 ˚C).[60] Isotopic labeling studies identified CO_2 as the carbon source for methanol and not CO.[61] Therefore, methanol production using CO_2 as the carbon source gained much attention as CO_2 is obtained directly from the atmosphere or exhaust gases of fossil fuel-burning power plants. Since H_2 is also obtained from a renewable energy source, the process has become highly attractive for CCU.[57] However, CO_2 is stable (strong C=O bonding energy; 127 kcal·mol^{-1}[62]) making efficient and productive catalysis difficult to achieve.[63] Therefore, efforts towards thermal conversion of CO_2 to methanol has received significant attention over recent years.[64]

1.2.4.1 Thermodynamic considerations

The successful reduction of thermodynamically stable CO_2 to methanol is achieved at high pressures and low temperatures.[65] Using an excess of H_2 favours the equilibrium further.[65] However, the activation of CO_2 often requires high temperatures and therefore, the endothermic reverse water gas shift (RWGS) is in direct competition (eq. 3).

$$CO_2 + 3H_2 \rightarrow CH_3OH + H_2O \qquad \Delta H_{298K} = -49.5\ kJ \cdot mol^{-1} \qquad (eq.\ 2)$$

$$CO_2 + H_2 \rightarrow CO + H_2O \qquad \Delta H_{298K} = +41.2\ kJ \cdot mol^{-1} \qquad (eq.\ 3)$$

Leitner and co-workers developed homogeneous ruthenium-based catalytic systems (Ru-triphos centre ; triphos = 1,1,1-tris(diphenylphosphinomethyl)ethane) that showed the direct conversion of CO_2 to methanol.[59,66] Furthermore, well-defined molecular cobalt catalysts ($[Co(triphos)(L)_n]^{m+}$) that are active for carbon dioxide hydrogenation to methanol have been reported by Beller and et al.[67] Despite the high selectivity and activity obtained for homogeneous catalysts, there is a trend towards heterogeneous catalysts due to their superior stability, and ease of separation/recycling ability. In particular, multi metallic Cu-Zn industrial catalysts offer the highest rate and selectivity for the transformation of CO_2 into methanol. As a result, research has been heavily focussed on improving the efficiency of this process in order to compete with the syngas-based process.[57]

To optimise their performance, the role of each component has been studied to understand the complex nature of the active site on the Cu/ZnO-based catalysts. However, their role in catalysis remains controversial.[58,68]

1.2.4.2 The power of three

One of the best heterogeneous catalysts for the direct conversion of CO_2 to methanol is based on a ternary (three component system) system consisting of copper and zinc-oxide nanoparticles supported on Al_2O_3. Understanding the fundamental chemistry behind the observed activity has been a key focus using microscopy, spectroscopy and computational calculations to understand the system. Yet, it remains a challenge to pinpoint the exact origin of the high catalytic activity because the active sites represent only a small fraction of the materials. Additionally, dynamic processes occur within the catalyst during pre-treatment and under working conditions, complicating mechanistic elucidation.[68]

It is generally understood that ZnO either acts as a structural or electronic promoter.[68,69] It is also clear that an increased contact area between Cu(0) and Zn(II) boosts the formation of methanol from CO_2.[69,70] For example, Van Den Berg and co-workers showed that a Cu(0)/ZnO catalyst that was

10 times more active than the Cu(0) catalyst on its own.[71] Coperét et al.[72] investigated the role of the Lewis acidic, non-reducible alumina-support by using Cu(0)/Al_2O_3 as the model catalyst. Specific interfacial sites between Cu(0) and Al_2O_3 were identified and proposed to enhance both methanol and CO production, alongside with the dehydration of methanol to dimethylether.[72]

1.2.4.3 Mechanistic Pathways

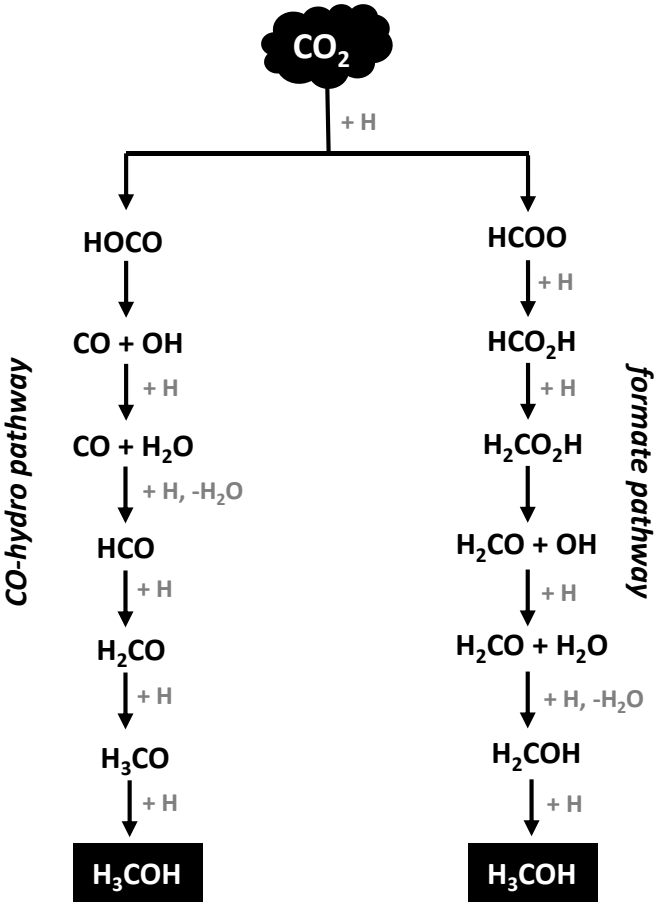

Figure 1.5. Possible reaction pathways for CO_2 hydrogenantion to methanol.

Two major reaction pathways for the chemical fixation of CO_2 to methanol over copper catalysts have been proposed.[73] The CO-hydro pathway (**Figure 1.5**, left), involves CO as an intermediate, formed from a carboxyl (HOCO) species *via* the RWGS reaction, and the subsequent hydrogenation to methanol. The other mechanism, the formate pathway (**Figure 1.5,** right), first generates formate (HCO_2) as an

intermediate from the hydrogenation of CO_2. Subsequently formate is hydrogenated, *via* C-O bond cleavage, forming methanol. Computational studies have indicated that there is a preference for the formate pathway, as its barrier is considerably lower (activation energy (E_g) = 0.77 eV on ZnCu(211)) than the barrier for the formation of HOCO (activation energy (E_g) = 0.99 eV on ZnCu(211)). Experimental observation indicate prove for this theory, as the formate was the most observed intermediate by X-ray photoemission spectroscopy (XPS).[73]

1.2.4.4 Synthetic strategies to Cu/ZnO-based catalysts

The industrial Cu/ZnO/Al_2O_3 methanol synthesis catalyst is known to be "structure-sensitive".[60] In that regard, the right synthetic approaches are critical to deliver its catalytic performance.

Generally, the synthesis starts with the formation of amorphous, well-mixed CuZn(Al) hydroxycarbonates, formed by the co-precipitation of metal nitrate and sodium carbonate solutions, at constant temperatures and pH values. Ageing converts the slurry into single-phase crystalline precursor, such as malachite $Cu_2(OH)_2CO_3$, zincian malachite $(Cu_xZn_y)_2(OH)_2CO_3$, aurichalcite $(Cu_xZn_y)_5(OH)_6(CO_3)_2$ and hydrozincite $Zn_5(OH)_6(CO_3)_2$. The active catalyst is formed after thermal decomposition of such hydroxycarbonates and *in situ* reduction.[74]

1.2.4.4.1 Catalysts from hydrotalcite-like precursors

Since the discovery and isolation of a single atomic layer of carbon in 2004, 2D materials have attracted increasing attention.[75,76] Among them, Layered Metal Hydroxides (LMHs) have applications in biomedicine, photoluminescence, catalysis, and electrochemical energy storage and conversion.[77,78]

The layered single metal hydroxides (LSHs), consist of divalent metal cations octathedrally linked by hydroxyl units and intercalated by various anions and water molecules within the interlayer gallery.[77] These structures are Brucite-type phases. Replacing a certain fraction, x, of divalent metal ions with trivalent cations, forms layered double hydroxides (LDHs). These exhibit a hydrotalcite-like (htl)

structure.[76] Such structures are best described by the general formula, $[M^{II}_{1-x}M^{III}_{x}(OH)_2(A^{n-})_{x/n}\cdot mH_2O]$, where M^{II} is a divalent cation (i.e. Mg, Co, Ni, Cu, Zn or Ca), and M^{III} is a trivalent metal cation (i.e. Al, Fe, Cr or Ga). The charge of the cationic sheets is compensated by intercalated anions, like CO_3^{2-}, NO_3^- and SO_4^{2-};[79] x is normally within the range of 0.25–0.33,[79] and water molecules are loosely coordinated in the interlayer region.[80]

A large library of compounds can be synthesised by changing the identity of the metal and/or intercalating ions, resulting in adaptable physiochemical properties tailored for specific applications.[77]

LDH precursors offer great promise in catalysis due to their homogeneous distribution of metal cations inside the 2D layers and after calcination (and reduction) may afford well-dispersed mixtures of metal oxide particles.[81,82] Recently, Cu-based catalysts derived from LDH precursors were found to show good dispersion at the atomic level, high stability against sintering, high specific surface area and a high degree of cooperativity between the metal cations.[83,84] These properties are considered to enhance methanol production from CO_2 and so several catalysts deriving from ternary and quaternary Cu-containing LDHs were tested (Table 1.1).[81,85-92]

Table 1.1. Table showing catalysts for methanol synthesis deriving from Cu(II) containing hydrotalcite like structures.

htl precursor for catalyst	d_{Cu} [nm]	δ_{Cu} [$m^2 \cdot g^{-1}$]	D_{Cu} [%]	T [°C]	P [bar]	Space velocity[a]	Gas feed	STY[b]	TOF [s^{-1}]	Selectivity [mol% C]
$Cu_6Zn_3Al_{0.7}Zr_{0.3}$-CO_3[86]	-	17.24	4.66	250	50	(G) 4000	25% CO_2 75% H_2	0.18 [$gmL^{-1}h^{-1}$]	-	55.0
$Cu_6Zn_3Al_{0.7}Zr_{0.3}$-CO_3[87]	-	21.4	6.0	250	50	(W) 7500	25% CO_2 75% H_2	0.3	-	53.6
$Cu_2Zn_1Al_{0.7}Zr_{0.3}$-CO_3[88]	-	41.5	14.4	270	50	(G) 4000	25% CO_2 75% H_2	0.16 [$gmL^{-1}h^{-1}$]	9.22 $\times 10^3$	43.1
$Cu_{50}Zn_{25}Al_{22.5}Y_{2.5}$-$CO_3$[89]	-	34.3	13.7	250	50	(W) 12 000	25% CO_2 75% H_2	0.52	-	47.1
$Cu_{51.1}Zn_{23.5}Al_{22.4}Y_3$-$CO_3$[90]	8.3	34.3	13.6	230	50	(W) 10 000	25% CO_2 75% H_2	0.39	6.66 $\times 10^3$	69.3
$Cu_2Zn_1Al_{1.2}Zr_{0.1}$-CO_3[91]	6.5	19.4	6.07	190	50	(G) 4000	24% CO_2 73% H_2 3% N_2	0.087	7.34 $\times 10^{-3}$	81.84
$Cu_{50}Zn_{17}Al_{33}$-CO_3[81]	7	7	-	250	60	(W) 20 000	4% CO_2 72% H_2 10% CO 14% He	-	2.68 $\times 10^{-2}$	-
$Cu_{50}Zn_{17}Al_{18}Ga_{15}$-$CO_3$[92]	8.5	7.2	-	250	60	(W) 20 000	4% CO_2 72% H_2 10% CO 14% He	-	-	100
$Cu_{0.47}Zn_{0.32}Ga_{0.21}$-$CO_3$[85]	< 5	99.2	46	270	45	(W) 18 000	25% CO_2 75% H_2	0.59	2.15 $\times 10^{-3}$	49

[a](G) = GHSV = gas hourly space velocity volume [h^{-1}]; (W) = WHSV = weight hourly space velocity [$mL \cdot g_{cat}^{-1} \cdot h^{-1}$], [b]Space time yield of methanol [$g_{MeOH} \cdot g_{cat}^{-1} \cdot h^{-1}$].

In summary, an optimal methanol catalyst has a highly dispersed but accessible distribution of small copper crystallites, with a high Cu(I)/Cu(0) ratio that interacts with its oxide matrix. The synthetic methods of pre-phases are very important and continue to warrant attention.

1.2.5 POLYMERS FROM CO_2

Synthetic polymers are typically formed from natural gas or crude oil, and have become an indispensable part of our everyday life.[93] The worldwide production in 2020 was estimated to 367 million metric tons.[94] Due to tailorable physical properties, such as weight, toughness and strength they find use in packaging, consumer products, textiles, building materials and electronics amongst other areas of modern life.[93]

Polycarbonates, with a production of 4.4 million metric tons/annum in 2016, are represented as a rather small proportion of plastics but are heavily used as replacements for glass in automotive interiors, sunglasses, bulletproof windows, and medical devices.[95,96] Also, their use as blends has attracted significant attention. Typical blends include stiff polymers in form of polyhydroxybutyrates or poly(lactid acid). The resulted composites often demonstrated better toughness, stiffness and transparency, which are favourable for commercialisation.[97]

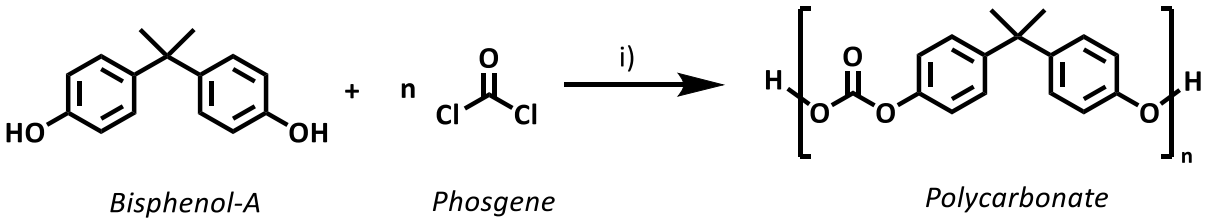

Scheme 1.2. Industrial synthesis of polycarbonate. i)+ NaOH, - NaCl/H_2O. Modified from Ref.[98]

The industrial production from bisphenol A and phosgene (Scheme 1.2) yields the polymer, featuring [O-C(=O)-O) repeat units in the backbone, with a glass transition temperature T_g of 140–155 °C and good tensile and impact strength.[96] However, the use phosgene as gaseous substrate is undesirable as it is highly toxic. Moreover, the formation of chloride salts and chlorinated solvent waste during polymer production makes this synthesis path even less attractive.[99]

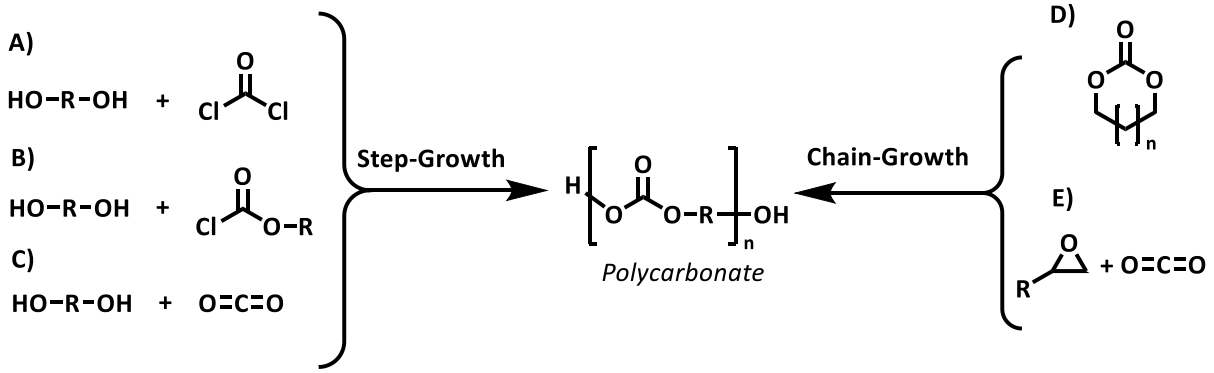

Scheme 1.3. Polycarbonate synthesis *via* step-growth A) Industrial method, B) Greener industrial method, C) Greener method and chain-growth D) Ring opening polymerisation; ROP, E) Ring opening copolymerisation ROCOP. Modified from Ref.[98]

As a greener method, diols can be reacted with other carbonyl fragments such as carbonates or CO_2, affording aromatic or aliphatic polycarbonates (Scheme 1.3, B and C).[100] However, step-growth condensation copolymerisation does not allow a control over the molecular weight and requires high temperatures and the continuous removal of water, and other condensates, to drive the reaction to full conversion, making it a highly energy consuming process.[100] An attractive alternative is the synthesis of polycarbonates *via* ring opening polymerisation of a cyclic monomer (ROP) (Scheme 1.3, D) or the ring opening copolymerisation (ROCOP) (Scheme 1.3, E) of an epoxide with CO_2 in a chain-growth manner as both can be conducted under milder conditions as the driving force is the release of ring strain.[100]

Conversion of the cheap, abundant and non-toxic waste CO_2 into polymers has attracted considerable attention as it is an attractive strategy to move towards a more sustainable chemical industry.[101] Depending on catalyst selection, monomer and conditions the resulting polymer maybe perfectly alternating (polycarbonate, with 43 wt.% CO_2 and ≥99% carbonate linkages) or a combination of carbonate and ether linkages poly(ether carbonate).[98,102]

Perfectly alternating poly(propylene carbonate) yields materials which have a high strength , durability, heat resistance, good electrical insulation and biodegradability.[102-104] However, low glass transition temperatures of 37 °C maybe problematic for any stand-alone plastic applications.[105] Reducing the carbonate linkage content was found to reduce the glass transition temperature. For

example poly(ether carbonate) with 7 wt.% CO_2 content is reported as a viscose material with a T_g of –60 °C, making it potentially useful as a blend (*vide supra*).[102]

1.2.5.1 Mechanistic steps

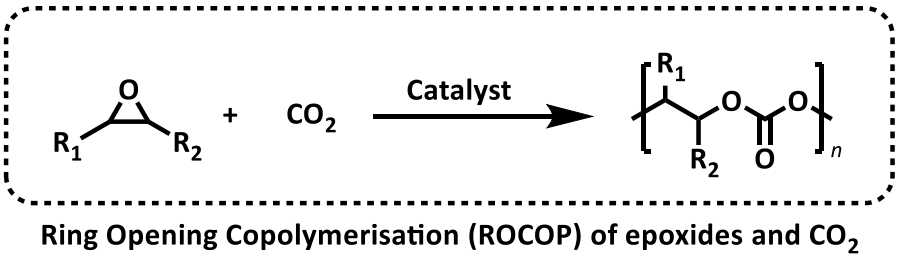

1. Initiation

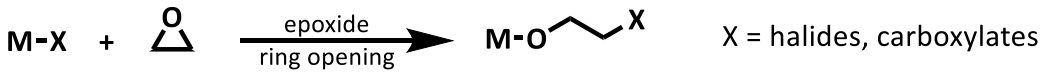

2. Propagation

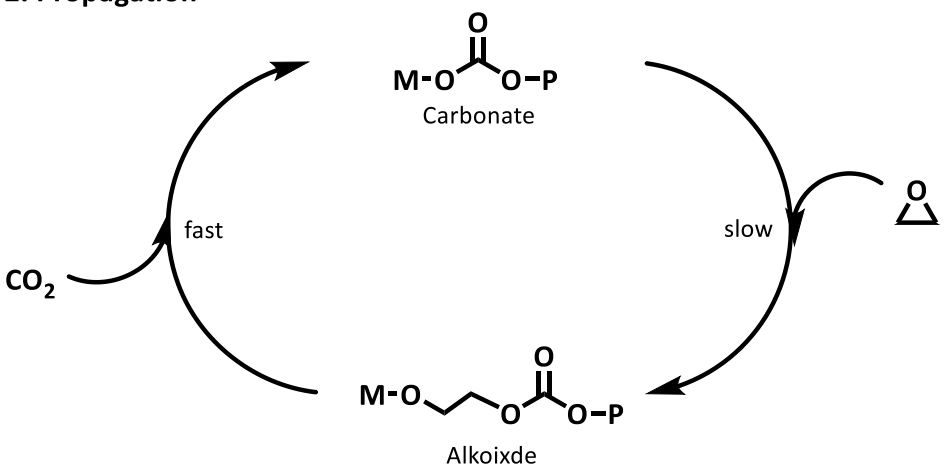

3. Termination

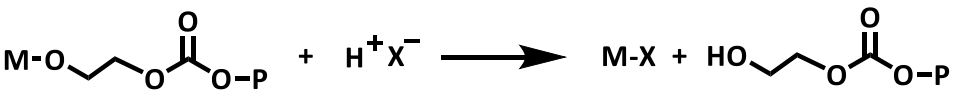

Scheme 1.4. Catalytic formation of poly(propylene oxide) from epoxide and CO_2 (top). Steps involved in the reaction: Initiation, Propagation and Termination. Modified from Ref.[104,106]

Typically, the formation of carbon dioxide derived polymers occurs by a polymerisation mechanism reliant upon some key processes: 1) initiation, 2) propagation 3) termination (Scheme 1.4). The reaction requires a catalyst and this species is implicated in reducing reaction barriers in all steps.

Initiation is proposed to involve the activation of the epoxide at Lewis acidic metal sites and the attack and ring-opening by a nucleophile (X). The nucleophile is typically a metal coordinated halide or carboxylate group. Propagation consists of two elementary reactions: CO_2 insertion and epoxide ring opening. The metal-alkoxide reacts with CO_2 to generate a metal carbonate species. Heterogeneous catalysts typically require high pressures to proceed (>20 bar) and the polymer chain grows by repeated nucleophilic attack by the growing chain on a coordinated epoxide. For propene oxide ROCOP, the ring-opening can be regioselective/random (depending upon the relative site of epoxide ring-opening, different linkages are formed in the polymer chain).[107] Termination occurs during reaction work-up and is proposed to involve the hydrolysis of the chain from the metal. Polymerizations may be quenched by the addition of acids to accelerate the hydrolysis process.[106]

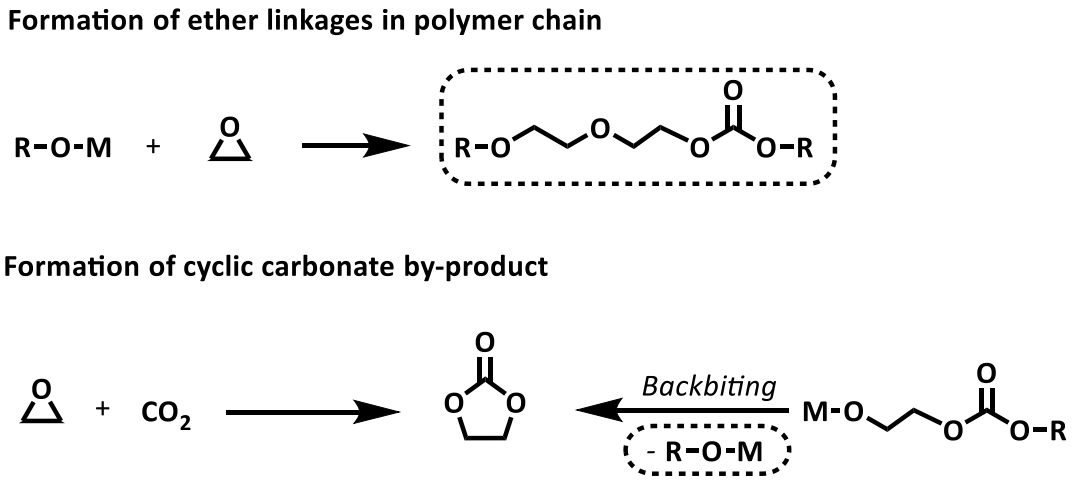

Scheme 1.5. Formation of ether linkages in the polymer or cyclic by products. Products surrounded by dots can go back into the reaction cycle of propylene oxide formation, either generating a polymer mixture of a broader PDI or imperfectly alternating PPC.

Ether linkages form due to sequential insertion of epoxides into the metal alkoxide intermediate and the process is dependent upon the Lewis acidity of metal, although this feature is not well understood or quantified (**Scheme 1.5**).[106] An undesirable by-product is propylene carbonate, a five membered ring cyclic carbonate, which forms either directly from CO_2/epoxide cycloaddition or *via* a polymer chain backbiting reaction (**Scheme 1.5**). Its formation is problematic in large scale synthesis because cyclic carbonates can behave as plasticiser and have high boiling points (hence are energy intensive to remove from the polymer).

1.2.5.2 Catalyst Development

The first copolymerisation of epoxides and CO_2 was reported by Inoue *et al.* in 1969 and the report detailed a catalyst formed *in situ* from a 1:1 mixture of $ZnEt_2$ and water. At 80 °C and 50-60 atm CO_2 pressure, poly(propylene carbonate) was produced in low yield and with low molecular weight.[108] Since this pioneering work, academia and industry have discovered more efficient catalysts; many are complexes of transition metals (e.g. Co, Cr, Zn, Ti, Fe, Ni) and/or base metals (Mg, Na or Al).[104] Only a few metal-free catalysts, such as combinations of *tri*alkyl- and *tri*arylborane[109], organic cations[110-112], organoboron based catalysts[113,114] or tertiary amines[115], have been reported recently.

So far, the vast majority of published research focusses on homogeneous catalysts as they yield high polymer conversions, molar mass control and narrow dispersions (*Đ*). Reaction processes can be probed through use of NMR spectroscopy, IR spectroscopy and theoretical analysis. Nonetheless, the patent literature focus has been on heterogeneous catalysts, although more challenging to elucidate structure-activity relationships, they are typically easy to synthesise at scale and use cheap, colourless and non-toxic zinc with the ability to be recovered and reused.

To-date, two major heterogeneous catalyst systems have been developed: 1) Zn-Co double-metal cyanide complexes (DMC) and 2) zinc dicarboxylates (ZnGA). Among them, DMC catalysts show the highest productivity of 60.6 kg polymer/ g Zn–Co-DMC.[104,116] These catalysts yield poly(ether

carbonates), typically with low carbonate linkage uptakes, making them attractive in the preparation of polyols for polyurethane synthesis.[104,117] DMC catalysts are, however, quite complex to use – they require specific activation protocols and can be easily deactivated.[118] They also contain cobalt which is expensive. In contrast, zinc dicarboxylates offer a cheap and non-toxic alternative and are able to produce polymers with greater carbon dioxide uptake and higher molar masses. Thus, despite their lower catalytic efficiency (0.16 kg polymer/g ZnGA catalyst, **Table 1.2** entry 10) they can be desirable to use in the production of a broad range of polycarbonates.[119]

Among zinc based dicarboxylates, zinc glutarate (ZnGA) has been studied extensively over the last 50 years, as it is easy to synthesise and yields poly(propylene carbonate) materials with high molecular weight (~150 kg/mol) in good yields.[120] It is speculated that the dicarboxylate glutarate generates a structure with the correct balance of crystallinity, zinc Lewis acidity and optimal Zn—Zn distance (between 4 – 5 Å; theoretically calculated) for a dinuclear activation/polymerisation mechanism to operate.[104,121] The use of alternative dicarboxylates resulted in a significant drop in activity.[121]

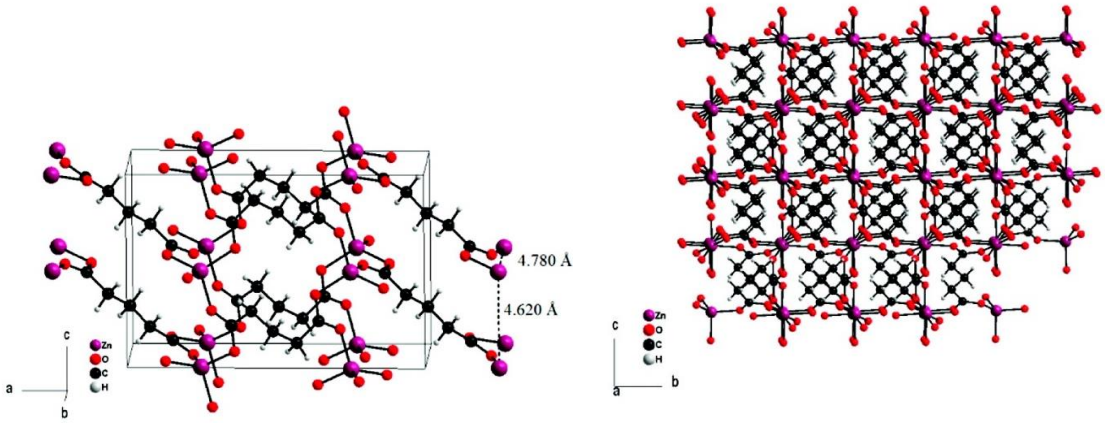

Figure 1.6. Solid-state structure of ZnGA. View along b-axis (left) and view along a-axis (right).[121] Reprinted with permission from *J. Am. Chem. Soc.* 2011, 133, 33, 13151-13161. Copyright 2011 American Chemical Society.

The solid-state structure of ZnGA was evaluated using X-ray powder diffraction experiments (**Figure 1.6**). The structure consists of layered tetrahedrally coordinated zinc atoms bound to four oxygen

atoms from different glutarate units, which bridge the layers (Figure 1.6).[122-124] As no micro-pores were identified, the catalytic active sites were hypothesised to be present on the catalyst's surface as the epoxide monomer is not expected to diffuse into the bulk material.[104]

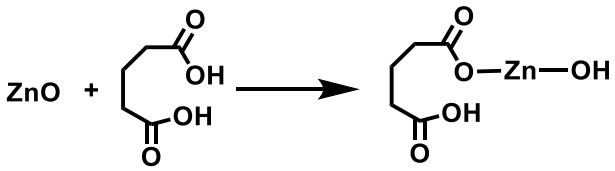

Scheme 1.6. Zinc hydroxyl groups formed as a result of the monocondensation of ZnO and glutaric acid.[125]

Chisholm and co-workers identified hydroxyl end-groups to the poly(propylene carbonate), PPC, formed by zinc glutarate catalysts using mass spectrometry.[126] From this result, Rieger and co-workers concluded that hydroxyl-groups should be present in the initiator.[125] Since the synthetic protocol for ZnGA requires a condensation reaction between ZnO and glutaric acid (Scheme 1.6), the active sites/initiators were proposed to be surface Zn-OH groups.[125]

Additional studies on the interaction of propylene oxide and carbon dioxide with ZnGA by near edge X-ray absorption fine structure spectroscopy (NEXAFS) showed a reversible absorption of both monomers on to the catalyst surface *via* insertion into the Zn-O bond on the surface of the ZnGA material. The surfaces showed preferential propylene oxide (PO) absorption (ZnGA powder on Si wafer exposed to 20 bar CO_2 pressure for 10 h, followed by exposure to PO at 35 °C for 4 h), which implies that the copolymersisation is initiated by PO insertion rather than CO_2.[127] Theoretical calculations, by Rieger et al., implicated a bimetallic mechanism dependent upon two zinc centres ideally separated by 4.3-5 Å on the surface.[121]

The many investigations of ZnGA catalysts have shown that the activity depends strongly on the zinc precursors, synthetic protocol, crystallinity, particle size, Zn–Zn distance, and the amount of surface active sites that are accessible.[119-121] As a result, studies to improve the overall catalytic activity of ZnGA have mainly focused on synthetic protocol modifications to increase the surface area, whilst maintaining high crystallinity.

Moreover, it was found that the source of zinc and glutarate used in the synthesis of ZnGA was crucial for the catalytic polymerisation activity.[128,129] Among the various starting materials, the use of ZnO and glutaric acid produced the best catalysts (*vide supra* and **Table 1.2**). For comparison, best value achieved for ZnGA synthesised from $ZnEt_2$ and glutaric acid produced only 2.5 grams of alternating polypropylene carbonate per gram of catalyst under the same reaction conditions (Entry 2 in **Table 1.2**).[130]

Table 1.2. Comparison of Selected ZnGA Catalysts for the Copolymerisation of Carbon Dioxide (CO_2) and Propylene Oxide (PO).

Entry	Precursors	Cat. [g]	PO [mL]	CO_2 [bar]	Temp. [ºC]	Time [h]	Productivity [$g/g_{Catalyst}$]	M_n [kg/mol]	$Đ$ [g/mol]
1[131]	$ZnEt_2$-GA	1.6[a]	15[b]	40[c]	35	44	0.22[d]	-	-
2[130]	$ZnEt_2$-GA	1.0	100	52[c]	60	40	2.5	11.0	11.3
3[130]	$Zn(OH)_2$-GA	1.0	100	52[c]	60	40	8.8	22.0	3.0
4[130]	ZnO-GA	1.0	100	52[c]	60	40	64.0	143.0	2.4
5[132]	$Zn(OAc)_2{\cdot}2H_2O$-GA	1.0	-	41[e]	60	40	83.0	60.0	2.7
6[133]	ZnO-GA	0.5	100	50[f]	60	40	126.0	56.1	-
7[134]	ZnO-GA	0.5	100	52[f]	60	40	115.2	14.5	2.2
8[135]	ZnO-GA	0.1	30	50	60	36	130[g]	14.5[h]	3.3
9[129]	ZnO-GA	0.4	40	51[c]	60	40	40.0	>50	-
10[119]	ZnO-GA	0.3	100	52[f]	60	40	160.4	26.3	-
11[121]	ZnO-GA	0.1[i]	10[j]	40	80	20	71.5[k]	103.0	2.8
12[120]	ZnO-GA	0.2	20	30[f]	60	40	132.1	147.8	2.2

[a]Calculated from the reported moles of $ZnEt_2$. [b]The amount of PO was reported in g but as been converted into mL for consistency. [c]The pressure was reported in atm but has been converted into bar for consistency. [d]Calculated from the copolymer yield. [e]The pressure was reported in psi but has been converted into bar for consistency. [f]The pressure was reported in MPa but has been converted into bar for consistency. [g]Calculated from the amount of catalyst and polymer yield [$kg{\cdot}mol^{-1}$ Zn] reported. [h]Calculated from the number average molecular weight $\cdot 10^{-3}$ [$g{\cdot}mol^{-1}$]. [i]The amount of catalyst was reported in mmol but has been converted into g for consistency. [j]The amount of PO was reported in mmol but has been converted into g for consistency. [k]Reported as the turnover number [grams of polymer per moles of zinc].

For example, the addition of amphiphilic block copolymer templates (eg. poly(ethylene glycol)-*block*-poly(propylene glycol)-*block*-poly(ethylene glycol); Pluronic PE6400) during the synthesis[132] enhance the surface area of the ZnGA catalyst while retaining crystallinity (Entry 5, **Table 1.2**). The support of Zn glutarate onto perfluorinated polymers (Entry 6, **Table 1.2**)[133] or silica (Entry 8, **Table 1.2**).[135] resulted in even better productivity, once again attributed to greater product crystallinity. Dispersing the ZnGA onto the surface of acid-treated montmorillonite clay was also effective and was attributed to the effective dispersion of small catalyst crystallites which increase the overall catalyst surface area (Entry 7, **Table 1.2**).[134] Also, ultrasonication of the catalyst was found to be efficient in

improving activity (Entry 9 and 10, **Table 1.2**).[119,129] Rieger improved the activity of ZnGA *via* ball milling of ZnGA, under N_2 in the presence of water, to generate more Zn-OH initiator groups on the surface (Entry 11, **Table 1.2**).[121] However, further downsizing of the catalyst particles was restricted by the lower limit of ball milling, which is 1 μm.[3] Thus, nanosized ZnGA particles *via* surface-etching of standard ZnO offers an alternative methodology (Entry 12, **Table 1.2**).[120]

Despite these advances, the catalytic activity of ZnGA has been only marginally improved over the past decade.[121] In contrast to the efforts afforded to optimising ZnGA, much less investigation of alternative heterogeneous zinc catalysts have been undertaken.

1.3 REFERENCES

[1] R. P. Feynman, *APS annual meeting*, Plenty of Room at the Bottom (1959).

[2] N. Taniguchi, *International Conference of Production Engineering 18-23 (Japan Society of Precision Engineering, 1974)*.

[3] A. P. Alivisatos, *J. Phys. Chem.* **1996**, *100*, 13226-13239.

[4] S. Horikoshi, N. Serpone, *Microwaves in nanoparticle synthesis: fundamentals and applications*, John Wiley & Sons, **2013**.

[5] K. J. Balkus, *New and Future Developments in Catalysis - Catalysis by Nanoparticles* Elsevier, **2013**.

[6] B. Rogers, J. Adams, S. Pennathur, *Nanotechnology Understanding Small Systems*, Apple Academic Press Inc, **2014**.

[7] Z.-Y. Zhou, N. Tian, J.-T. Li, I. Broadwell, S.-G. Sun, *Chem. Soc. Rev.* **2011**, *40*, 4167-4185.

[8] C. Mello-Donega, *Nanoparticles Workhorses of Nanoscience*, Springer, **2014**.

[9] A. H. M. Leung, *PhD Thesis* **2018**.

[10] T. A. Saleh, *Environ. Technol. Innov.* **2020**, *20*, 101067.

[11] C. Buzea, I. Pacheco, in *EMR/ESR/EPR Spectroscopy for Characterization of Nanomaterials*, Springer, **2017**.

[12] *https://www.iea.org/reports/co2-emissions-from-fuel-combustion-overview (accessed November 2021)*.

[13] Z. Liu, P. Ciais, Z. Deng, R. Lei, S. J. Davis, S. Feng, B. Zheng, D. Cui, X. Dou, B. Zhu, *Nat. Commun.* **2020**, *11*, 1-12.

[14] B. Pfefferbaum, C. S. North, *N. Engl. J. Med.* **2020**, *383*, 510-512.

[15] C. A. Tisdell, *Econ. Anal. Policy* **2020**, *68*, 17-28.

[16] R. Kumar, R. Mangalapuri, M. H. Ahmadi, D.-V. N. Vo, R. Solanki, P. Kumar, *Int. J. Low-Carbon Technol.* **2020**.

[17] K. Jiang, P. Feron, A. Cousins, R. Zhai, K. Li, *Environ. Sci. Technol.* **2020**, *54*, 2429-2438.

[18] C. Cao, H. Liu, Z. Hou, F. Mehmood, J. Liao, W. Feng, *Energies* **2020**, *13*, 600.

[19] M. S. Diallo, N. A. Fromer, M. S. Jhon, in *Nanotechnology for Sustainable Development*, Springer, **2013**, 1-16.

[20] M. H. Ahmadi, M. Ghazvini, M. Alhuyi Nazari, M. A. Ahmadi, F. Pourfayaz, G. Lorenzini, T. Ming, *Int. J. Energy Res.* **2019**, *43*, 1387-1410.

[21] C. Hepburn, E. Adlen, J. Beddington, E. A. Carter, S. Fuss, N. Mac Dowell, J. C. Minx, P. Smith, C. K. Williams, *Nature* **2019**, *575*, 87-97.

[22] Y. Zhu, C. Romain, C. K. Williams, *Nature* **2016**, *540*, 354-362.

[23] J. Wei, Q. Ge, R. Yao, Z. Wen, C. Fang, L. Guo, H. Xu, J. Sun, *Nature* **2017**, *8*, 1-9.

[24] H. Yang, C. Zhang, P. Gao, H. Wang, X. Li, L. Zhong, W. Wei, Y. Sun, *Catal. Sci. Technol.* **2017**, *7*, 4580-4598.

[25] G. A. Olah, *Angew. Chem. Int. Ed.* **2013**, *52*, 104-107.

[26] M. S. Frei, C. Mondelli, M. I. Short, J. Pérez-Ramírez, *ChemSusChem.* **2020**, *13*, 6330-6337.

[27] J.-Y. Li, L. Yuan, S.-H. Li, Z.-R. Tang, Y.-J. Xu, *J. Mater. Chem. A* **2019**, *7*, 8676-8689.

[28] R. Shwetharani, H. Chandan, M. Sakar, G. R. Balakrishna, K. R. Reddy, A. V. Raghu, *Int. J. Hydrog. Energy* **2020**, *45*, 18289-18308.

[29] J. Kosco, F. Moruzzi, B. Willner, I. McCulloch, *Adv. Energy Mater.* **2020**, *10*, 2001935.

[30] Q. Wang, K. Domen, *Chem. Rev.* **2019**, *120*, 919-985.

[31] C. S. Gopinath, N. Nalajala, *J. Mater. Chem. A* **2021**, *9*, 1353-1371.

[32] R. Pedanekar, S. Shaikh, K. Rajpure, *Curr. Appl. Phys.* **2020**, *20*, 931-952.

[33] M. A. Lazar, *IOP Conf. Ser.: Mater. Sci. Eng.* , Nanostructured thin films as functional coatings, **2010**.

[34] C. Barrière, G. Alcaraz, O. Margeat, P. Fau, J. B. Quoirin, C. Anceau, B. Chaudret, *J. Mater. Chem.* **2008**, *18*, 3084-3086.

[35] A. Heuer-Jungemann, N. Feliu, I. Bakaimi, M. Hamaly, A. Alkilany, I. Chakraborty, A. Masood, M. F. Casula, A. Kostopoulou, E. Oh, *Chem. Rev.* **2019**, *119*, 4819-4880.
[36] L. Lu, S. Zou, B. Fang, *ACS Catal.* **2021**, *11*, 6020-6058.
[37] S. Campisi, M. Schiavoni, C. E. Chan-Thaw, A. Villa, *Catalysts* **2016**, *6*, 185.
[38] M. Green, *J. Organomet. Chem.* **1995**, *500*, 127-148.
[39] N. C. Anderson, M. P. Hendricks, J. J. Choi, J. S. Owen, *J. Am. Chem. Soc.* **2013**, *135*, 18536-18548.
[40] C. Battocchio, F. Porcaro, S. Mukherjee, E. Magnano, S. Nappini, I. Fratoddi, M. Quintiliani, M. V. Russo, G. Polzonetti, *J. Phys. Chem.* **2014**, *118*, 8159-8168.
[41] K. P. Kepp, *Inorg. Chem.* **2016**, *55*, 9461-9470.
[42] Q. Liang, X. Wu, D. Weng, H. Xu, *Catal. Today* **2008**, *139*, 113-118.
[43] I. F. Cruz, C. Freire, J. P. Araújo, C. Pereira, A. M. Pereira, in *Magnetic Nanostructured Materials*, Elsevier, **2018**, 59-116.
[44] B. Gersten, *Chemfiles* **2005**, *5*, 11-12.
[45] J. A. Darr, J. Zhang, N. M. Makwana, X. Weng, *Chem. Rev.* **2017**, *117*, 11125-11238.
[46] M. Parashar, V. K. Shukla, R. Singh, *J. Materi. Sci.: Mater. Electron.* **2020**, *31*, 3729-3749.
[47] S. G. Kwon, T. Hyeon, *Small* **2011**, *7*, 2685-2702.
[48] M. Sanchez-Dominguez, M. Boutonnet, C. Solans, *J. Nanopart. Res.* **2009**, *11*, 1823-1829.
[49] M. L. Kahn, A. Glaria, C. Pages, M. Monge, L. Saint Macary, A. Maisonnat, B. Chaudret, *J. Mater. Chem.* **2009**, *19*, 4044-4060.
[50] C. Barrière, K. Piettre, V. Latour, O. Margeat, C.-O. Turrin, B. Chaudret, P. Fau, *J. Mater. Chem.* **2012**, *22*, 2279-2285.
[51] Y. Liu, M. Gibbs, J. Puthussery, S. Gaik, R. Ihly, H. W. Hillhouse, M. Law, *Nano. Lett.* **2010**, *10*, 1960-1969.
[52] G. I. Koleilat, L. Levina, H. Shukla, S. H. Myrskog, S. Hinds, A. G. Pattantyus-Abraham, E. H. Sargent, *ACS Nano* **2008**, *2*, 833-840.
[53] D. Yu, B. L. Wehrenberg, P. Jha, J. Ma, P. Guyot-Sionnest, *J. Appl. Phys.* **2006**, *99*, 104315.
[54] Z. Niu, Y. Li, *Chem. Mater.* **2014**, *26*, 72-83.
[55] M. Yan, T. Wu, L. Chen, Y. Yu, B. Liu, Y. Wang, W. Chen, Y. Liu, C. Lian, Y. Li, *ChemCatChem* **2018**, *10*, 2433-2441.
[56] G.-R. Zhang, B. J. Etzold, *J. Energy Chem.* **2016**, *25*, 199-207.
[57] J. Zhong, X. Yang, Z. Wu, B. Liang, Y. Huang, T. Zhang, *Chem. Soc. Rev.* **2020**, *49*, 1385-1413.
[58] M. Behrens, *Angew. Chem. Int. Ed.* **2016**, *55*, 14906-14908.
[59] S. Wesselbaum, T. vom Stein, J. Klankermayer,W. Leitner, *Ang. Chem. Int. Ed.* **2012**, *51*, 7499-7502.
[60] M. Behrens, F. Studt, I. Kasatkin, S. Kühl, M. Hävecker, F. Abild-Pedersen, S. Zander, F. Girgsdies, P. Kurr, B.-L. Kniep, *Science* **2012**, *336*, 893-897.
[61] F. Studt, M. Behrens, E. L. Kunkes, N. Thomas, S. Zander, A. Tarasov, J. Schumann, E. Frei, J. B. Varley, F. Abild-Pedersen, *ChemCatChem* **2015**, *7*, 1105-1111.
[62] S. W. Benson, *J. Chem. Educ.* **1965**, *42*, 502.
[63] H.-J. Freund, M. W. Roberts, *Surf. Sci. Rep.* **1996**, *25*, 225-273.
[64] W. Li, H. Wang, X. Jiang, J. Zhu, Z. Liu, X. Guo, C. Song, *RSC Adv.* **2018**, *8*, 7651-7669.
[65] M. M.-J. Li, S. C. E. Tsang, *Catal. Sci.Technol.* **2018**, *8*, 3450-3464.
[66] S. Wesselbaum, V. Moha, M. Meuresch, S. Brosinski, K. M. Thenert, J. Kothe, T. vom Stein, U. Englert, M. Hölscher, J. J. C. s. Klankermayer, *Chem. Sci.* **2015**, *6*, 693-704.
[67] F. K. Scharnagl, M. F. Hertrich, G. Neitzel, R. Jackstell, M. Beller, Catalysis, *Adv. Synth. Catal.* **2019**, *361*, 374-379.
[68] S. R. Docherty, C. Copéret, *J. Am. Chem. Soc.* **2021**, *143*, 6767-6780.
[69] S. Kuld, M. Thorhauge, H. Falsig, C. F. Elkjær, S. Helveg, I. Chorkendorff, J. Sehested, *Science* **2016**, *352*, 969-974.
[70] J. Schumann, M. Eichelbaum, T. Lunkenbein, N. Thomas, M. C. Alvarez Galvan, R. Schlögl, M. Behrens, *ACS Catal.* **2015**, *5*, 3260-3270.

[71] R. Van Den Berg, G. Prieto, G. Korpershoek, L. I. Van Der Wal, A. J. Van Bunningen, S. Lægsgaard-Jørgensen, P. E. De Jongh, K. P. De Jong, *Nat. Commun.* **2016**, *7*, 1-7.
[72] E. Lam, J. J. Corral-Pérez, K. Larmier, G. Noh, P. Wolf, A. Comas-Vives, A. Urakawa, C. Copéret, *Angew. Chem.* **2019**, *131*, 14127-14134.
[73] S. Kattel, P. J. Ramírez, J. G. Chen, J. A. Rodriguez, P. Liu, *Science* **2017**, *355*, 1296-1299.
[74] P. J. Smith, S. A. Kondrat, P. A. Chater, B. R. Yeo, G. M. Shaw, L. Lu, J. K. Bartley, S. H. Taylor, M. S. Spencer, C. J. Kiely, G. J. Kelly, C. W. Park, G. J. Hutchings, *Chem. Sci.* **2017**, *8*, 2436-2447.
[75] K. S. Novoselov, A. K. Geim, S. V. Morozov, D. Jiang, Y. Zhang, S. V. Dubonos, I. V. Grigorieva, A. A. Firsov, *Science* **2004**, *306*, 666-669.
[76] H. Yin, Z. Tang, *Chem. Soc. Rev.* **2016**, *45*, 4873-4891.
[77] G. Chen, H. Wan, W. Ma, N. Zhang, Y. Cao, X. Liu, J. Wang, R. Ma, *Adv. Energy Mater.* **2020**, *10*, 1902535.
[78] J. Yu, Q. Wang, D. O'Hare, L. Sun, *Chem. Soc. Rev.* **2017**, *46*, 5950-5974.
[79] B. Venugopal, C. Shivakumara, M. Rajamathi, *J. Colloid Interface Sci.* **2006**, *294*, 234-239.
[80] A. Garcia-Gallastegui, D. Iruretagoyena, V. Gouvea, M. Mokhtar, A. M. Asiri, S. N. Basahel, S. A. Al-Thabaiti, A. O. Alyoubi, D. Chadwick, M. S. P. Shaffer, *Chem. Mater.* **2012**, *24*, 4531-4539.
[81] S. Kühl, A. Tarasov, S. Zander, I. Kasatkin, M. Behrens, *Chem. Eur. J.* **2014**, *20*, 3782-3792.
[82] F. Cavani, F. Trifiro, A. Vaccari, *Catal. Today* **1991**, *11*, 173-301.
[83] L. Zhang, C. Zheng, F. Li, D. Evans, X. Duan, *J. Mater. Sci.* **2008**, *43*, 237-243.
[84] M. Behrens, I. Kasatkin, S. Kühl, G. Weinberg, *Chem. Mater.* **2010**, *22*, 386-397.
[85] M. M.-J. Li, C. Chen, T. c. e. Ayvalı, H. Suo, J. Zheng, I. F. Teixeira, L. Ye, H. Zou, D. O'Hare, S. C. E. Tsang, *ACS Catal.* **2018**, *8*, 4390-4401.
[86] P. Gao, F. Li, F. Xiao, N. Zhao, N. Sun, W. Wei, L. Zhong, Y. Sun, *Catal. Sci. Technol.* **2012**, *2*, 1447-1454.
[87] P. Gao, F. Li, F. Xiao, N. Zhao, W. Wei, L. Zhong, Y. Sun, *Catal. Today* **2012**, *194*, 9-15.
[88] P. Gao, F. Li, H. Zhan, N. Zhao, F. Xiao, W. Wei, L. Zhong, H. Wang, Y. Sun, *J. Catal.* **2013**, *298*, 51-60.
[89] P. Gao, F. Li, N. Zhao, F. Xiao, W. Wei, L. Zhong, Y. Sun, *Appl. Catal. A* **2013**, *468*, 442-452.
[90] P. Gao, L. Zhong, L. Zhang, H. Wang, N. Zhao, W. Wei, Y. Sun, *Catal. Sci. Technol.* **2015**, *5*, 4365-4377.
[91] S. Xiao, Y. Zhang, P. Gao, L. Zhong, X. Li, Z. Zhang, H. Wang, W. Wei, Y. Sun, *Catal. Today* **2017**, *281*, 327-336.
[92] S. Kühl, J. Schumann, I. Kasatkin, M. Hävecker, R. Schlögl, M. Behrens, *Catal. Today* **2015**, *246*, 92-100.
[93] *https://theconversation.com/the-world-of-plastics-in-numbers-100291 (accessed December 2021)*.
[94] *https://www.statista.com/statistics/282732/global-production-of-plastics-since-1950/ (accessed 2021)*.
[95] *https://www.statista.com/statistics/650318/polycarbonates-production-worldwide-and-in-europe/ (accessed March 2022)*.
[96] Y. Wang, D. J. Darensbourg, *Coord. Chem. Rev.* **2018**, *372*, 85-100.
[97] G. A. Luinstra, *Polym. Rev.* **2008**, *48*, 192-219.
[98] A. C. Deacy, E. Moreby, A. Phanopoulos, C. K. Williams, *J. Am. Chem. Soc.* **2020**, *142*, 19150-19160.
[99] S. Fukuoka, M. Kawamura, K. Komiya, M. Tojo, H. Hachiya, K. Hasegawa, M. Aminaka, H. Okamoto, I. Fukawa, S. Konno, *Green Chem.* **2003**, *5*, 497-507.
[100] X. Zhang, M. Fevre, G. O. Jones, R. M. Waymouth, *Chem. Rev.* **2018**, *118*, 839-885.
[101] X.-B. Lu, W.-M. Ren, G.-P. Wu, *Acc. Chem. Res.* **2012**, *45*, 1721-1735.
[102] J. Langanke, A. Wolf, J. Hofmann, K. Böhm, M. Subhani, T. Müller, W. Leitner, C. Gürtler, *Green Chem.* **2014**, *16*, 1865-1870.
[103] D. J. Darensbourg, S. J. Wilson, *Green Chem.* **2012**, *14*, 2665-2671.
[104] L. Grefe, E. Mejía, *Tetrahedron* **2021**, *98*, 132433.

[105] N. von der Assen, A. Bardow, *Green Chem.* **2014**, *16*, 3272-3280.
[106] M. R. Kember, A. Buchard, C. K. Williams, *Chem. Commun.* **2011**, *47*, 141-163.
[107] C. T. Cohen, T. Chu, G. W. Coates, *J. Am. Chem. Soc.* **2005**, *127*, 10869-10878.
[108] S. Inoue, H. Koinuma, T. Tsuruta, *J. Polym. Sci B.* **1969**, *7*, 287-292.
[109] K. A. Andrea, F. M. Kerton, *ACS Catal.* **2019**, *9*, 1799-1809.
[110] D. Zhang, S. K. Boopathi, N. Hadjichristidis, Y. Gnanou, X. Feng, *J. Am. Chem. Soc.* **2016**, *138*, 11117-11120.
[111] M. Jia, D. Zhang, Y. Gnanou, X. Feng, *ACS Sustain. Chem. Eng.* **2021**, *9*, 10370-10380.
[112] M. Jia, D. Zhang, G. W. de Kort, C. H. Wilsens, S. Rastogi, N. Hadjichristidis, Y. Gnanou, X. Feng, *Macromolecules* **2020**, *53*, 5297-5307.
[113] G.-W. Yang, Y.-Y. Zhang, R. Xie, G.-P. Wu, *J. Am. Chem. Soc.* **2020**, *142*, 12245-12255.
[114] G.-W. Yang, C.-K. Xu, R. Xie, Y.-Y. Zhang, X.-F. Zhu, G.-P. Wu, *J. Am. Chem. Soc.* **2021**, *143*, 3455-3465.
[115] Y. Wang, J.-Y. Zhang, J.-L. Yang, H.-K. Zhang, J. Kiriratnikom, C.-J. Zhang, K.-L. Chen, X.-H. Cao, L.-F. Hu, X.-H. Zhang, *Macromolecules* **2021**, *54*, 2178-2186.
[116] Z. Li, Y. Qin, X. Zhao, F. Wang, S. Zhang, X. Wang, *Eur. Polym. J.* **2011**, *47*, 2152-2157.
[117] J. K. Varghese, D. S. Park, J. Y. Jeon, B. Y. Lee, *J. Polym. Sci A. Polym. Chem.* **2013**, *51*, 4811-4818.
[118] L. C. Wu, A. F. Yu, M. Zhang, B. H. Liu, L. B. Chen, *J. Appl. Polym. Sci.* **2004**, *92*, 1302-1309.
[119] Y. Meng, L. Du, S. Tiong, Q. Zhu, A. S. Hay, *J. Polym. Sci A. Polym. Chem.* **2002**, *40*, 3579-3591.
[120] S. Padmanaban, M. Kim, S. Yoon, *J. Ind. Eng. Chem.* **2019**, *71*, 336-344.
[121] S. Klaus, M. W. Lehenmeier, E. Herdtweck, P. Deglmann, A. K. Ott, B. Rieger, *J. Am. Chem. Soc.* **2011**, *133*, 13151-13161.
[122] D. J. Darensbourg, *Chem. Rev.* **2007**, *107*, 2388-2410.
[123] Y.-Q. Zheng, J.-L. Lin, H.-L. Zhang, *Z. Kristallogr. NCS* **2000**, *215*, 535-536.
[124] J.-S. Kim, H. Kim, M. Ree, *Chem. Mater.* **2004**, *16*, 2981-2983.
[125] R. Eberhardt, M. Allmendinger, M. Zintl, C. Troll, G. A. Luinstra, B. Rieger, *Macromol. Chem. Phys.* **2004**, *205*, 42-47.
[126] M. H. Chisholm, D. Navarro-Llobet, Z. Zhou, *Macromolecules* **2002**, *35*, 6494-6504.
[127] J.-S. Kim, M. Ree, S. Lee, W. Oh, S. Baek, B. Lee, T. J. Shin, K. Kim, B. Kim, Lüning, *J. Catal.* **2003**, *218*, 386-395.
[128] M. Ree, Y. Hwang, J.-S. Kim, H. Kim, G. Kim, H. Kim, *Catal. Today* **2006**, *115*, 134-145.
[129] S. Wang, L. Du, X. Zhao, Y. Meng, S. Tjong, *J. Appl. Polym. Sci.* **2002**, *85*, 2327-2334.
[130] M. Ree, J. Bae, J. Jung, T. Shin, *J. Polym. Sci.,Part A: Polym. Chem.* **1999**, *37*, 1863-1876.
[131] M. Kobayashi, S. Inoue, T. Tsuruta, *J. Polym. Sci Polym. Chem. Ed.,* **1973**, *11*, 2383-2385.
[132] J. S. Kim, H. Kim, J. Yoon, K. Heo, M. Ree, *J. Polym. Sci. A Polym. Chem.* **2005**, *43*, 4079-4088.
[133] Q. Zhu, Y. Z. Meng, S. C. Tjong, X. S. Zhao, Y. L. Chen, *Polym. Int.* **2002**, *51*, 1079-1085.
[134] J. Wang, Q. Zhu, X. Lu, Y. Meng, *Eur. Polym. J.* **2005**, *41*, 1108-1114.
[135] L. Gao, Y. Luo, Y. Lin, T. Su, R. Su, J. Feng, *J. Polym. Res.* **2015**, *22*, 1-7.

Chapter 2:

Synthesis of Copper based Colloidal Nanoparticles by Organometallic Reactivity

2 SYNTHESIS OF COPPER BASED COLLOIDAL NANOPARTICLES BY ORGANOMETALLIC REACTIVITY

2.1 BACKGROUND AND SCOPE

Earth-abundant and inexpensive Cu-based nanoparticles (NPs) are attractive in catalysis as they show variable accessible oxidation states (Cu^{0-III}).[1] Different synthetic strategies, and/or post synthetic treatments allow for fine tuning of their chemical and physical properties.[1]

Cu-based NPs tend to be synthesised *via* bottom-up approaches as this enables better shape and size control in comparison to top-down methods.[1] Wet chemical techniques are well established to make such NPs. These protocols generally entail the reduction of Cu(II) salts (i.e. $CuSO_4$, $Cu(C_5H_7O_2)_2$, $CuCl_2$, or $Cu(NO_3)_2$) with sodium borohydride, hydrazine, 1,2-hexadecanediol, glucose, ascorbic acid, CO or boranes.[2-5] These processes tend to require high temperatures (>100 °C), form salt by-products and require excess ligand.

Alternatively, Cu(0) NPs can be synthesised *via* low temperature hydrogenolysis of an organometallic copper precursor, such as isobutyrate copper(II); ($[Cu\{CHCOO(CH_3)_2\}_2]$), mesityl copper(I), CuMes (Mes = C_6H_2-2,4,6-Me_3), or *N,N'*-diisopropylacetamidinato copper(I); ($[Cu_2(^iPr NH)_2(CHCH_3)]_2$) in the presence of a surface capping ligand (i.e. alkylamines or carboxylic acids) in an organic solvent (i.e. toluene, THF or anisole).[6] The key advantages of an organometallic approach to NP synthesis are: (1) Low temperature reaction conditions, since the organometallic precursors do not require thermal decomposition, (2) volatile reaction by-products, such as mesitylene, can be removed easily, and (3) substochiometric quantities of surface capping ligands is advantageous for heterogeneous catalysis as fully saturated surfaces block active sites (see Chapter 1 – Introduction, *vide supra*).

The, treatment of a toluene solution of mesitylcopper(I) with substoichoimetric amounts of a long chain primary amine, such as dodecylamine or octylamine, under 4 bar H_2 pressure with heating to 100 °C, yielded colloidal Cu NPs that are 3 to 5.5 nm in size (Scheme 2.1).[7]

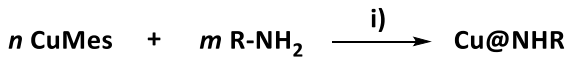

Scheme 2.1. Synthesis of stable colloidal Cu NPs capped with alkylamine ligands. i) Toluene, H_2.[7]

Previously our team synthesised well-defined, ultra-small (~2 nm) colloidal Cu(0) NPs, capped by substochiometric amounts of a phosphinate ligand, $[(C_8H_{17})_2PO_2]^-$. The NPs were prepared by reducing mesityl copper(I) with H_2 at 110 °C, in the presence of di(octyl)phosphinic acid.[8] The use of phosphinate ligands allowed *in-situ* reaction monitoring *via* ^{31}P NMR spectroscopy, which indicated the formation of minor Cu-phosphinate complexes and mesitylene prior to the formation of phosphinate capped Cu(0) nanoparticles *via* hydrogenation.[8] Subsequent oxidation of colloidal Cu(0) NPs to Cu_2O was achieved through exposure to air, at 25 °C, overnight. Cu(0) NPs were regenerated by exposing the Cu_2O NPs to H_2. By repeating cycles of exposure to air and H_2 gases, it was feasible to achieve redox cycling.[8]

Cu_2O NPs are potential photocatalysts for the conversion of CO_2 to methanol as they show strong visible light absorption, have a small band gap energy (2.1 eV) and well-suited band edges potentials (valence band 1, conducting band –1.1 V vs. NHE, pH 0).[9,10] Future economically feasible pathways to form large-area films is desirable (see Chapter 1 – Introduction). In this context, the formation of stable colloidal solutions of Cu_2O NPs, in common organic solvents is a useful target. Here, the aim is to study the stability of colloidal Cu-based NPs as a function of surface capping ligand identity, as well as to understand the properties such ligands impart onto the resulting nanoparticulate materials, such as ligand binding strength, thermal ligand removal and their solubility in common organic solvents.

First, the impact of the donor ligands on the formation and stability of colloidal Cu and Cu_2O NPs will be investigated. Specifically, a sulphur-containing dithiocarboxylate ligand (dithiononanoate, $[L_1^{S2}]^-$) and oxygen-containing carboxyate ligands will be deployed (nonanoate, $[L_1^{O2}]^-$ or 2-[2-(2-methoxyethoxy)ethoxy]acetate, $[L_2^{O2}]^-$). By keeping the ligand chain consistent and only changing the donor atoms of the ligand between $[L_1^{S2}]^-$ and $[L_1^{O2}]^-$, it may be possible to understand how the donors impact the formation of stable, colloidal nanoparticles. To understand the stability of the NP-ligand interactions ligand exchange reactions will be performed. These will be conducted by treating solutions of Cu and Cu_2O NPs capped with *O*-containing carboxylate ligands ($Cu@L_1^{O2}$ or $Cu_2O@L_1^{O2}$) with an equivalent amount of an *S*-containing dithiocarboxylic acid (HL_1^{S2}). Second, as ligand coordination consumes potentially catalytically active sites on the NP surface, its removal while retaining NP size, morphology and identity is required. Therefore, thermal ligand removal and degradation will be surveyed on the Cu_2O NPs. Ligands of varied chains, such as long alkyl or polyether-containing ligands, will be investigated; the latter are anticipated to thermolyse off at lower temperatures because decomposition products consisting of carbon and oxygen are expected to be more volatile than carbon-based products are. Finally, the effects of ligand polarity on NP solubility and subsequent formation of highly concentrated solutions in common organic solvents will be evaluated. Powder X-ray diffraction, IR, UV-Vis and X-ray photoelectron spectroscopy (XPS), and thermal gravimetric analysis (TGA) have been used for nanoparticle characterisation and reaction monitoring.

2.2 Results and Discussion

2.2.1 Synthesis and Characterization of Cu@L nanoparticles

Mesitylcopper(I) (CuMes) is a suitable metal precursor for accessing colloidal copper-containing nanoparticles as the mesityl ligand readily undergoes protonolysis with carboxylic or dithiocarboxylic acids to form mesitylene, an unreactive hydrocarbon byproduct, and afford a carboxylate or dithiocarboxylate ligand, respectively. CuMes was prepared on a multigram scale (>5 g) from cuprous chloride and mesitylmagnesium bromide. Alternatively, commercially CuMes was recrystallised from toluene prior to use.

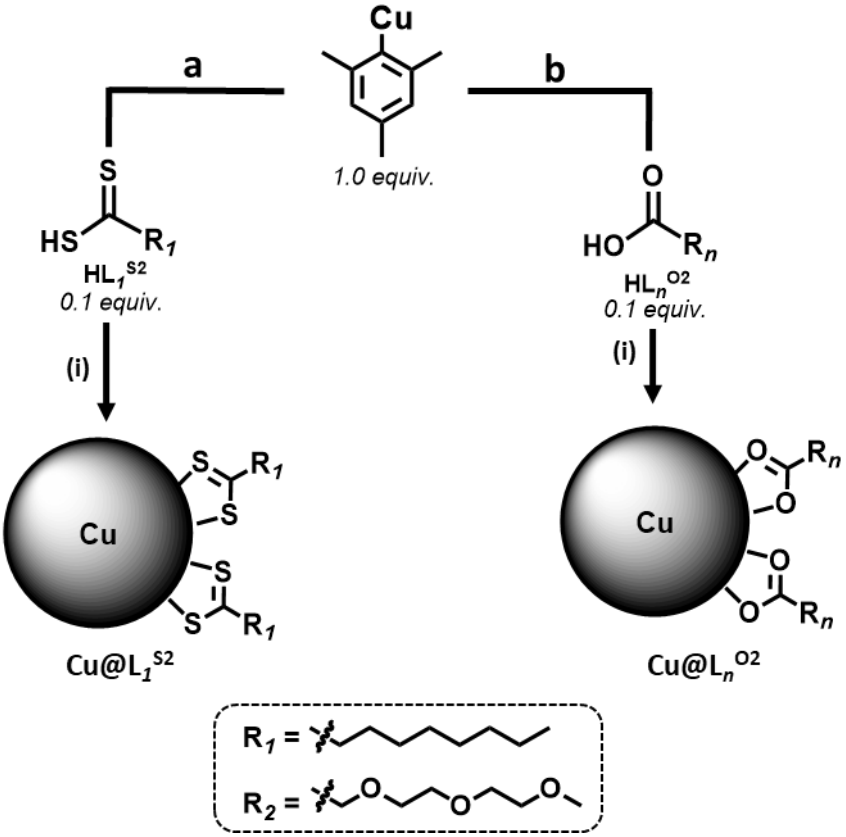

Scheme 2.2. Representation of the synthesis of colloidal Cu@L_1^{S2} (a) and Cu@L_n^{O2} (b, n = 1 or 2) from CuMes and the appropriate proteo-ligand in toluene; i) 3 bar H_2, 110 °C, 2.5 h. [Cu] = 36 mM.

Colloidal Cu@L (L = ligand) nanoparticles were synthesised by treating a toluene solution of CuMes with 0.1 equiv. of the appropriate proteo-ligand (nonanoic acid; HL_1^{O2}, 2-[2-(2-methoxyethoxy)ethoxy]acetic acid HL_2^{O2} or dithiononanoic acid; HL_1^{S2}) and heating under a hydrogen

atmosphere (3 bar; **Figure 2.2**). Cu@L_1^{X2} (X = O or S) were purified *via* precipitation from toluene with acetone. Cu@L_2^{O2} was used without further purification as the particles remain soluble in acetone, hampering further purification.

Carboxylate ligands are well-known for stabilising metal and metal oxide nanoparticles through covalent binding to the particle surface. Apolar nonanoic acid (HL_1^{O2}) and a polar polyether-containing carboxylic acid, 2-[2-(2-methoxyethoxy)ethoxy]acetic acid (HL_2^{O2}), were selected as suitable proteo-ligands; varying the ligand chain polarity from an alkyl group in HL_1^{O2} to an oligoether group in HL_2^{O2} allows insights into how ligand polarity affects both NP solubility in common organic solvents, and thermal ligand removal. The sulphur-containing analogue, HL_1^{S2}, was also utilised.

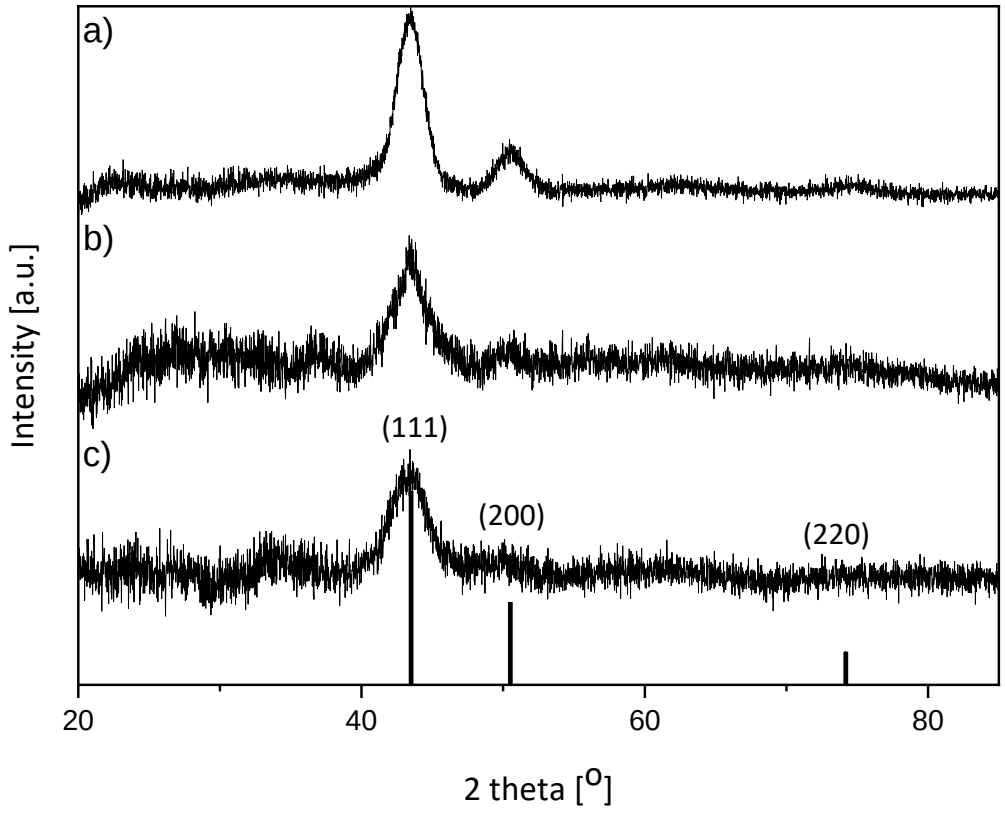

Figure 2.1. Powder X-ray diffraction patterns for a) Cu@L_1^{O2}, b) Cu@L_2^{O2} and c) Cu@L_1^{S2}. Reference bars: Cu (black, JCPDS card no.: 01-085-1326).

Analysis of the samples by powder X-ray diffraction confirmed the formation of Cu(0) nanoparticles when all three ligands were deployed (i.e. HL_n^{O2}, n = 1, 2; HL_1^{S2}), giving rise to broad diffraction peaks at 44° (111), 51° (200) and 74° (220) 2 theta (**Figure 2.1**). The crystallite size was reproducible and was estimated to be < 4 nm *via* the Scherrer equation for all samples.

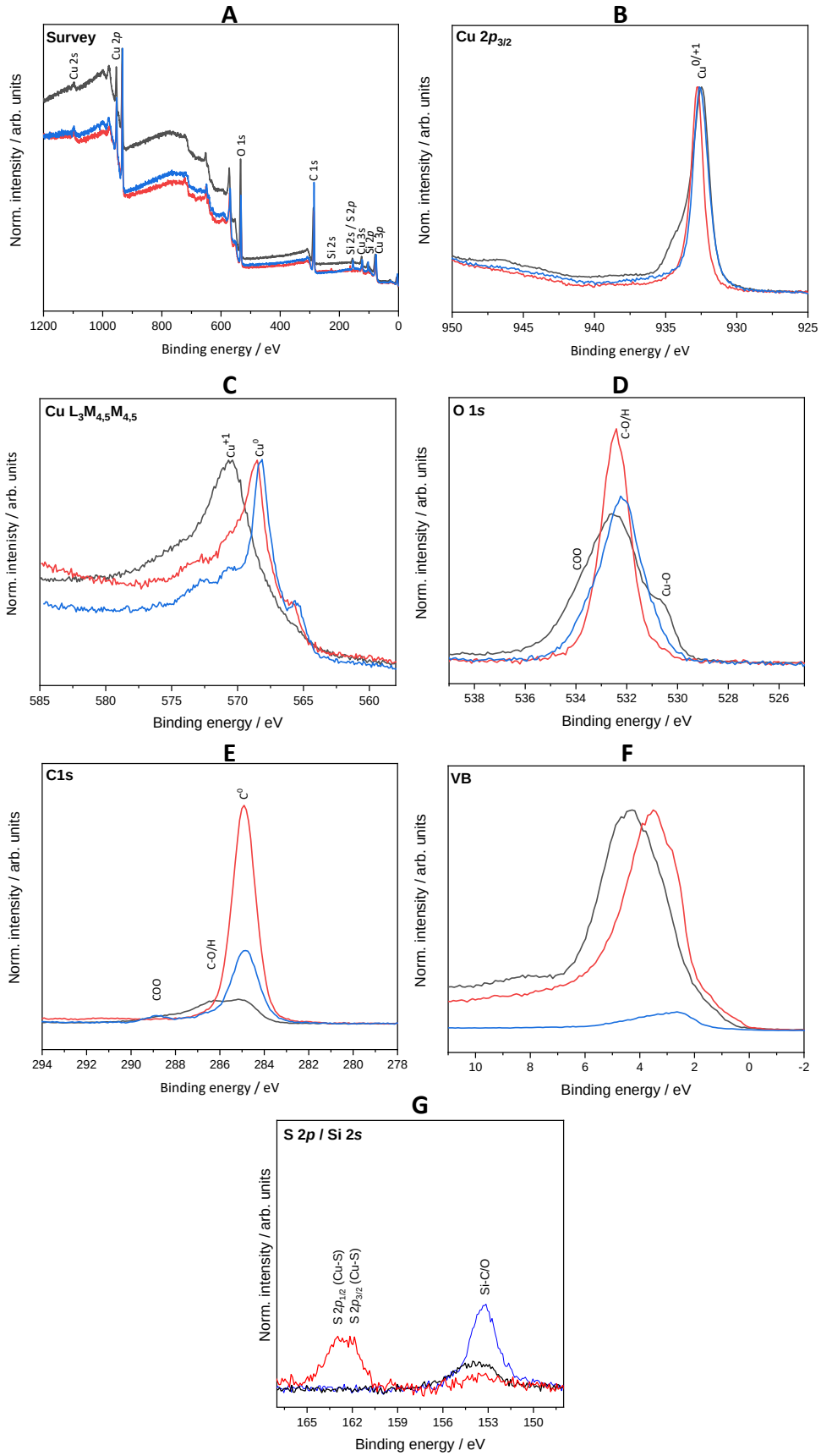

Figure 2.2. XPS spectra for Cu@L_1^{O2} (blue), Cu@L_2^{O2} (black) and Cu@L_1^{S2} (red) nanoparticles; A) survey, B) Cu $2p_{3/2}$, C) $CuL_3M_{4,5}M_{4,5}$ D) O 1*s*, E) C 1*s*, F) valence band spectra and G) S 2*p*/Si 2*s* spectra. Measurements were acquired by Dr Anna Regoutz, UCL.

X-ray photoelectron spectroscopy (XPS) measurements were performed by Dr Anna Regoutz from University College London (UCL). To avoid air exposure and any related alterations of observed chemical environments all samples were transferred to the spectrometer using a special glovebox module. The survey spectra contained the expected peaks corresponding to Cu and the coordinated ligand (Cu 2*p*, O 1*s* and C 1s, **Figure 2.2** A).[11] In addition, unexpected signals attributed to Si were observed, which may derive from silicon grease.[11] The Cu $2p_{3/2}$ core level peaks appear at a binding energy (BE) of 932.7 eV in all samples Cu@L_n^{X2} (n = 1 or 2 and X = O or S), and can be assigned to either Cu(0) or Cu(I) (**Figure 2.2** B).[12] To determine the Cu oxidation states the energy position and line shape of the Cu $L_3M_{4,5}M_{4,5}$ Auger line is analysed. Cu@L_1^{X2} (X = O or S) is composed of metallic Cu(0), whereas for Cu@L_2^{O2} strong lines representing Cu(I) were observed (**Figure 2.2** C), which is in line with data reported for stearate coordinated Cu NPs.[8,13,14] The O 1*s* spectra for Cu@L_n^{O2} (n = 1 or 2) showed COO signals, representing the surface bound carboxylate ligands, and C-O/H environments were observed for the ligand chains.[15,16] Oxidised Cu was again detected for Cu@L_2^{O2}, evidenced by Cu-O environments (**Figure 2.2** D).[12] For Cu@L_1^{S2} the spectra contained only the C-O/H peaks, as expected for a coordinated dithiocarboxylate ligand with an alkyl chain (**Figure 2.2** D). The C 1*s* spectra contained C^0 peaks for all samples which can be attributed to the carbon-containing chains of the coordinated ligands, though adventitious carbon, is always present in this technique.[17,18] Cu@L_n^{O2} (1 or 2) showed additional COO signals from the carboxylate groups of the ligands (**Figure 2.2** E). For the $[L_2^{O2}]^-$ ligand, additional C-O/H signals were also observed (**Figure 2.2** E). From the visible fermi edges, the valence band spectra of Cu@L_1^{X2} (X = O or S) showed evidence of metallic Cu(0) (**Figure 2.2** F). The S 2*p*/Si 2*s* spectra of Cu@L_1^{S2} contained peaks corresponding to Cu-S environments and Si-O/H signals appeared for all samples (**Figure 2.2** G).[19]

Fourier transform infrared spectroscopy (FT-IR) is useful to determine the nanoparticle surface composition since the diagnostic stretches for free and coordinated ligand are easily identified and distinct from one another. As a result, FT-IR spectroscopy is important to verify successful coordination of the selected ligand to the nanoparticle surface.

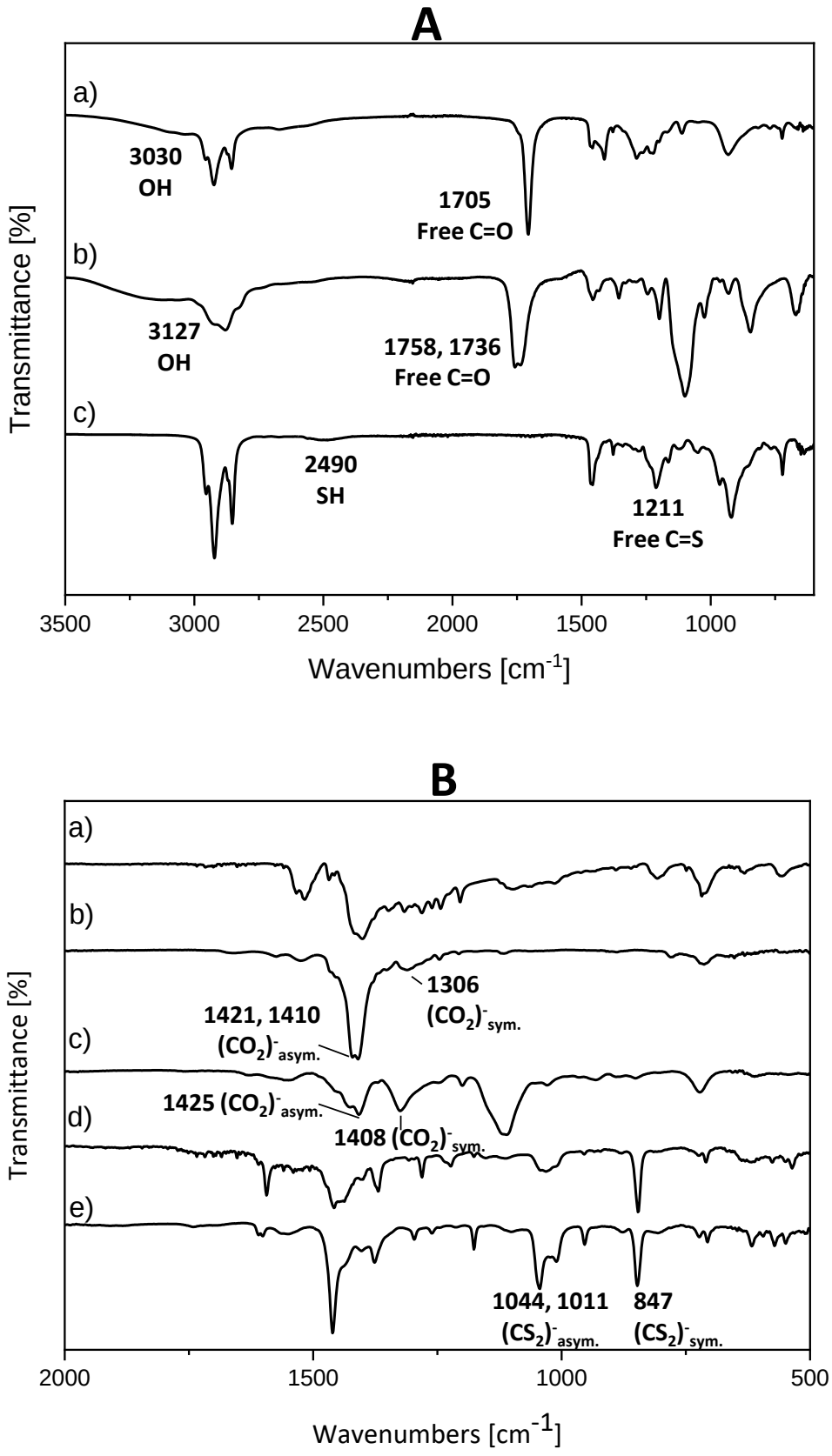

Figure 2.3. Stacked FT-IR spectra. A): a) HL_1^{O2}, b) HL_2^{O2} and c) HL_1^{S2}; B): a) $Cu@L_1^{O2}$, b) $Cu@L_1^{O2}$ after acetone precipitation, c) $Cu@L_2^{O2}$, d) $Cu@L_1^{S2}$, e) $Cu@L_1^{S2}$ after acetone precipitation.

The FT-IR spectra of Cu@L_1^{O2} and Cu@L_1^{S2} are plotted both as crude products and after precipitation to demonstrate how the product purity was improved (compare spectra Ba with Bb and spectra Bd with Be in **Figure 2.3**). Cu@L_n^{O2} (n = 1 or 2) and Cu@L_1^{S2} do not contain stretches associated with the free carboxylic acid (HL_1^{O2}, 3030 cm^{-1} (ν O-H), 1705 cm^{-1} (ν C=O),

Figure 2.3 Aa; HL_2^{O2}, 3127 cm^{-1} (ν O-H), 1758/1736 cm^{-1} (ν C=O), **Figure 2.3** Ab, or dithiocarboxylic acid (HL_1^{S2}, 2490 cm^{-1} (ν S-H), 1211 cm^{-1} (ν C=S), **Figure 2.3** Ac), indicating the carboxylic and dithiocarboxylic acids are fully converted to Cu-carboxylates. Asymmetric and symmetric stretches for the coordinated $[CO_2]^-$ and $[CS_2]^-$ moieties were observed at 1421/1410 ($\nu_{asym}CO_2^-$) and 1306 ($\nu_{sym.}CO_2^-$) cm^{-1} for Cu@L_1^{O2} (**Figure 2.3** Bb), at 1425 ($\nu_{asym.}CO_2^-$) and 1408 ($\nu_{sym.}CO_2^-$) cm^{-1} for Cu@L_2^{O2} (**Figure 2.3** Bc), and 1044/1011 ($\nu_{asym.}CS_2^-$) and 847 ($\nu_{sym.}CS_2^-$) cm^{-1} for Cu@L_1^{S2} (**Figure 2.3** Be).

The asymmetric and symmetric stretches for metal-coordinated carboxylate ligands typically range from 1620–1560 and 1440–1310 cm^{-1}, respectively. Those for metal-coordinated dithiocarboxylate ligands from 1140–1020 and 970–815 cm^{-1}, respectively.[20,21] Such ranges are reported for discrete Cu(carboxylate) complexes and may shift upon nanoparticle coordination.

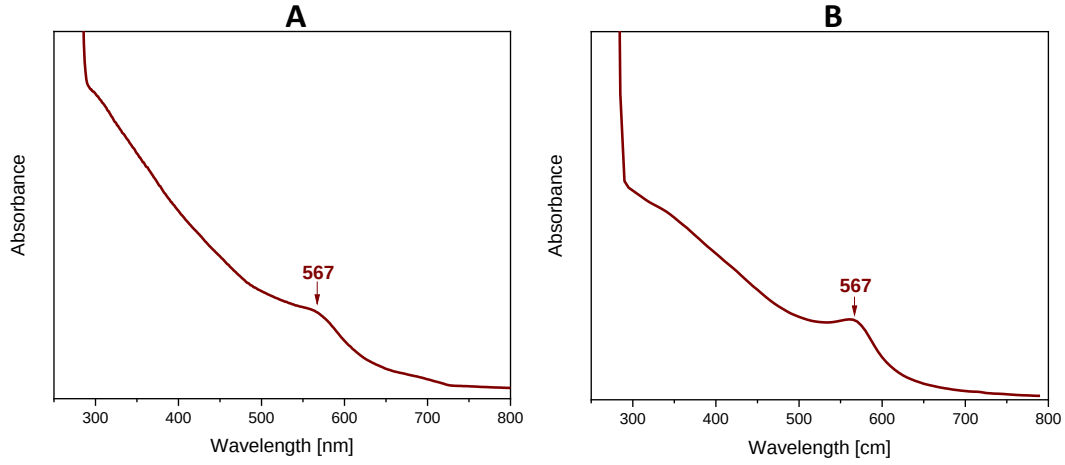

Figure 2.4. UV-Vis spectra of 0.5 mM toluene solutions of: A) Cu@L_1^{O2} and B) Cu@L_2^{O2}.

UV-Vis spectroscopy of the red colloidal solutions of Cu@L_n^{O2} (n = 1, 2) showed a characteristic surface plasmon resonance (SPR) characteristic of nanosized Cu(0) centred at 567 nm (**Figure 2.4**).[8]

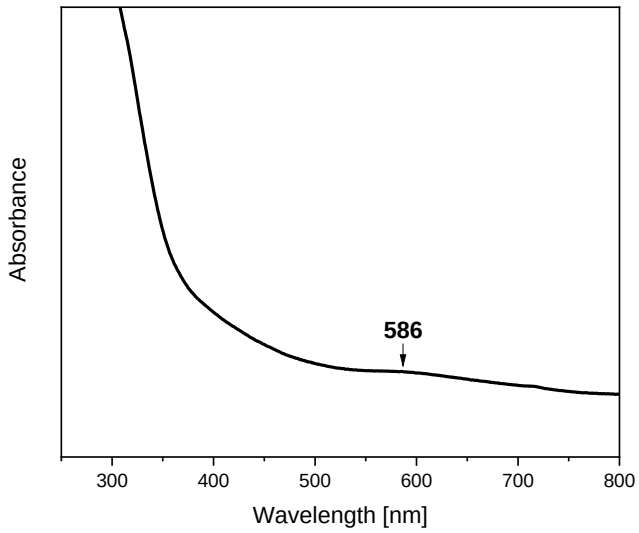

Figure 2.5. UV-Vis spectrum of a 0.5 mM toluene solution of Cu@L_1^{S2}.

Solutions of Cu@L_1^{S2} in toluene appeared black as opposed to red and the UV-Vis spectrum displayed plasmon resonance at 586 nm (**Figure 2.5**). A shift of the plasmon peak to higher wavelength in the present of an *S*-containing ligand (thiolate) in comparison to carboxylates has been reported for Cu(0) nanoparticle before and was attributed to the formation of a strong bond between the sulphur atom and the copper surface.[22]

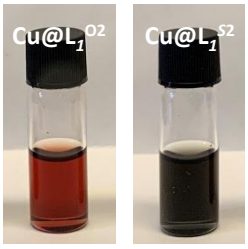

Figure 2.6. Solution of Cu@L_1^{O2} (left), representative for Cu nanoparticles coordinated by carboxylates, and Cu@L_1^{S2} (right).

All Cu colloids were found to be stable over several weeks when stored under an N_2 atmosphere at room temperature. This contrasts reports by Rohner and co-workers who found Cu nanoparticles stabilised by an *S*-containing ligand (i.e. dodecanethiol) to be metastable due to partial conversion to Cu_2S by α–β-elimination of the ligand.[23]

2.2.2 SYNTHESIS AND CHARACTERISATION OF Cu_2O@L NANOPARTICLES

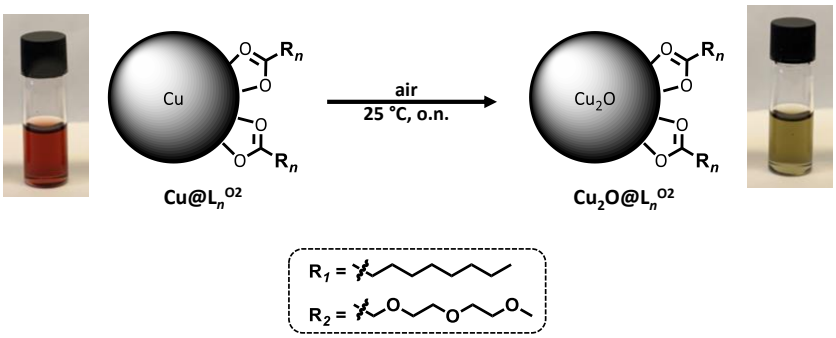

Figure 2.7. Formation of $Cu_2O@L_n^{O2}$ by oxidation of $Cu@L_n^{O2}$ in air at room temperature (n = 1 or 2).

Exposure of colloidal solutions of $Cu@L_n^{O2}$ (n = 1 or 2) to air, with stirring overnight, at room temperature, produced a colour change from deep red to yellow green, indicative of oxidation to Cu_2O (**Figure 2.7**). The $Cu_2O@L_1^{O2}$ was purified and isolated by precipitation from a toluene solution, whereas $Cu_2O@L_2^{O2}$ was isolated by evaporating the toluene solution to dryness. The Cu_2O NP colloids were stable in toluene, at room temperature for weeks.

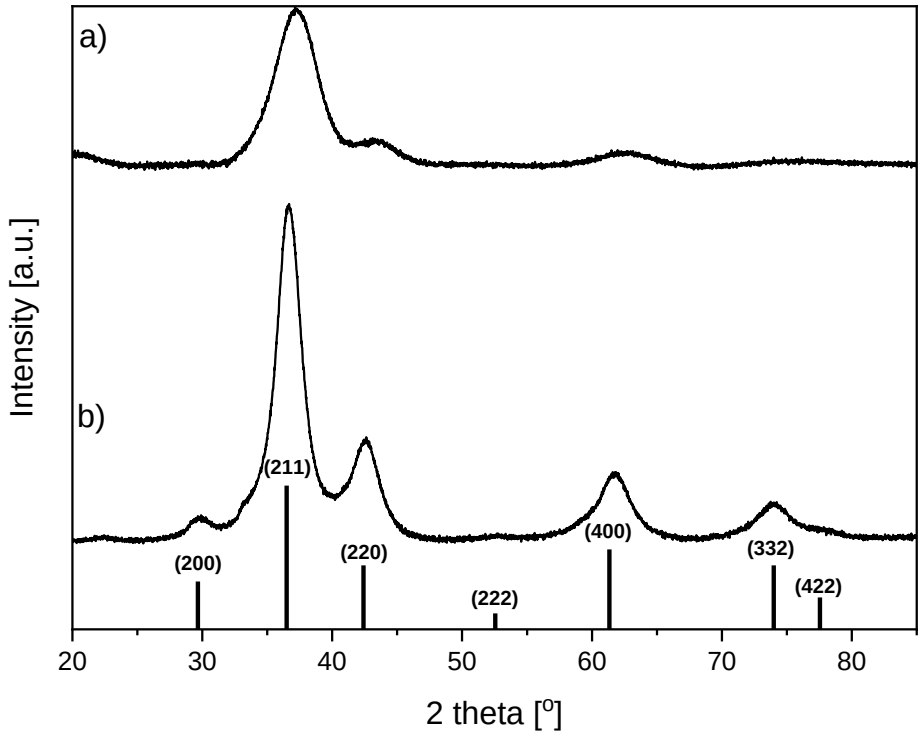

Figure 2.8. Powder XRD patterns of a) $Cu_2O@L_1^{O2}$ and b) $Cu_2O@L_2^{O2}$. The particles were found to be 2.2 and 3.1 nm in size *via* a Scherrer analysis. Patterns are indexed against Cu_2O as black vertical bars (JCPDS card no.: 00-002-1067).

The powder X-ray diffraction patterns confirmed the formation of $Cu_2O@L_n^{O2}$ (n = 1 or 2) nanoparticles, with broad diffraction peaks observed at 30° (200), 37° (211), 42° (220), 53° (222), 61° (400) and 74° (332) 2 theta (**Figure 2.8**). The average particle size of $Cu_2O@L_1^{O2}$ was 2.4 nm, whereas that for $Cu_2O@L_2^{O2}$ was 3.1 nm, as determined using the Scherrer analysis.

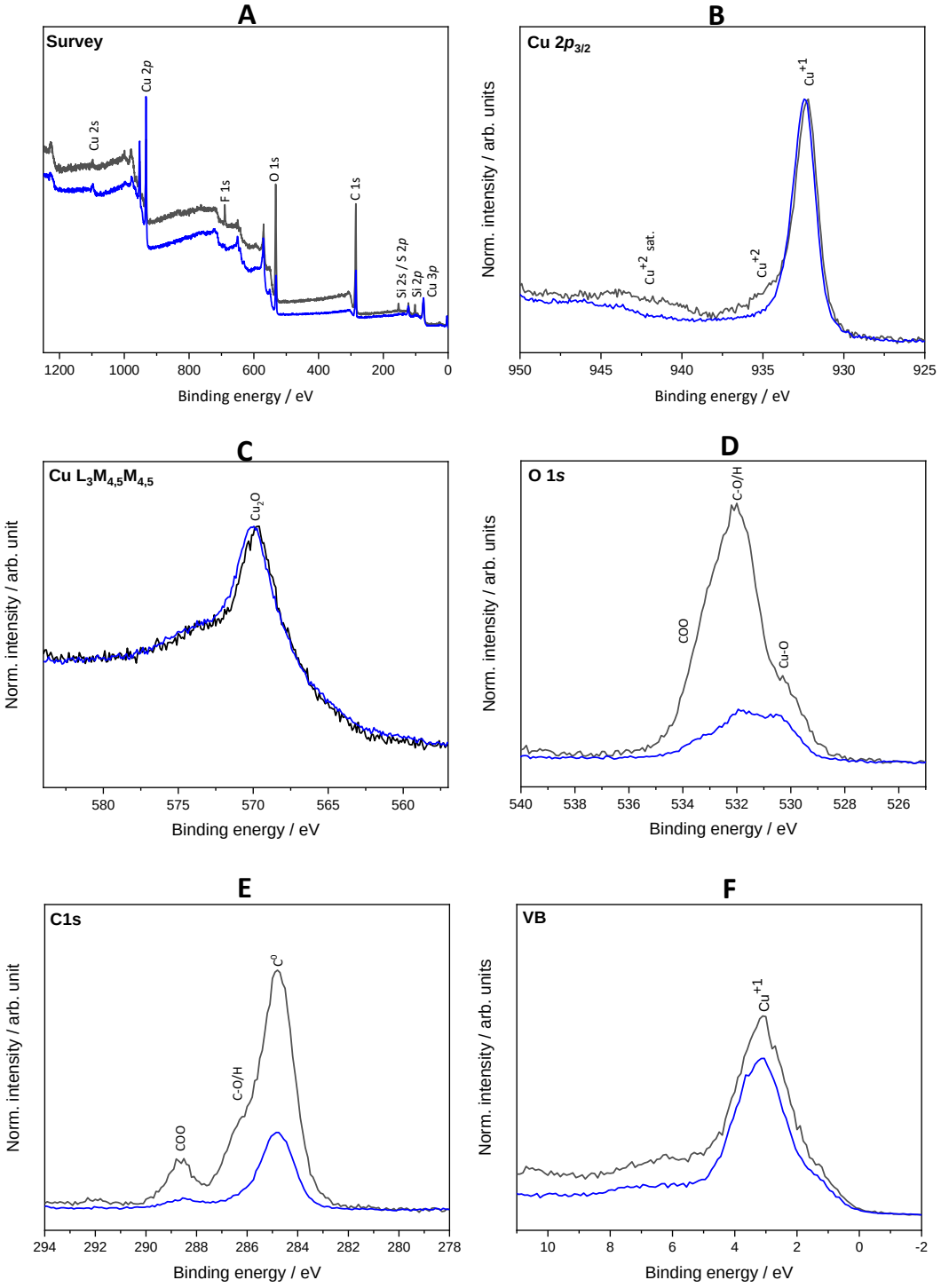

Figure 2.9. XPS spectra of $Cu_2O@L_1^{O2}$ (blue) and $Cu_2O@L_2^{O2}$ (black) nanoparticles. A) Survey, B) Cu $2p_{3/2}$, C) Cu $L_3M_{4,5}M_{4,5}$ D) O 1*s*, E) C 1*s* and F) valence band. Measurements acquired by Dr Anna Regoutz, UCL.

The composition and oxidation state of $Cu_2O@L_n^{O2}$ (n = 1 or 2) samples was also confirmed using X-ray photoelectron spectroscopy (XPS, **Figure 2.9**). The survey spectra showed the expected signals for Cu and the ligands (Cu 2*p*, O 1*s* and C 1*s*, **Figure 2.9** A).[11] In addition, samples contained unexpected lines for Si again and fluorine for $Cu_2O@L_2^{O2}$.[11] The Cu $2p_{3/2}$ core level peaks arising from Cu(I/0) dominated, however, the XPS spectrum for $Cu_2O@L_2^{O2}$ also contained small amounts of Cu(II), as indicated by a shoulder on the higher binding energy side and Cu(II) satellites, as seen in similar systems (**Figure 2.9** B).[8,24,25] The energy and shape of Cu $L_3M_{4,5}M_{4,5}$ Auger lines commensurate with Cu_2O for both samples (**Figure 2.9** C).[13] The O 1*s* spectra showed C-O/H, COO and Cu-O environments for both $Cu_2O@L_1^{O2}$ and $Cu_2O@L_2^{O2}$, resulting from the ligand chains, the carboxylates and oxidised Cu, respectively (**Figure 2.9** D). The C 1s spectra contains the peaks for carboxylate (COO), adventitious carbon and a C-O/H signal for L_2^{O2} (**Figure 2.9** E).[17] Finally, the valence band spectra confirmed the Cu oxidation and chemical states, in which $Cu@L_n^{O2}$ undergoes oxidation to $Cu_2O@L_n^{O2}$ (n = 1 or 2) in air (**Figure 2.9** F).

Oxidation of Cu(0) NPs to Cu(I), occurs due to the ultra-small size of the starting Cu(0) nanoparticles. Although, CuO (monoclinic lattice) is the thermodynamically most stable oxide by copper under ambient conditions, Cu_2O (face-centred cubic (fcc) lattice) is it at the nanoscale. A simple lattice expansion caused by oxygen diffusion into the fcc lattice of Cu(0) if preferred over the formation of a monoclinic lattice.[8]

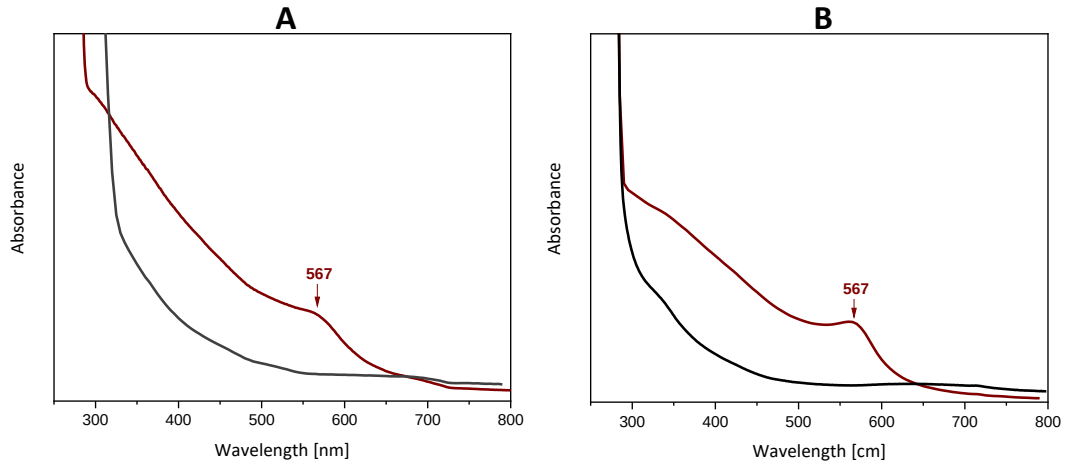

Figure 2.10. Superimposed UV-Vis spectra of: A) $Cu_2O@L_1^{O2}$ (black) and $Cu@L_1^{O2}$ (red), and B) $Cu_2O@L_2^{O2}$ (black) and $Cu@L_2^{O2}$ (red).

Clean oxidation of $Cu@L_n^{O2}$ to $Cu_2O@L_n^{O2}$ (n = 1 or 2) in air was further confirmed by the disappearance of the surface plasmon resonance in the resulting UV-Vis spectra (**Figure 2.10**). Through construction of Tauc plots from the UV-Vis data, the band gaps for $Cu_2O@L_1^{O2}$ and $Cu_2O@L_2^{O2}$ were found to be 2.1 and 2.4 eV, respectively.

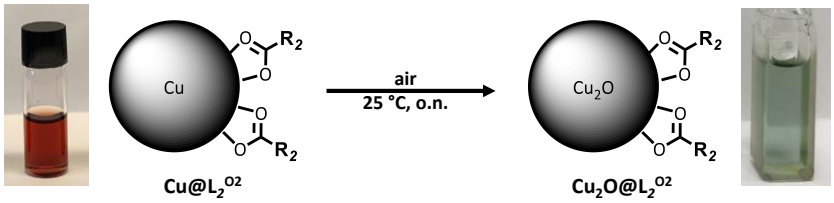

Figure 2.11. Formation of $Cu_2O@L_2^{O2}$ from $Cu@L_2^{O2}$ using O_2.

The oxidation of $Cu@L_2^{O2}$ upon exposure to O_2 was also investigated. Oxygen gas was passed over a toluene solution of $Cu@L_2^{O2}$ for several minutes before sealing the reaction vessel, and stirred under an O_2 atmosphere overnight; an immediate colour change from deep red to deep turquoise was observed **Figure 2.11**.

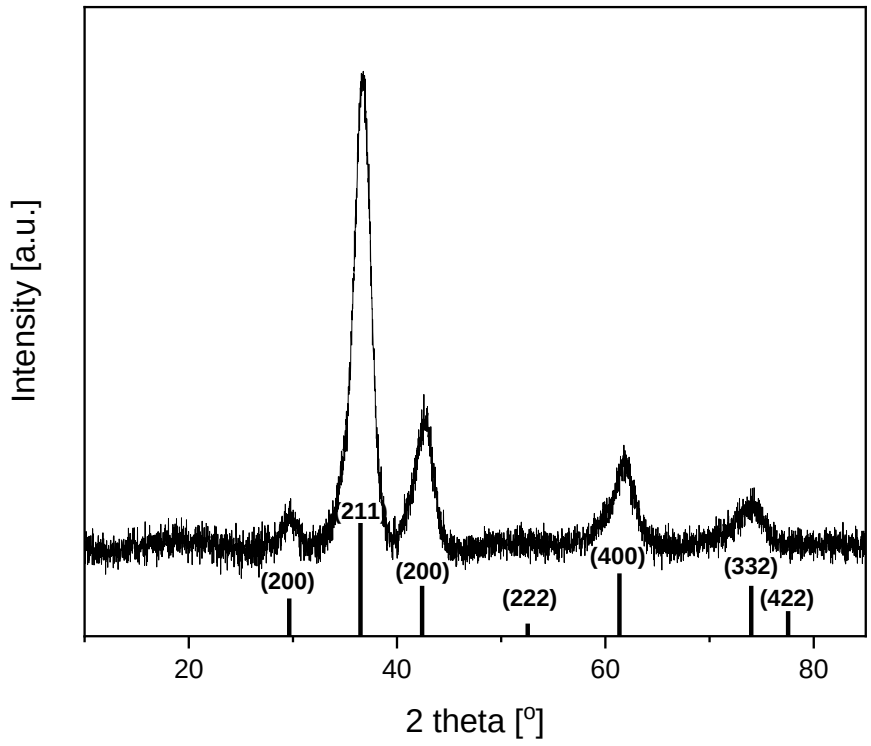

Figure 2.12. Powder XRD patterns of $Cu_2O@L_2^{O2}$ oxidised with O_2; the average particle size was 3.7 nm from the Scherrer equation. Patterns are indexed against Cu_2O as black vertical bars (JCPDS card no.: 00-002-1067).

The produced powder X-ray diffraction pattern showed characteristic reflections of Cu_2O nanoparticles at 30° (200), 37° (211), 42° (220), 52° (222), 61° (400), and 74° (332) 2 theta. No CuO was detected (**Figure 2.12**). The average particle size was 3.7 nm *via* the Scherrer equation, which was close to $Cu_2O@L_2^{O2}$ produced by air oxidation.

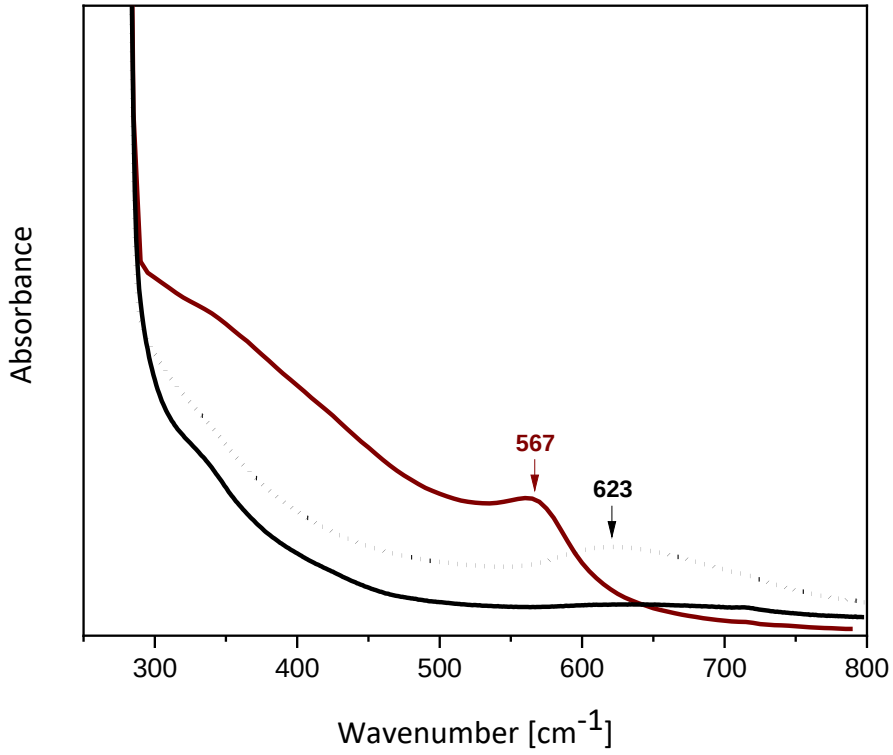

Figure 2.13. Superimposed UV-Vis spectra of $Cu@L_2^{O2}$ (red), $Cu_2O@L_2^{O2}$ obtained by oxidation of $Cu@L_2^{O2}$ in air at room temperature overnight (black, solid line), $Cu_2O@L_2^{O2}$ obtained by oxidation of $Cu@L_2^{O2}$ with O_2 overnight at room temperature (black, dotted line).

The UV-Vis spectrum of $Cu_2O@L_2^{O2}$ (oxidation of $Cu@L_2^{O2}$ with O_2) showed a weak red-shifted SPR centred at 623 nm (**Figure 2.13**, black dotted line). This is in contrast to samples of $Cu_2O@L_2^{O2}$ that were oxidised in air (**Figure 2.13**, black, solid line).

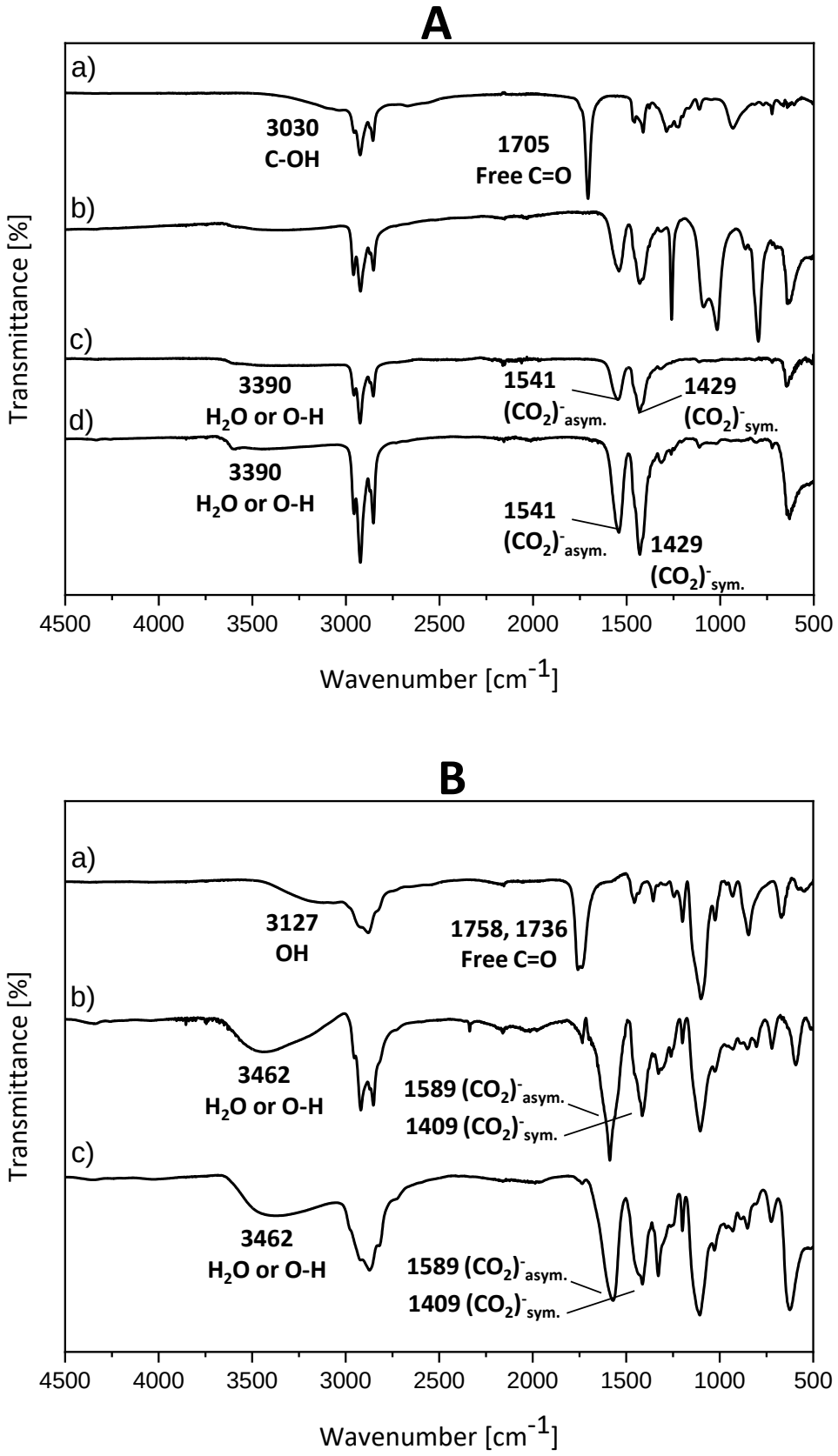

Figure 2.14. Stacked FT-IR spectra of: A) a) HL_1^{O2}, b) $Cu_2O@L_1^{O2}$ oxidised in air, c) $Cu_2O@L_1^{O2}$ oxidised in air and precipitated with acetone, d) $Cu_2O@L_1^{O2}$ oxidised with O_2 B) a) HL_2^{O2}, b) $Cu_2O@L_2^{O2}$ oxidised in air, c) $Cu_2O@L_2^{O2}$ oxidised with O_2.

No stretches associated with free carboxylic acid were observed in the FT-IR spectra, indicating the carboxylate ligands $[L_n^{O2}]^-$ (n = 1 or 2) remained bound to the particle surface in all cases (**Figure 2.14**). Instead, the resulting FT-IR spectra contained asymmetric and symmetric CO_2^- stretches at 1541 and 1429 cm^{-1} for $Cu_2O@L_1^{O2}$, and 1589 and 1409 cm^{-1} for $Cu_2O@L_2^{O2}$ respectively.

Strong stretches, at 3390 for $Cu_2O@L_1^{O2}$ and 3462 cm^{-1} for $Cu_2O@L_2^{O2}$, were also observed in the resulting FT-IR spectra, and are diagnostic of O-H stretches associated with either surface coordinated water or hydroxyl moieties. Given the hydrophilic nature of the $[L_2^{O2}]^-$ ligand, it is perhaps not surprising that these stretches are more intense for $Cu_2O@L_2^{O2}$ than for $Cu_2O@L_1^{O2}$, which is coordinated by the hydrophobic $[L_1^{O2}]^-$ ligand (**Figure 2.14** Ac and Bb).

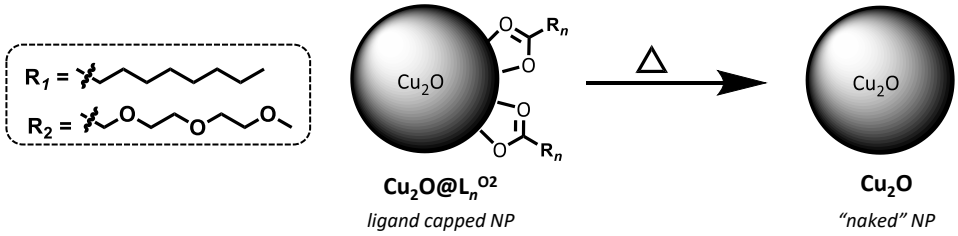

Scheme 2.3. General depiction of thermal ligand removal from the surface of Cu_2O nanoparticles.

$Cu_2O@L_n^{O2}$ (n = 1 or 2) was examined by thermal gravimetric analysis (TGA) to: (1) quantify the amount of ligand coordinated to the nanoparticle surface, and (2) determine the temperature for complete ligand removal (**Figure 2.3**).

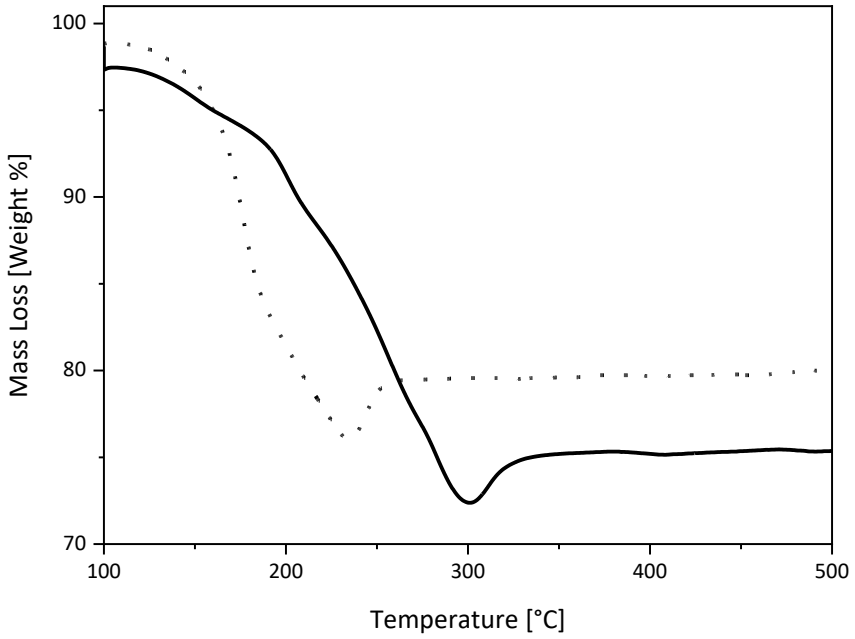

Figure 2.15. TGA of $Cu_2O@L_1^{O2}$ (solid line) and $Cu_2O@L_2^{O2}$ (dotted line) performed in air.

The data for $Cu_2O@L_1^{O2}$ (in air, **Figure 2.15**, solid line) indicated a ~25 weight % mass loss from 125 to 300 °C, which is close to the calculated 20 weight % mass loss calculated for complete loss of coordinated ligand (10%) and Cu(I)→Cu(0) reduction (10%). The discrepancy of ~5% may due to undesired volatile byproducts formed during the synthesis as the sample was not purified by precipitation from toluene with acetone. The mass increase of ~3 weight % from 300 to 340 °C is indicative for 30% re-oxidation (10% mass increase expected for complete re-oxidation) of Cu(0) to Cu_2O. The data for $Cu_2O@L_2^{O2}$ (in air, **Figure 2.15**, dotted line) was similar, showing an initial mass loss of ~22 weight % from 120 to 230 °C, corresponding to complete ligand removal (11%) and Cu(I)→Cu(0) reduction (10%). The followed mass increase of ~4 weight % from 230 to 260 °C indicated a re-oxidation of 40% of Cu(0) to Cu_2O since 10% mass increase would be expected for complete re-oxidation.

The lower ligand degradation temperature for $Cu_2O@L_2^{O2}$ is attributed to the formation of volatile *O*-containing degradation byproducts during thermal degradation. It may be advantageous for future catalytic or optoelectronic applications to produce 'ligand free' nanoparticle surfaces.[26]

The oxidation of Cu@L_1^{S2} to Cu_2O@L_1^{S2} in air (25°C, overnight) was not successful. Rather, exposure of Cu@L_1^{S2} to air in toluene produced a black precipitate (**Figure 2.16**).

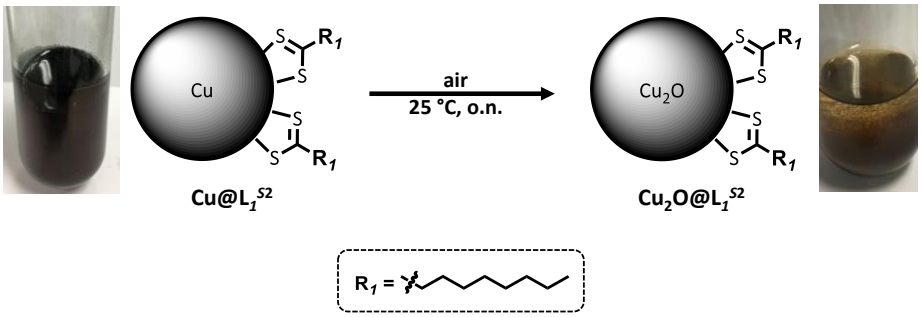

Figure 2.16. Attempted oxidation of Cu@L_1^{S2} in air.

The precipitate was isolated by centrifugation, washed with toluene, and analysed by pXRD and FT-IR spectroscopy (**Figure 2.17**). The powder X-ray diffractogram identified the precipitate as Cu_2O. However, the FT-IR spectrum of the isolated Cu_2O did not contain diagnostic stretches associated with the coordinated dithiocarboxylate ligand, $[L_1^{S2}]^-$ (*vide supra*), indicating they were no longer coordinated to the nanoparticle surface.

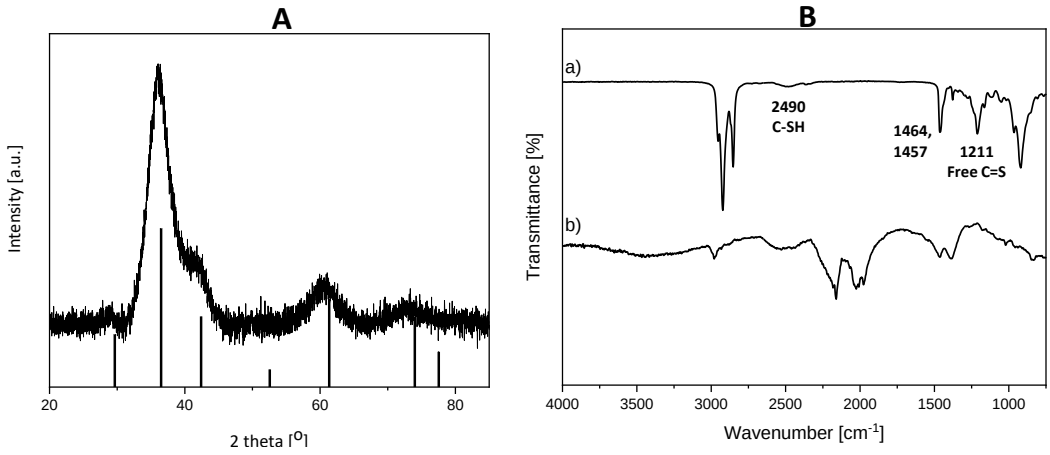

Figure 2.17. A) Powder XRD pattern of isolated precipitate formed when stirring Cu@L_1^{S2} in air overnight. Indexed against Cu_2O as vertical bars (JCPDS card no.: 00-002-1067). B) Stacked FT-IR spectra: a) HL_1^{S2} and b) isolated precipitate.

Therefore, the attempted oxidation of Cu@L_1^{S2} did not yield colloidal Cu_2O nanoparticles. Given this, it was hypothesised that the ligand donor group must be compatible with the surface of the nanoparticles in order to successfully coordinate and provide stable colloidal solutions. To investigate this ligand chemistry in more detail, a series of carboxylate/dithiocarboxylate ligand exchange reactions were investigated.

2.2.3 SURFACE LIGAND CHEMISTRY – LIGAND EXCHANGE REACTIVITY

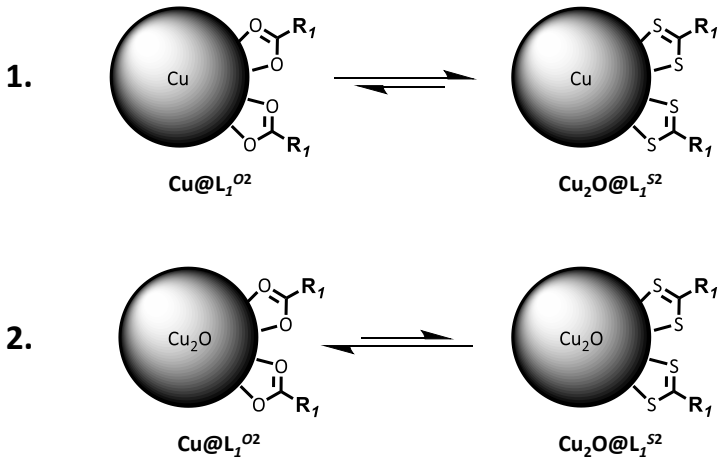

Figure 2.18. Ligand exchange reactivity on the surface of Cu (1., top) and Cu_2O nanoparticles (2., bottom).

The nanoparticles, $Cu@L_1^{O2}$ and $Cu_2O@L_1^{O2}$ are both coordinated by 0.1 equiv. of $[L_1^{O2}]^-$. For the exchange reaction they were treated with 0.1 equiv. HL_1^{S2}. On the other hand, $Cu@L_1^{S2}$, coordinated by 0.1 equiv. of $[L_1^{S2}]^-$, was treated with 0.1 equiv. HL_1^{O2}. UV-Vis and FT-IR spectroscopy were used to evaluate the extent of ligand exchange (**Figure 2.18**). For clarification, the amount of ligand present or expected to be present on the nanoparticle's surface will be given as a subscript in this subsection of the chapter. For example, a Cu nanoparticle coordinated by 0.1 equiv. of $[L_1^{O2}]^-$ will be labelled as $Cu@(L_1^{O2})_{0.1}$.

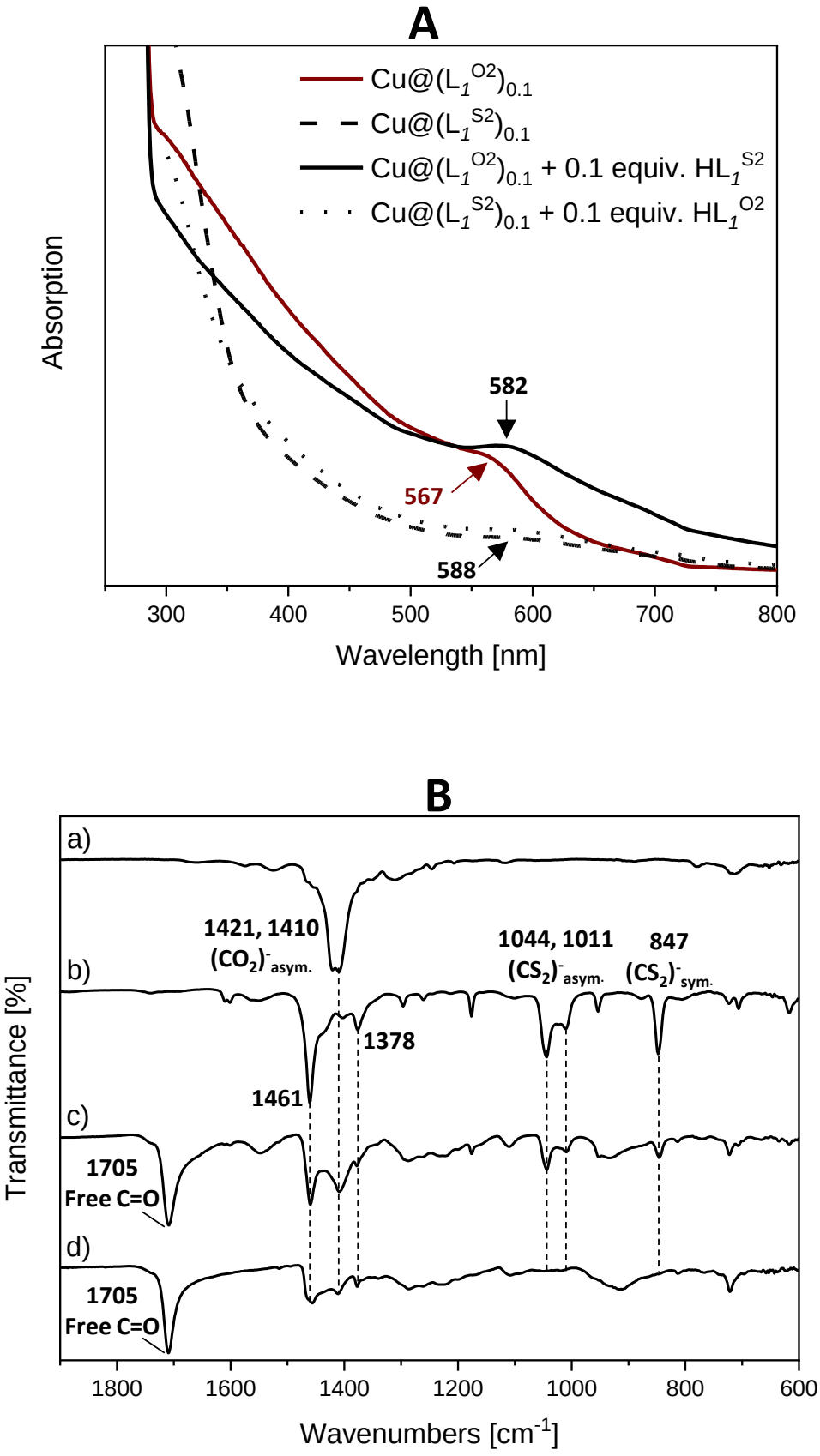

Figure 2.19. A) Superimposed UV-Vis spectra of $Cu@(L_1^{X2})_{0.1}$ (X = O or S), $Cu@(L_1^{O2})_{0.1}$ + 0.1 equiv. HL_1^{S2} and $Cu@(L_1^{S2})_{0.1}$ + 0.1 equiv. HL_1^{O2} B) Stacked FT-IR spectra of a) $Cu@(L_1^{O2})_{0.1}$, b) $Cu@(L_1^{S2})_{0.1}$, c) $Cu@(L_1^{S2})_{0.1}$ + 0.1 equiv. HL_1^{O2}, d) $Cu@(L_1^{O2})_{0.1}$ + 0.1 equiv. HL_1^{S2}.

A toluene solution of Cu@$(L_1^{S2})_{0.1}$ was treated with 0.1 equiv. of HL_1^{O2}. The solution remained black in colour, consistent with retention of Cu@$(L_1^{S2})_{0.1}$ with no ligand exchange occurring. The FT-IR spectrum of the product (**Figure 2.19**, Bc) showed stretches consistent with both Cu@$(L_1^{S2})_{0.1}$ ($\nu_{asym.}CS_2^-$ 1044, 1011 cm^{-1}, **Figure 2.19**, Bb) and Cu@$(L_1^{O2})_{0.1}$ ($\nu_{asym}CO_2^-$ 1421,1410 cm^{-1}, **Figure 2.19**, Ba), and free HL_1^{O2} (ν C=O 1705 cm^{-1}). However, free HL_1^{S2} (ν C=S 1211 cm^{-1}) was not observed. Stretches associated with the CS_2^- moiety of a surface-coordinated dithiocarboxylate ligand were still observable by FT-IR ($\nu_{sym.}CS_2^-$ 847 cm^{-1}). Additionally, stretches at 1461 and 1378 cm^{-1} were present, which have been detected for Cu@$(L_1^{S2})_{0.1}$ before. These data indicate a mixed ligand surface speciation.

The reverse reaction was also examined, that is the addition of 0.1 equiv. of HL_1^{S2} to a solution of Cu@$(L_1^{O2})_{0.1}$ in toluene. Upon the addition of the dithiocarboxylic acid, an immediate colour change from deep red to black was observed, characteristic of the formation of Cu@$(L_1^{S2})_{0.1}$. The resulting UV-Vis spectrum showed a clear red-shift of the SPR from 567 nm to 582 nm, in agreement with the formation of Cu@$(L_1^{S2})_{0.1}$ (588 nm; **Figure 2.19**, A). Free HL_1^{O2} (ν C=O 1705 cm^{-1}) was observed in the resulting FT-IR spectrum (**Figure 2.19**, Bd). The spectrum also showed, asymmetric stretches associated with Cu@$(L_1^{O2})_{0.1}$ ($\nu_{asym}CO_2^-$ 1421,1410 cm^{-1}, **Figure 2.19**, Ba) and stretches at 1461 and 1378 cm^{-1}. However, stretches for free HL_1^{S2} or coordinated CS_2^- moieties were not observed.

Based on these results, the addition of HL_1^{S2} to Cu@$(L_1^{O2})_{0.1}$, and HL_1^{O2} to Cu@$(L_1^{S2})_{0.1}$ most likely provides nanoparticles coordinated by both ligands. One plausible explanation is that 0.1 equiv. of ligand loading is not enough to fully saturate the nanoparticle surface. Nevertheless, the presence of free carboxylic acid, HL_1^{O2}, in combination with the persistence of a black solution for Cu@$(L_1^{S2})_{0.1}$ indicates that the *S*-containing dithiocarboxylate ligand probably binds more strongly to the Cu(0) nanoparticle surface than the *O*-containing carboxylate ligand.

This observation was found to be in line with various inorganic chemistry theories: According to Kepp, who recently proposed the terms 'oxo' and 'thiophilicity' to predict a metals character, classified copper as more 'thiophilic' (~~*S*~~ = 0.8) than oxophilic (~~*O*~~ = 0.2), thus a preferential binding of a *S*-ligand

over an *O*-ligand is expected.[27] Moreover, Cu(0) is classificate as a 'soft' metal according to the HSAB theory and, therefore should prefer the softer *S*-ligand coordinated on its surface.[28] Lastly, replacement of $[L_1^{S2}]^-$ by HL_1^{O2} would have been surprising as protonation of the stronger acid HL_1^{S2} (pK_a= 2.59) by the weaker acid HL_1^{O2} (pK_a= 4.96) is rather unlikely.[29,30]

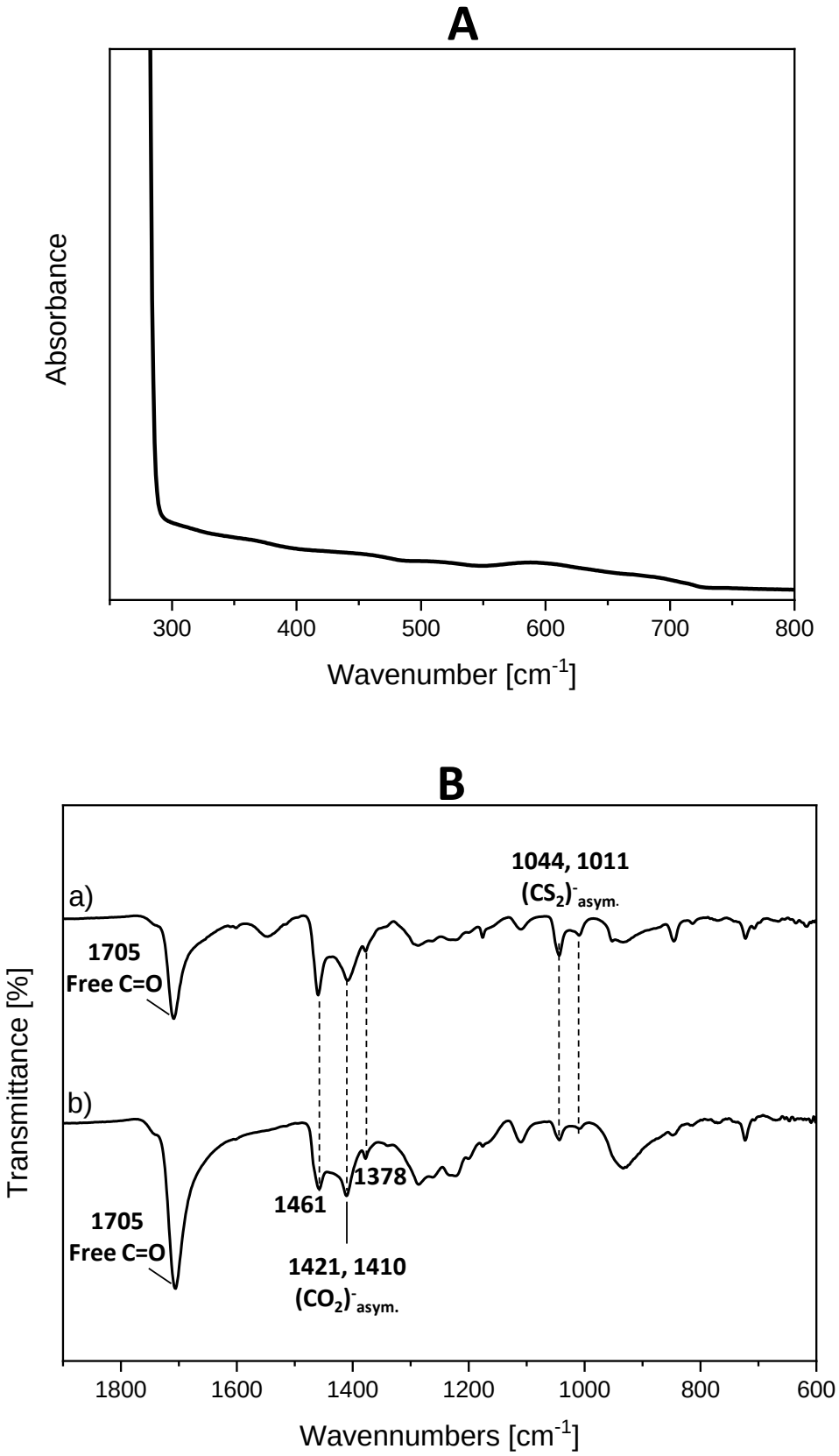

Figure 2.20. A) UV-Vis spectrum of Cu@$(L_1^{S2})_{0.1}$ + 0.5 equiv. HL_1^{O2}. B) Stacked FT-IR spectra of: a) Cu@$(L_1^{S2})_{0.1}$ + 0.1 equiv. HL_1^{O2} and b) Cu@$(L_1^{S2})_{0.1}$ + 0.5 equiv. HL_1^{O2}.

To further probe the influence of ligand loading, excess HL_1^{O2} (0.5 equiv.) was added to $Cu@(L_1^{S2})_{0.1}$. The resulting solution remained black in colour but the UV-Vis spectrum did not give rise to a SPR at 567 nm (**Figure 2.20** A). The FT-IR spectrum contained stretches associated with both $Cu@(L_1^{S2})_{0.1}$ and $Cu@(L_1^{O2})_{0.1}$ along with free HL_1^{O2} (**Figure 2.20**, Bb). The stretch associated with coordinated $[L_1^{S2}]^-$ was also observable and thus the FT-IR spectrum was in good agreement with that of $Cu@(L_1^{S2})_{0.1}$ + 0.1 equiv. HL_1^{O2} (**Figure 2.20**, Ba). This experiment further confirms, that dithiocarboxylate coordination to Cu(0) is favoured, since even excess HL_1^{O2} does not fully replace coordinated $[L_1^{S2}]^-$.

Next, ligand exchange reactivity on $Cu_2O@(L_1^{O2})_{0.1}$ nanoparticles was explored. As $Cu_2O@(L_1^{S2})_{0.1}$ could not be isolated, the addition of the *S*-containing dithiocarboxylic acid (HL_1^{S2}) to $Cu_2O@(L_1^{O2})_{0.1}$ was not expected to displace any of the *O*-containing carboxylate ligand.

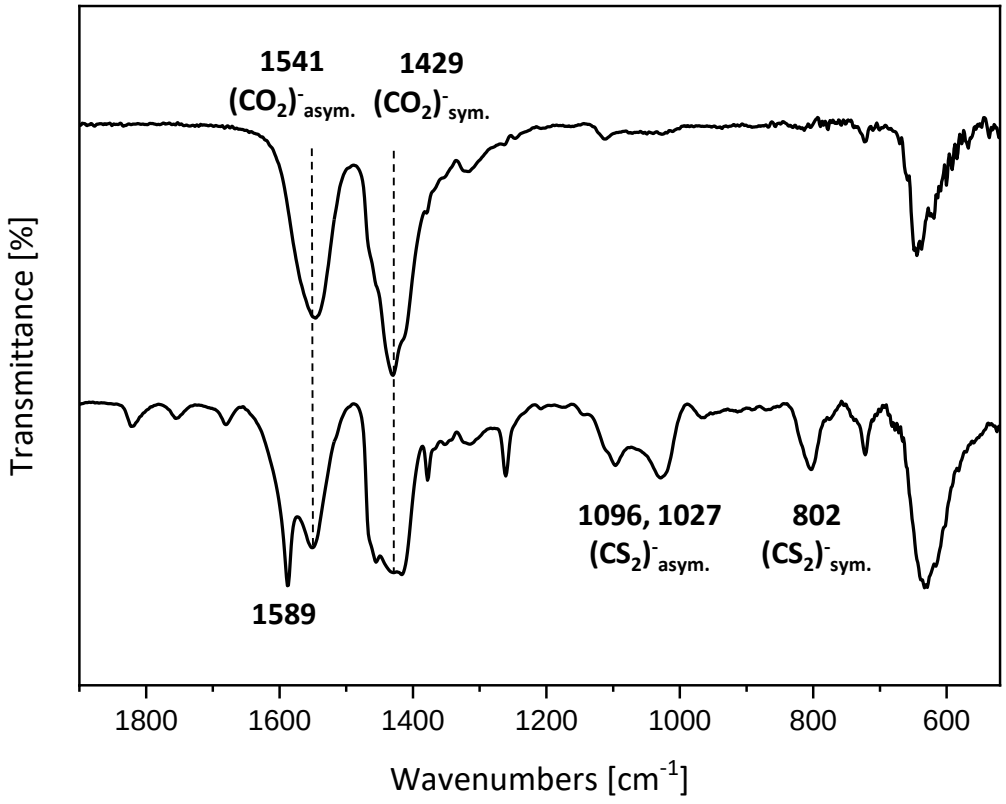

Figure 2.21. FT-IR spectra of $Cu_2O@(L_1^{O2})_{0.1}$ (top) and $Cu_2O@(L_1^{O2})_{0.1}$ + 0.1 equiv. HL_1^{S2} (bottom).

A toluene solution of $Cu_2O@(L_1^{O2})_{0.1}$ was treated with 0.1 equiv. of HL_1^{S2}. The resulting FT-IR spectrum (**Figure 2.21**, bottom) showed stretches associated with surface coordinated carboxylate ligand in a bidentate fashion mode (1541 and 1429 cm^{-1}). No stretches associated with free carboxylic acid (1705 cm^{-1}) were detected, indicating that ligand exchange did not occur. Curiously, stretches associated with free HL_1^{S2} (1211 cm^{-1} for free C=S) were also absent, which may again, indicate that particle surfaces were not saturated and can accommodate the excess ligand. Additional stretches at 1096, 1027 and 802 cm^{-1} may represent asymmetric and symmetric CS_2^- stretches for coordinated $[L_3^{S2}]^-$ ligand. The new sharp stretch at 1589 cm^{-1} might account for carboxylate ligands that changed their coordination mode from bidentate to monodentate upon an increased ligand coverage on the particle surface.

Therefore, this experiment is inconclusive with respect to whether there is an increased propensity for coordination of *O*-containing carboxylate ligands on Cu_2O over *S*-containing dithiocarboxylate ligands. However, the fact that $Cu_2O@(L_1^{S2})_{0.1}$ could not be isolated in carboxylate ligand exchange suggests that *O*-containing ligands are preferentially coordinated at the Cu_2O surface.

Rationalisation of the ligand preferences on Cu_2O was difficult as the 'oxo-' or 'thiophilic' model by Kepp is not accounted to metal oxides and Cu(I) is according to the HSAB concept still classified as a 'soft' metal.[28] However, the preferential binding of the *O*-containing ligand onto the surface of the Cu_2O nanoparticle may derive from the ionic lattice character in Cu_2O, making the Cu(I) sites 'harder' and thus preferentially coordinated by the harder ligand $[L_1^{O2}]^-$.

2.2.4 SOLUBILITY TESTING

A potential application for colloidal solutions of $Cu_2O@L_n^{O2}$ (n = 1 or 2) nanoparticles would be as inks for the deposition of thin films. As such, knowledge regarding their solubility in a range of solvents is important.

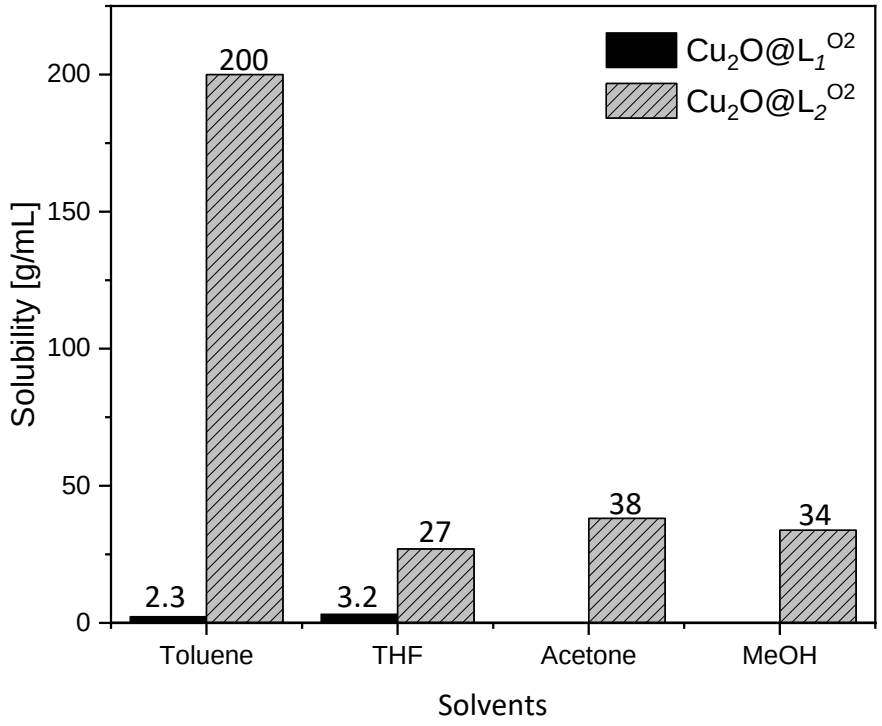

Figure 2.22. Solubility of Cu_2O nanoparticles coordinated by 0.1 equiv. L_n^{O2} (n = 1 or 2) in various organic solvents [g/mL].

The solubility of the nanoparticles was assessed by re-dissolving dried $Cu_2O@L_n^{O2}$ (n = 1 or 2) in solvents with increasing polarity. The re-dispersed colloidal $Cu_2O@L_1^{O2}$ nanoparticles show only low solubility, with maximum solubilities of 2.3, 3.2, 0 and 0 mg/mL in toluene, THF, acetone, and methanol, respectively. On the other hand, colloidal $Cu_2O@L_2^{O2}$ nanoparticles exhibit maximum solubilities of 200, 27, 38 and 34 mg/mL in the same solvents (**Figure 2.22**).

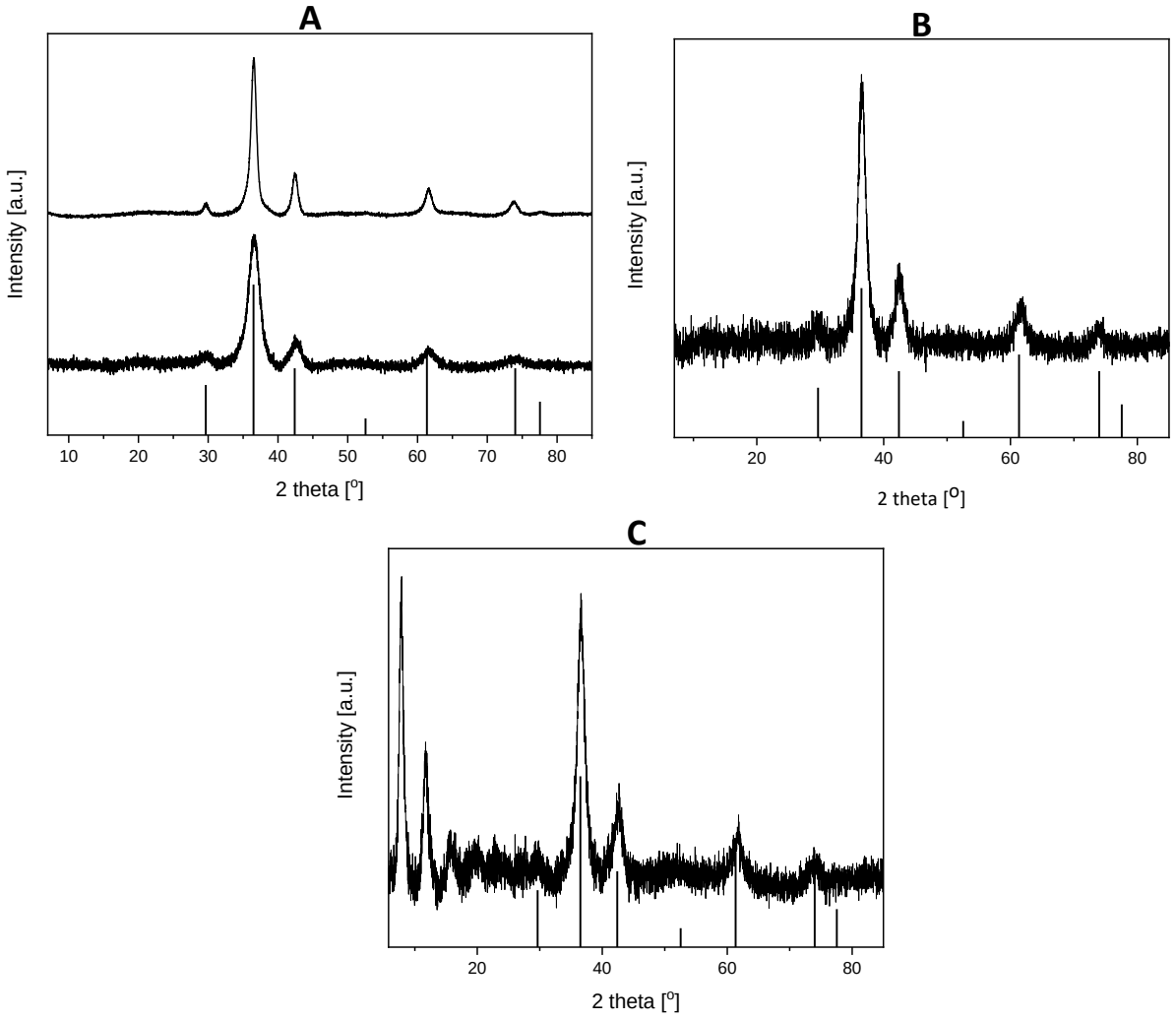

Figure 2.23. Powder X-ray diffraction of Cu_2O nanoparticles. A) $Cu_2O@L_2^{O2}$ (top) and $Cu_2O@L_1^{O2}$ (bottom) from THF, B) $Cu_2O@L_2^{O2}$ from acetone, and C) $Cu_2O@L_2^{O2}$ from methanol. Indexed against Cu_2O as vertical bars (JCPDS card no.: 00-002-1067).

To establish the stability of the 'inks' the properties of the Cu_2O NPs before and after solvent addition were tested. The Cu_2O NP phase is preserved in THF and acetone, as demonstrated in **Figure 2.23**. However, for methanol, additional reflections at low 2 theta [°] are observed, perhaps indicating the formation of a layered material.

The solubility tests indicate that the polyether ligand show significantly greater solubility to the resulting nanoparticles, which form stable colloidal solutions in both polar and non-polar solvents.

2.2.5 PRELIMINARY PROGRESS IN CATALYTIC APPLICATIONS USING CU AND Cu_2O NPS

Using abundant CO_2 as a carbon feedstock has gained significant attention over the past years.[31] However, CO_2 is very stable due to strong C=O bonds (C=O bonding energy; 127 kcal·mol^{-1}), therefore energy in the form of thermochemical, electrochemical, or photochemical, is required for its catalytic transformation.[32] Copper based materials such as metallic copper (Cu), or cuprous oxide (Cu_2O) could be inexpensive, and low toxicity catalysts for the hydrogenation of CO_2 into chemicals and fuels (see introduction, chapter 1).[1,33]

In this regard, collaborations with other research groups have been initiated to test the Cu@L_n^{O2} and Cu_2O@L_n^{O2} (n = 1, 2) nanoparticles as catalysts for the hydrogenation of CO_2. In the following section, an overview of the preliminary catalytic results are provided.

2.2.5.1 Photocatalytic testing of Cu_2O

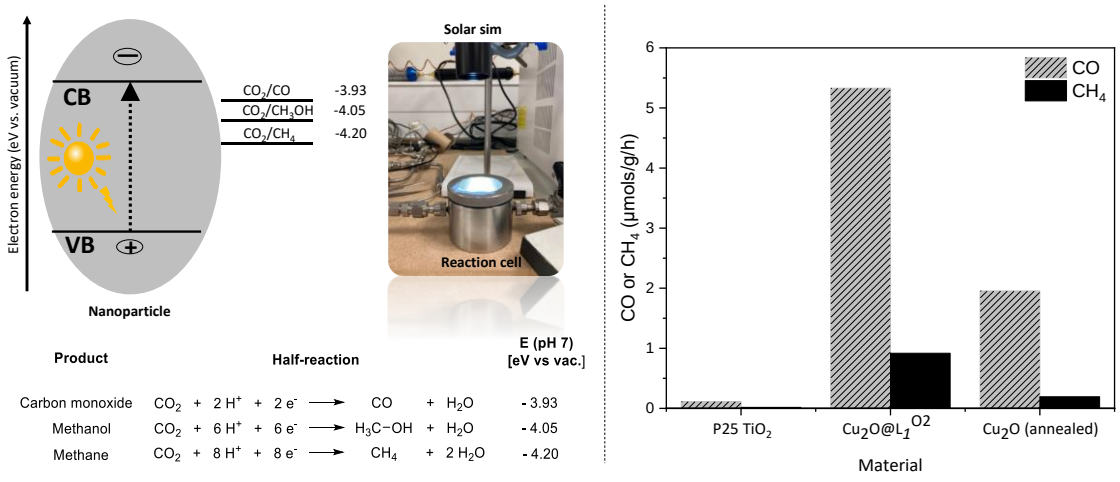

Scheme 2.4. Simplified formation of electrons (–) and holes (+) *via* photonic excitation (sun) of a nanoparticle (oval, grey). Table showing products and half-cell redox potential (E) that occurs during CO_2 reduction at pH 7. Picture of reaction cell used for photocatalytic testing under irradiation (left). Preliminary results for photocatalytic testing of Cu_2O@L_2^{O2} and Cu_2O nanoparticles in comparison to standard P25 TiO_2. Data collected by Floriana Moruzzi, Dr Ludmilla Steier Group (right).

The narrow band gap of for Cu_2O@L_n^{O2} (~2 eV, n = 1 or 2) is compatible with light harvesting across the visible spectrum (**Scheme 2.4**). Therefore, the Cu_2O nanoparticles may be photocatalysts for the hydrogenation of CO_2.

In collaboration with the research group of Dr Ludmilla Steier at the University of Oxford, a gas phase photoreactor with a reactant gas consisting of CO_2:H_2 in a 1:3 ratio was used for testing thin films of $Cu_2O@L_2^{O2}$ for photocatalytic CO_2 reduction. In the first experiment a 36 mM toluene solution of $Cu_2O@L_2^{O2}$ was drop casted onto a pre-weighted glass slide and dried in air; the process was repeated until 2 mg of dried nanoparticles were on the glass slide. The catalytic activity of the sample was tested in the gas reactor and the products formed were analysed using gas chromatography. In another test run, the deposited $Cu_2O@L_2^{O2}$ nanoparticles were annealed on the glass slide for 30 minutes at 150 ^oC prior to catalytic testing. The annealing was conducted to remove the ligands according to the TGA experiments for $Cu_2O@L_2^{O2}$.

In both cases, the Cu_2O nanoparticles were found to be photocatalytically active (Scheme 2.4, right), evidenced by negligible CO_2 reduction during dark runs (data not shown). To our surprise, there was no improvement in catalytic activity following ligand removal. In fact, the amount of CO and methane formed during CO_2 reduction was less for the ligand-free annealed sample. In comparison to the TiO_2 standard, the performance of the Cu_2O nanoparticles were significantly better in the initial result. Therefore, it is worth conducting further investigations in the future using these nanoparticles.

2.2.5.2 Cu_2O as co-catalysts for organic based photocatalysts

Single semi-conductor (p(^{t}Bu)TA-Ph) Reduction Co-catalyst

Scheme 2.5. Using Cu_2O NPs as co-catalysts in photocatalytic organic single semi-conducting polymers, such as p(^{t}Bu)TA-Ph (band gap 2.72 eV with HOMO at -5.64 eV and LUMO at -2.92 eV).

Another option is to decouple the photon absorption from the catalytic reduction. To achieve this a nanocomposite of a conjugated polymer (absorber) and Cu_2O (co-catalyst) were targeted. Dissolving

the organic single semi-conductor, p(^{t}Bu)TA-PH, in a solvent and adding a colloidal solution of $Cu_2O@L_2^{O2}$ was considered as a synthesis strategy (**Scheme 2.5**).

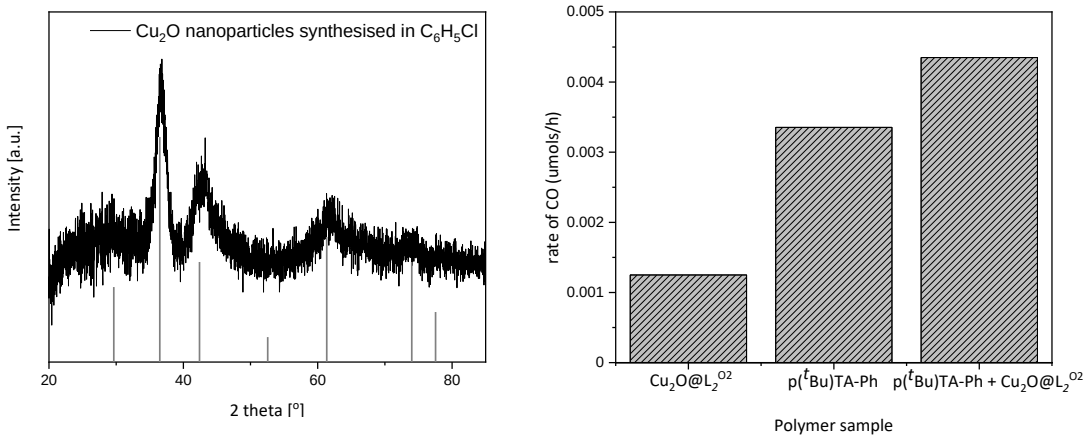

Figure 2.24. Powder X-ray diffractogram of $Cu_2O@L_2^{O2}$ NPs synthesised in chlorobenzene (left). Rate of CO in mols/h produced during the photocatalytic reduction of CO_2 with $Cu_2O@L_2^{O2}$, p(^{t}Bu)TA-Ph or p(^{t}Bu)TA-Ph + $Cu_2O@L_2^{O2}$ as catalysts. Data collected by Floriana Moruzzi, Steier Group (left).

First, a common solvent had to be found for both the polymer and the organometallic synthesis of Cu_2O nanoparticles. Chlorobenzene was identified to fulfil both requirements. $Cu_2O@L_2^{O2}$ nanoparticles were successfully synthesised in chlorobenzene with a particle size of 4 nm (**Figure 2.24**, left). Mixing of the polymer, p(^{t}Bu)TA-Ph, with 5 wt% [Cu] in form of $Cu_2O@L_2^{O2}$ yielded a dark film after drop casting the mixture onto a glass slide and drying it in air. For comparison, another two glass slides were prepared of which one contained the same amount of p(^{t}Bu)TA-Ph polymer only and the other one $Cu_2O@L_2^{O2}$ NPs. Photocatalytic testing was carried out in the gas phase reactor with a 3:1 ratio of H_2 to CO_2 gas feed and the products formed were analysed using gas chromatography.

While preliminary results showed both, $Cu_2O@L_2^{O2}$ and p(^{t}Bu)TA-Ph, are able to reduce CO_2 to CO, the nanocomposite demonstrated superior performance (**Figure 2.24**, right).

2.2.5.3 Cu_2O supported SWCNT for electrocatalytic testing

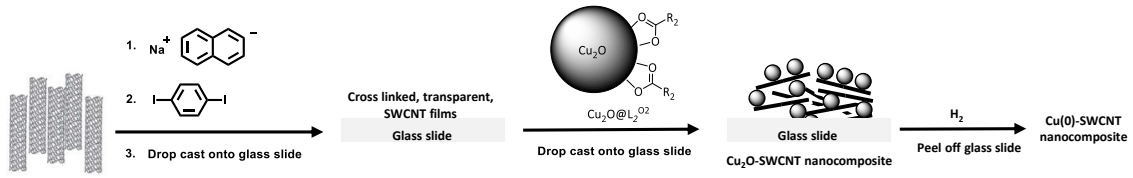

Scheme 2.6. Proposed and investigated synthesis strategy to Cu_2O-SWCNT nanocomposite.

The formation of a Cu_2O-SWCNT (single walled carbon nanotube) nanocomposite material was investigated in collaboration with Prof. Milo Shaffer's research group at Imperial College London for electrocatalysis (**Figure 2.6**). The carbon-based material might obviate deposition on electrodes and may increase conductivity and electron localisation at the catalytic sites.

The cross linked, transparent SWCNT film was prepared according to a literature protocol by David M. Stringer at Imperial College of London.[34] Drop casting of a 36 mM toluene solution of $Cu_2O@L_2^{O2}$ onto the cross linked SWCNT yielded a black film, which was peeled off the glass slide prior to further analysis.

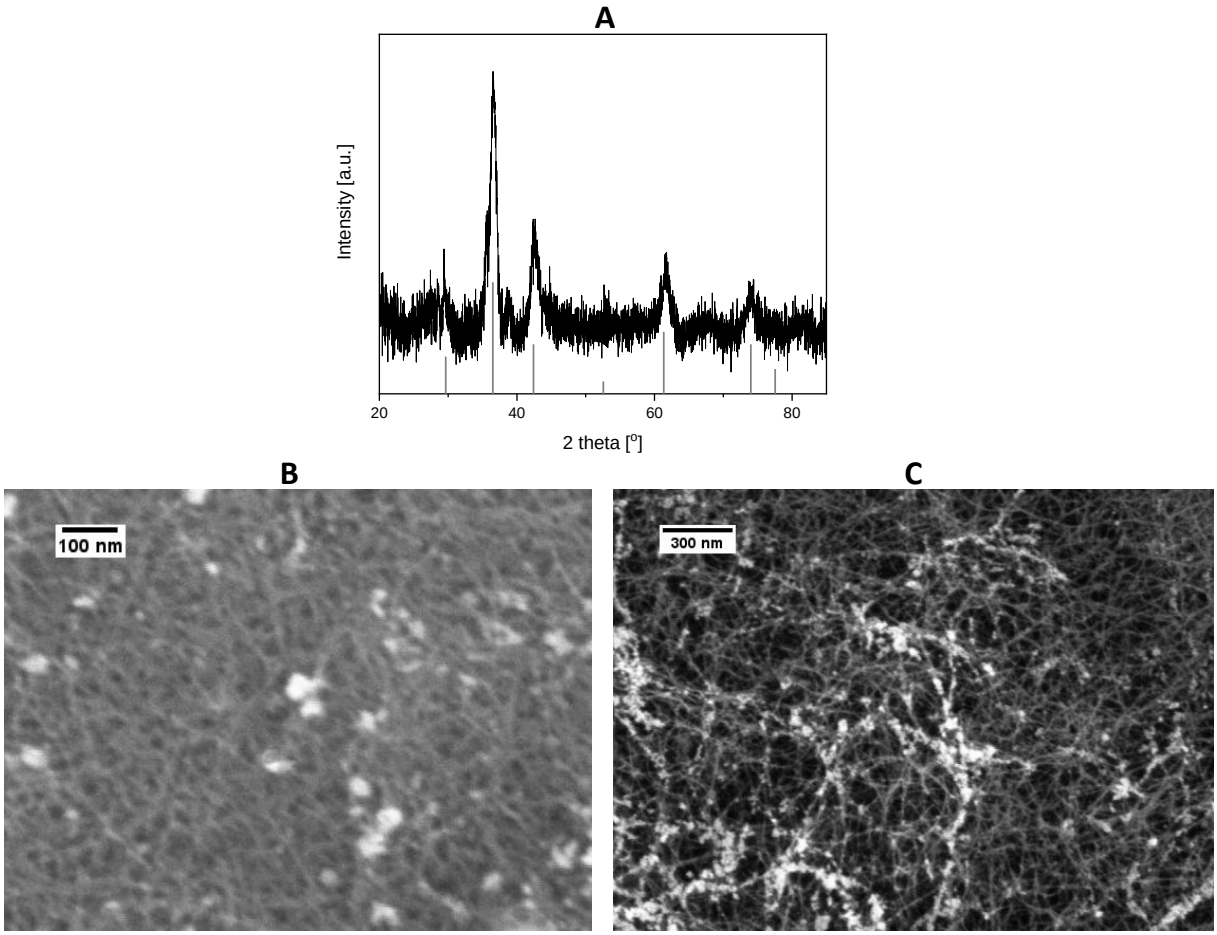

Figure 2.25. A) Powder X-ray diffractogram of a $Cu_2O@L_2^{O2}$ infused SWCNT nanocomposite. Patterns are indexed against Cu_2O as black vertical bars (JCPDS card no.: 00-002-1067). SEM pictures of: B) the surface of the SWCNT infused by the $Cu_2O@L_2^{O2}$ nanoparticles, and C) inside the SWCNT infused by the $Cu_2O@L_2^{O2}$ nanoparticles. The SEM data was collected by David M. Stringer (Imperial College London).

Characterisation of the Cu_2O-SWCNT nanocomposite by powder X-ray diffraction showed that the phase of Cu_2O was preserved under the applied conditions (**Figure 2.25**, A). However, the particle size was calculated to be 7 nm, using Scherrer equation, which is larger than the ~3 nm particles of the original ink solution, suggesting agglomeration of the nanoparticles.

SEM analysis of the surface and inside the SWCNT showed the Cu_2O nanoparticles as evenly distributed 'bright' spots within the SWCNT matrix (**Figure 2.25**, B and C) but some of the particles appear to be agglomerated to larger particles.

These initial results are promising and provide proof-of-concept over the production of Cu_2O-SWCNT nanocomposite. Electrocatalytic testing should be investigated in the future.

2.3 SUMMARY AND CONCLUSIONS

Ultra-small (~4 nm) stable colloidal Cu(0) nanoparticles were synthesised from an organometallic Cu(I) precursor, CuMes, with substochiometric amounts (0.1 equiv. with regards to [Cu]) of of various carboxylic acid and thiocarboxylic acid coordinating ligands. The ligands form colloidal solutions of Cu(0) nanoparticles that were stable in solutions for several weeks under N_2.

The nanoparticle ligand and compatibility was probed *via* a series of ligand exchange reactions. The addition of HL_1^{S2} to $Cu@L_1^{O2}$ or HL_1^{O2} to $Cu@L_1^{S2}$ resulted in similar products as determined using UV-Vis and FT-IR spectra. The data indicate that the nanoparticles were not fully ligand saturated with 0.1 equiv. ligand, allowing the coordination of further ligand onto the surface. Nonetheless, the data also indicate that Cu(0) NPs preferentially coordinate *S*-ligands.

Colloidal Cu_2O nanoparticles were prepared by exposure of $Cu@L_n^{O2}$ (n = 1 or 2 and X = O or S) to air. When oxygen-containing carboxylate ligands were deployed, a stable colloidal solution of Cu_2O was provided. However, the sulphur-containing dithiocarboxylate ligand, was not capable of stabilising colloidal Cu_2O. These findings indicate that carboxylate-containing ligands are better suited to the surface of Cu_2O nanoparticles.

An important overall conclusion is that the chemistry of the ligand should be 'matched' to the nanoparticle surface to maximise stability and access colloidal solutions.

In terms of thermal ligand removal, the polyether-containing carboxylate ligand, $[L_2^{O2}]^-$, was removed at lower temperatures than the alkyl-containing carboxylate ligand, as evidenced by an onset degradation temperature of 150 °C for $Cu_2O@L_2^{O2}$ in comparison to 220 °C for $Cu_2O@L_1^{O2}$.

Though, ligand removal may not be necessary for the photocatalytic CO_2 reduction, as the "naked" Cu_2O nanoparticles showed in preliminary results a lower catalytic activity in comparison to $Cu_2O@L_2^{O2}$.

The new Cu_2O nanoparticles, capped by a polyether-containing carboxylate ligand possess higher solubility in common organic solvents than those coordinated by an alkyl-containing carboxylate ligand. They are highly soluble in toluene, THF, acetone and methanol.

This work has initiated a long-term programme aimed to discovery of the most effective ligands. Currently, ligand selection appears to be largely empirical/trial and error based. For future investigations the goal should be to understand the parameters influencing stability.

2.4 REFERENCES

[1] M. B. Gawande, A. Goswami, F.-X. Felpin, T. Asefa, X. Huang, R. Silva, X. Zou, R. Zboril, R. S. Varma, *Chem. Rev.* **2016**, *116*, 3722-3811.

[2] M. Srivastava, J. Singh, R. K. Mishra, A. K. Ojha, Compounds, *J. Alloys Compd.* **2013**, *555*, 123-130.

[3] A. Paolella, R. Brescia, M. Prato, M. Povia, S. Marras, L. De Trizio, A. Falqui, L. Manna, C. George, *ACS Appl. Mater. Interfaces* **2013**, *5*, 2745-2751.

[4] D. Dodoo-Arhin, M. Leoni, P. Scardi, E. Garnier, A. Mittiga, *Mater. Chem. Phys.* **2010**, *122*, 602-608.

[5] X. Su, J. Chang, S. Wu, B. Tang, S. Zhang, *Nanoscale* **2016**, *8*, 6155-6161.

[6] C. Barrière, K. Piettre, V. Latour, O. Margeat, C.-O. Turrin, B. Chaudret, P. Fau, *J. Mater. Chem.* **2012**, *22*, 2279-2285.

[7] C. Barrière, G. Alcaraz, O. Margeat, P. Fau, J. B. Quoirin, C. Anceau, B. Chaudret, *J. Mater. Chem.* **2008**, *18*, 3084-3086.

[8] S. D. Pike, E. R. White, A. Regoutz, N. Sammy, D. J. Payne, C. K. Williams, M. S. P. Shaffer, *ACS Nano* **2017**, *11*, 2714-2723.

[9] S. Rej, M. Bisetto, A. Naldoni, P. Fornasiero, *J. Mater. Chem. A* **2021**, *9*, 5915-5951.

[10] R. Marschall, *Adv. Funct. Mater.* **2014**, *24*, 2421-2440.

[11] *X-Ray Data Booklet* **2009**, *Third edition*.

[12] J. C. Klein, C. P. Li, D. M. Hercules, J. F. Black, *Appl. Spectrosc.* **1984**, *38*, 729-734.

[13] S. Barman, D. Sarma, *J. Phys.: Condens. Matter* **1992**, *4*, 7607.

[14] G. Schön, R. Phenomena, *J. Electron Spectrosc. Relat. Phenom.* **1972**, *1*, 377-387.

[15] J. M. Pi, M. Stella, N. K. Fernando, A. Y. Lam, A. Regoutz, L. E. Ratcliff, *J. Phys. Chem. Lett* **2020**, *11*, 2256-2262.

[16] A. Regoutz, M. S. Wolinska, N. K. Fernando, L. E. Ratcliff, *Electron. Struct.* **2021**, *2*, 044005.

[17] P. Swift, *Surf. Interface Anal.* **1982**, *4*, 47-51.

[18] T. L. Barr, S. Seal, *J. Vac. Sci. Technol. A* **1995**, *13*, 1239-1246.

[19] D. L. Perry, J. A. Taylor, *J. Mater. Sci. Lett.* **1986**, *5*, 384-386.

[20] M. Justi, M. P. de Freitas, J. M. Silla, C. A. Nunes, C. A. Silva, *J. Mol. Struct.* **2021**, *1237*, 130405.

[21] A. Miyasuta, A. Yamamoto, *J. Organomet. Chem.* **1976**, *113*, 187-199.

[22] P. Kanninen, C. Johans, J. Merta, K. Kontturi, *J. Colloid Interface Sci.* **2008**, *318*, 88-95.

[23] C. Rohner, A. Pekkari, H. Härelind, K. Moth-Poulsen, *Langmuir* **2017**, *33*, 13272-13276.

[24] S. Poulston, P. Parlett, P. Stone, M. Bowker, *Surf. Interface Anal.* **1996**, *24*, 811-820.

[25] P. E. Larson, *J. Electron Spectrosc. Relat. Phenom.* **1974**, *4*, 213-218.

[26] L. Lu, S. Zou, B. Fang, *ACS Catal.* **2021**, *11*, 6020-6058.

[27] K. P. Kepp, *Inorg. Chem.* **2016**, *55*, 9461-9470.

[28] R. G. Pearson, *J. Chem. Educ.* **1968**, *45*, 643.

[29] M. Sinel'nikova, E. Shved, V. Usachev, N. Oleinik, *Theor. Exp. Chem.* **2010**, *46*, 168-175.

[30] *SciFinder, Calculated using Advanced Chemistry Development (ACD/Labs) Software V11.02 (© 1994-2022 ACD/Labs)*.

[31] A. Dibenedetto, A. Angelini, P. Stufano, *J. Chem. Technol. Biotechnol.* **2014**, *89*, 334-353.

[32] S. W. Benson, *J. Chem. Educ.* **1965**, *42*, 502.

[33] Y.-X. Yu, L. Pan, M.-K. Son, M. T. Mayer, W.-D. Zhang, A. Hagfeldt, J. Luo, M. Grätzel, *ACS Energy Lett.* **2018**, *3*, 760-766.

[34] M. De Marco, F. Markoulidis, R. Menzel, S. M. Bawaked, M. Mokhtar, S. A. Al-Thabaiti, S. N. Basahel, M. S. P. Shaffer, *J. Mater. Chem. A* **2016**, *4*, 5385-5389.

Chapter 3:

Hydrotalcite-like Materials from Organometallics

3 HYDROTALCITE-LIKE MATERIALS FROM ORGANOMETALLICS

3.1 BACKGROUND AND SCOPE

With increasing interest in 2D nanoplatelets, our group has designed a new bottom-up synthetic approach to make exfoliated nano-sheets of LZH, incorporating a range of carboxylates (L_n^{O2}) bound to the surface (**Scheme 3.1**).[1,2]

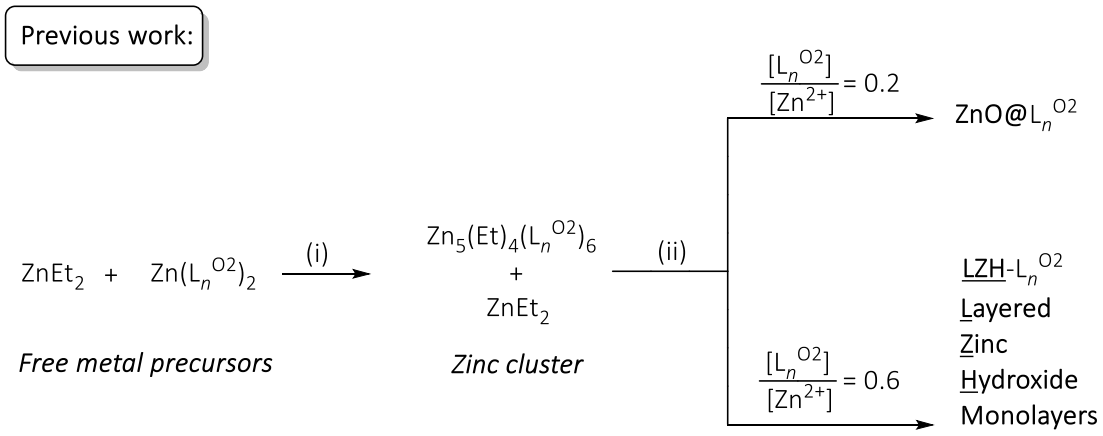

Scheme 3.1. Synthesis of ZnO@L_n^{O2} and LZH@L_n^{O2} nanoplatelets *via* an organometallic approach; (i) Toluene, 25 °C, 16 h, (ii) H_2O, 25 °C, 3 h.[1,2]

The inspiration for this synthesis is derived from the discovery that the hydrolysis of a mixture of diethyl zinc and a non-hydrolysable zinc carboxylate afforded colloidal dispersions of carboxylate capped ZnO nanoparticles. At certain zinc:ligand ratios another phase was identified which was subsequently shown to be the LZH. Although the detailed mechanism for the formation of these nanomaterials isn't fully understood, it is proposed that the hydrolysable Zn-alkyl groups, present on both dialkyl zinc and heteroleptic zinc complexes comprising ethyl and carboxylate ligands, react with water, forming Zn-OH species. A series of condensation and rearrangement reactions must occur to finally deliver crystalline ZnO nanoparticles coordinated by carboxylate ligands. The layered hydroxide species were considered to be intermediates of the nucleation and growth process of ZnO. Initial results showed that the quantity of the LZH by-product increased with increased quantities of zinc carboxylate

(or carboxylic acid precursor) added to the reaction. Therefore, a sufficient quantity of carboxylate ligands was expected to allow for the exclusive synthesis of layered zinc hydroxides.[1-4]

The synthesis of LZH materials entailed the controlled hydrolysis of diethylzinc with bis(carboxylate)zinc in toluene ([Zn] = 0.15 M). The carboxylate loading is defined as the ratio of the total amount of carboxylate [COOR] relative to the total amount of zinc [Zn]. From the chemical formula for LZH, $[Zn_5(OH)_8(A)_2 \cdot nH_2O]$, a molar ratio of [COOR]/[Zn] = 0.4 would be expected to be effective for forming pure LZH. However, ZnO Wurzite nanoparticles were detected in the powder XRD analysis as a side product at a carboxylate loading ratio lower than 0.6. IR spectroscopy, TGA and elemental analysis suggested that the excess carboxylate ligands were present as bis(carboxylate)zinc located between the nanoplatelets layers but that the excess was required to suppress over-hydrolysis of the LZH to the oxide. The LZH synthesised at the optimal ratio of [COOR]/[Zn] = 0.6 gave rise to a phase which was mostly LZH with ~6.4 wt.% ZnO, as determined by UV-Vis spectroscopy. In comparison to other literature routes to LZH, the amount of ZnO impurity is significantly smaller.[1,3]

In addition, the controlled hydrolysis of organozinc species directly affords exfoliated solutions of layered zinc hydroxide monolayers. In contrast, other syntheses yield aggregates which need to be subjected to physically aggressive exfoliation treatments. The LZH exfoliated nanosheets were characterized by TEM and AFM analysis both of which confirmed the existence of exfoliated monolayers (~3.6 nm x ~24 nm for LZH-L_3^{O2} with $L_3^{O2} = C_{18}H_{33}O_2$ = oleate).[1,3]

In-situ ^{1}H NMR spectroscopy of LZH-L_3^{O2} was applied to study the formation of LZH monolayers. The data suggested the hydrolysis of Zn-C bonds from $ZnEt_2$ first, followed by the hydrolysis of Zn-ethyl species in the pentanuclear zinc cluster $[Zn_5(Et)_4(L_3^{O2})_6]$ (Scheme 3.1). Finally, the formation of LZH is stabilised by the carboxylate ligands.[1,3]

In general, 2D layered zinc hydroxide nanoplatelets of high purity were synthesised directly *via* a simple hydrolysis of organo-zinc precursors, at room temperature. As the synthesis is carried out under a nitrogen atmosphere the formation of strongly coordinating carbonate contaminations

between the layers from reactions with atmospheric CO_2 is prevented, therefore exfoliation into nanosheets is facilitated. Moreover, the organometallic route was later extended to include carboxylic acids bearing ethylene glycol alkyl ether substituents, an alkyl substituent featuring a terminal alkene or a fluorescent anthracene substituent.[2] The metal cation(s) compositional tunability of layered materials is known but the generality of this unique organometallic approach has yet to be investigated and was therefore subject of this work.

The focus of this chapter is to investigate the synthesis of a metal doped layered zinc hydroxide. Specifically, a layered Cu/Zn/Al-based catalyst for methanol generation from CO_2, was proposed. Inspired by the commercially applied catalyst ($Cu/ZnO/Al_2O_3$), we targeted the synthesis of a CuZnAl LDH. The objective was to try to expand the synthetic method used to make LZH so as to generate the doped material and to use it to make small and stable colloidal metal oxide nanoparticles. It was hypothesized that this method might result in high Cu surface area; which is commonly attributed to high activity in CO_2 hydrogenation catalysis.

The controlled hydrolysis of $ZnEt_2$ in the presence of a carboxylic acid at a loading of [COOR]/[Zn] = 0.6 resulted in the formation of exfoliated LZH of high purity (**Scheme 3.1**).[1] Building on this method, the organometallic route was targeted with the addition of a suitable aluminium and copper organometallic reagents was investigated as a route to provide CuZnAl htl-like monolayers. Triethylaluminium ($AlEt_3$) and mesitylcopper (CuMes) were chosen as suitable precursors because they are commercially available and they generate volatile, yet inert hydrocarbons, upon hydrolysis that can be easily removed, and they have been used previously to make aluminium and/or copper doped colloidal ZnO nanoparticles, following a related organometallic hydrolysis approach.[1]

One aspect worth highlighting is that the introduction of Cu(I) doping has not been reported in CuZnAl LDH materials. This is most likely because conventional co-precipitation strategies are conducted under air, thus restricting results to Cu(II) species. However, the use of Schlenk techniques may allow for investigation of the potential to make LDH materials containing Cu(I).

Generally, CuZnAl hydrotalcite-like (htl-like) catalyst precursors for CO_2 hydrogenation are worth exploration since it is generally accepted that the choice of catalyst precursor and its pre-treatment strongly influence the catalysis. Several authors have reported that both Cu(I) and Cu(0) centres are required for successful hydrogenation of CO_2 to methanol.[5-8] Conventional H_2 activation of Cu(II)-based precursors affords mixtures of a Cu(I) and Cu(0), with Cu(I) as a minor component. However, Gao *et* al. showed that an increased ratio of active Cu(I)/Cu(0) is advantageous for catalytic selectivity.[5] Therefore, having Cu(I) as the only active species within the catalyst is an important target.

Lastly, the organometallic approach could be useful from a materials perspective because Cu(II) doping usually destabilises the layered zinc material due to its Jahn-Teller distortion. This is not expected for Cu(I) as it is a d^{10} metal. Moreover, Cu(I) and Zn(II) are isovalent, therefore phase-pure copper-rich monolayers of CuZnAl LDH materials might be feasible if the synthesis can be appropriately conducted.

This chapter aims to expand the organometallic synthetic approach. The first target would be AlZn LDH, followed by the incorporation of Cu(m) (m = I or II) as a third component in the metal layers to yield Cu^{m}ZnAl htl-like structures.

3.2 Results and Discussion

3.2.1 Synthesise of CuZnAl LDH Materials from organometallic Precursors

Expanding the organometallic synthetic protocol of LZH to LDH materials was investigated stepwise. The synthesis of ZnAl LDH was targeted first, followed by expanding the protocol to CuZnAl htl-like structures containing Cu(m) (with m = I or II).

3.2.1.1 Attempted Synthesis of ZnAl LDH Materials

ZnAl LDH with Zn:Al ratio of 3:1 are well characterised and studied in literature. The reported organometallic approach to LZHs was modified accordingly by exchanging 25 % of the zinc precursor, $ZnEt_2$, for $AlEt_3$.

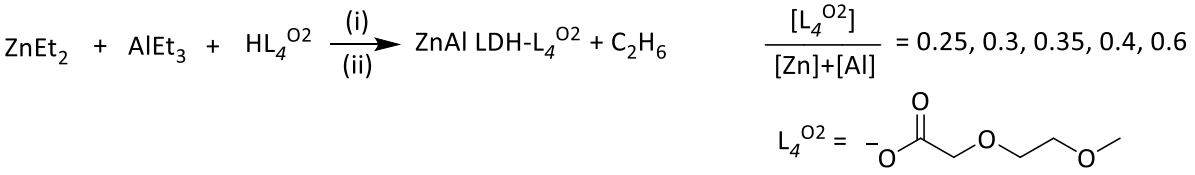

Scheme 3.2. Reaction conditions tested for the synthesis of 3:1 ZnAl LDHs intercalated by 2-(2-methoxyethoxy)acetate ($[L_4^{O2}]^-$). (i) Toluene, 25 °C, 16 h, (ii) H_2O, 25 °C, 3 h.

$ZnEt_2$ and $AlEt_3$ were mixed with 2-(2-methoxyethoxy)acetic acid (HL_4^{O2}) in toluene at 25 °C. Different ligand loadings of $[L_4^{O2}]/([Zn]+[Al])$ = 0.25, 0.30, 0.35, 0.40 and 0.60 were probed to find the optimised carboxylate loading necessary for the formation of LDH. HPLC-grade water was added directly to the reaction mixture after 16 h, and all volatiles were removed after 3 h, yielding colourless powders for all loadings. The samples were characterised using FT-IR spectroscopy and powder X-ray diffraction (XRD).

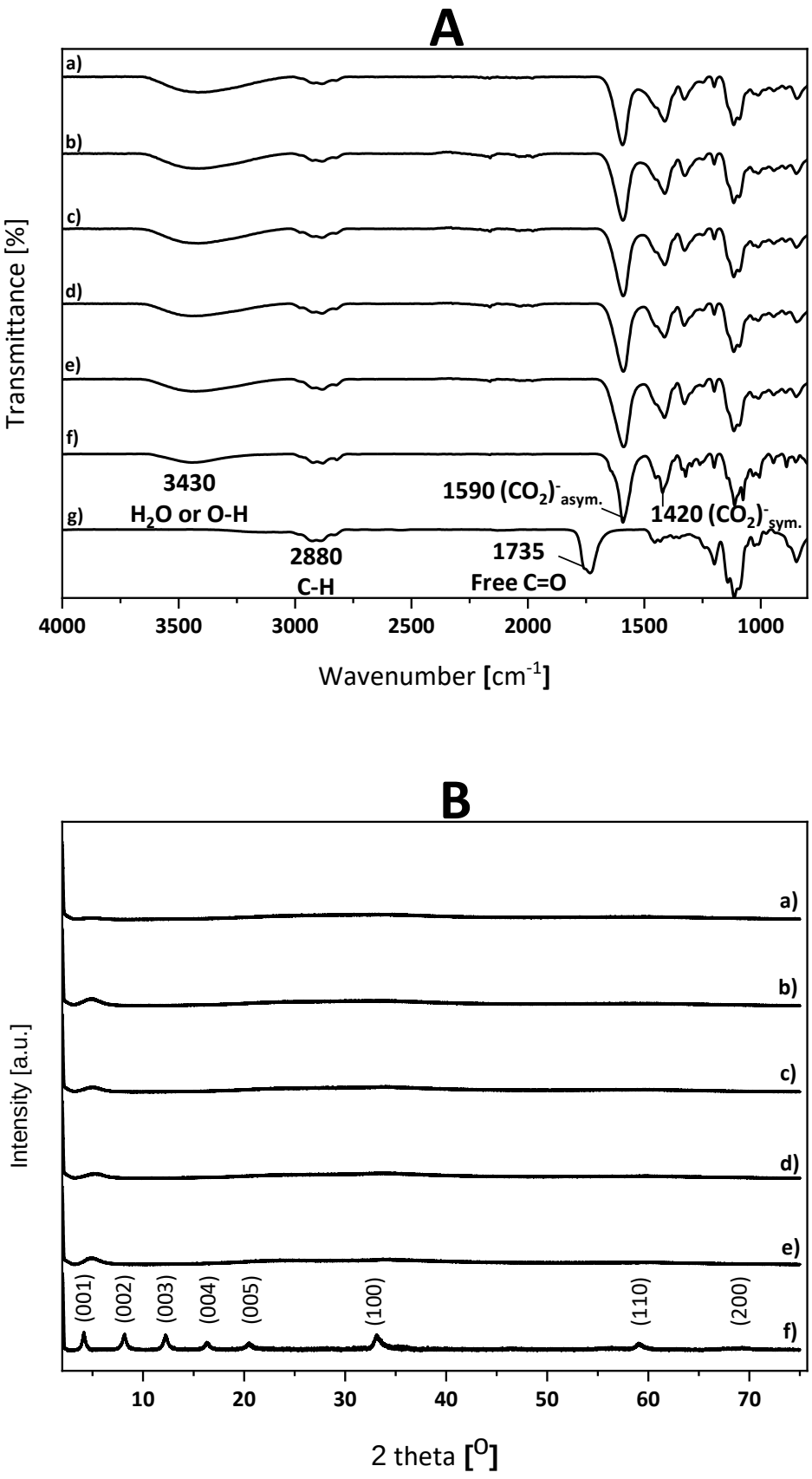

Figure 3.1. FT-IR spectra (A) and powder X-ray diffraction patterns (B) of isolated powders from attempts to synthesise ZnAl LDH-L_4^{O2}_X with a ligand loading X [L_4^{O2}]/([Zn]+[Al]) of a) 0.25, b) 0.3, c) 0.35, d) 0.4, e) 0.6, f) reference LZH-L_4^{O2} synthesised according to Ref.[2] and g) 2-(2-methoxyethoxy)acetic acid (HL_4^{O2}).

The FT-IR spectra with different ligand loadings are similar and consistent with that observed for LZH-L_4^{O2}. The broad stretch at 3430 cm^{-1} is assigned to either the hydroxyl groups (–OH) in the layered materials, water intercalated between the metal layers or coordinated water on the sample's surface. The stretch at 2880 cm^{-1} is assigned to the methylene groups (–CH_2–) of the ether chain. The absence of a stretching band at 1735 cm^{-1} for free carboxylic acid, and the presence of characteristic asymmetric and symmetric stretches for the carboxylate groups at 1590 cm^{-1} and 1420 cm^{-1}, respectively, indicates coordination of HL_4^{O2} as carboxylate $[L_4^{O2}]^-$ onto the metals (**Figure 3.1**).

However, analysis by powder X-ray diffraction did not confirm the successful formation of ZnAl LDH-L_4^{O2} as no sharp reflections at low 2θ, indicative for layered materials, were detected. Also, pXRD did not provide any evidence that LZH-L_4^{O2} had formed. All patterns showed a single broad diffraction peak spanning from ~3 to 6˚, along with the minor broad reflections at higher 2θ. This may either be due to very small layered particles causing very broad reflections in the diffractogram, or that the isolated materials are either amorphous themselves or contain majorly amorphous phases.

Thermal or solvothermal treatments are often deployed to grow nanomaterials in order to convert an amorphous slurry into individual crystalline particles.[9] Since the FT-IR spectra showed promising stretches associated with the carboxylate ligands, several ripening conditions were applied to the crude powder synthesised with a ligand loading of 0.6 (ZnAl LDH-L_4^{O2}_0.6).

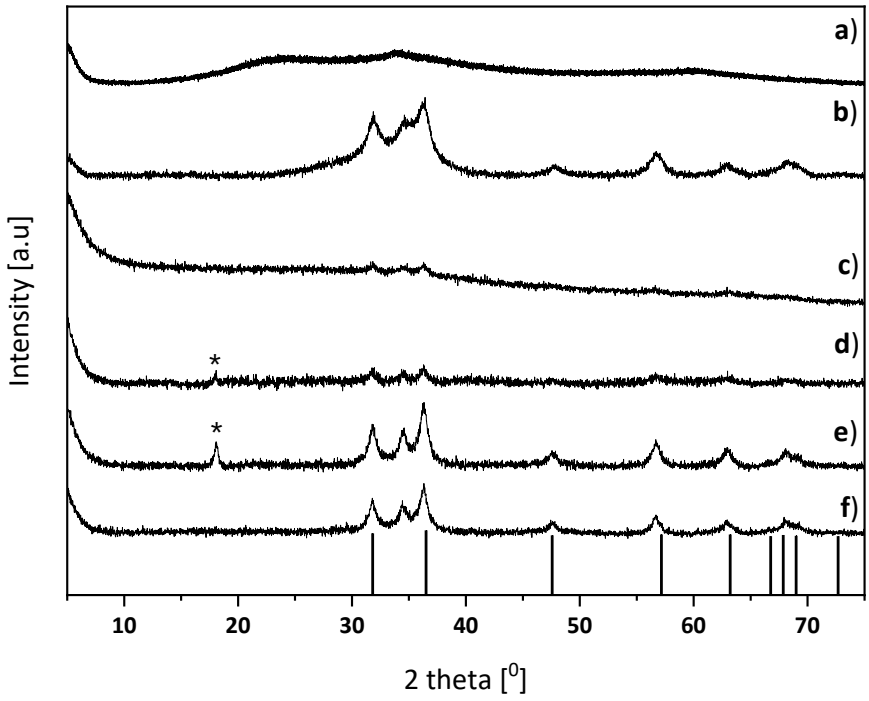

Figure 3.2. Powder X-ray diffraction pattern for ZnAl LDH-L_4^{O2}_0.6 a) 1 day after synthesis, b) after thermal ripening at 500 °C for 1 h, c) after solvothermal treatment in an autoclave with ethanol at 100 °C for 23 h, d) solvothermal treatment in toluene at 33 °C, e) at 73 °C, and f) at 93 °C. Reference bars: ZnO (JCPDS card no.: 00-001-1136). Reflections marked with '*' are not defined impurities.

Ripening the powder for 1 hour at 500 °C yielded ZnO nanoparticles only (**Figure 3.2**, b). Next, ZnAl LDH-L_4^{O2}_0.6 was dispersed in ethanol (0.5 mg/mL) *via* vigorous stirring at room temperature for 23 h. The suspension was then placed in an autoclave for solvothermal treatment at 100 ˚C for 24 h. The clear supernatant in the autoclave was decanted and the white precipitate was re-suspended in fresh ethanol, followed by centrifugation. The isolated white precipitate was dried under reduced pressure and powder X-ray diffraction analysis showed that ZnO had been synthesised exclusively (**Figure 3.2**, c). Since LZH-L_4^{O2} converts to ZnO at temperatures >40 °C, it seemed reasonable to test ripening under lower temperature conditions as layered double hydroxides might only be accessed as the kinetic products as well.[2] Therefore, the sample of ZnAl LDH-L_4^{O2}_0.6 was suspended in toluene (4.3 g/mL) and heated to 33 ˚C, 73 ˚C or 93 ˚C for 21 h. After the samples were dried under reduced pressure, powder X-ray diffraction analysis was performed, which revealed the exclusive formation of ZnO (**Figure 3.2**, d,e,f). This result was unexpected given that the reaction mixture for the synthesis of

LDH contained $AlEt_3$, but can only mean that amorphous Al-containing species (probably Al_2O_3), formed in separate phases to ZnO.

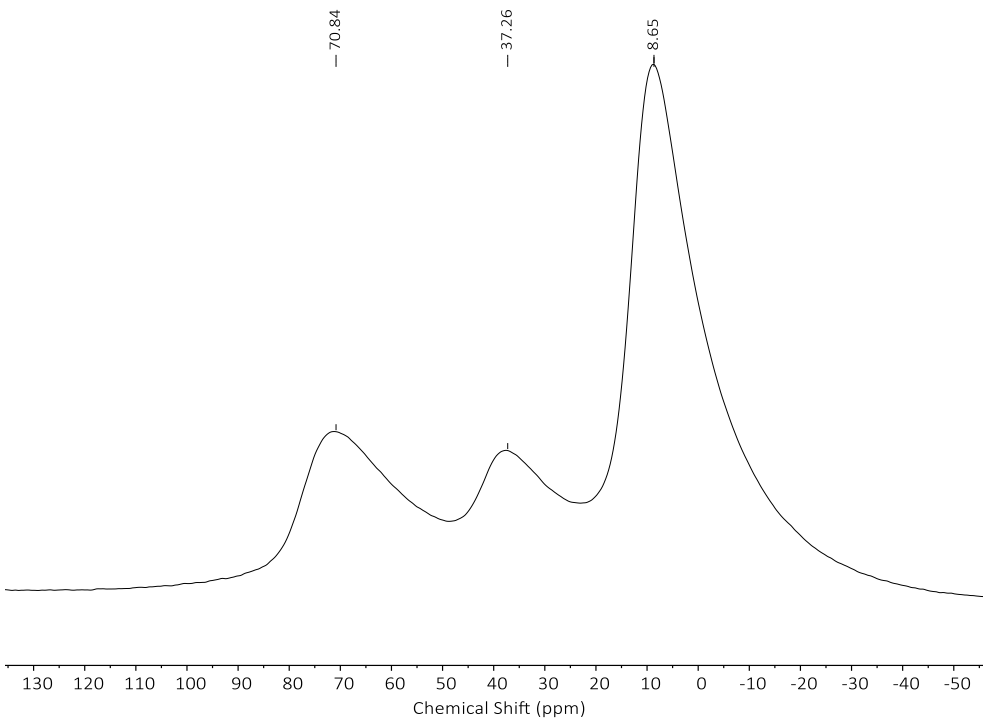

Figure 3.3. ^{27}Al-MAS-NMR spectrum of a sample ZnAl LDH-L_4^{O2}_0.6; this experiment was performed by Dr. Nick Rees.

Analysing the ZnAl LDH-L_4^{O2}_0.6 by ^{27}Al solid-state MAS NMR spectroscopy (spectra recorded by Dr. Nick Rees) verified this hypothesis. The recorded spectra (**Figure 3.3**) shows three resonances with chemical shifts of 8.65, 37.26 and 70.84 ppm, which were assigned to hexa-coordinated Al^{VI} ($\delta\,^{27}_{Al}$ = 8.65 ppm), penta-coordinated Al^{V} ($\delta\,^{27}_{Al}$ = 37.26 ppm), and tetra-coordinated Al^{IV} ($\delta\,^{27}_{Al}$ = 70.84 ppm) sites by comparison with literature data for Al_2O_3.[10-12]

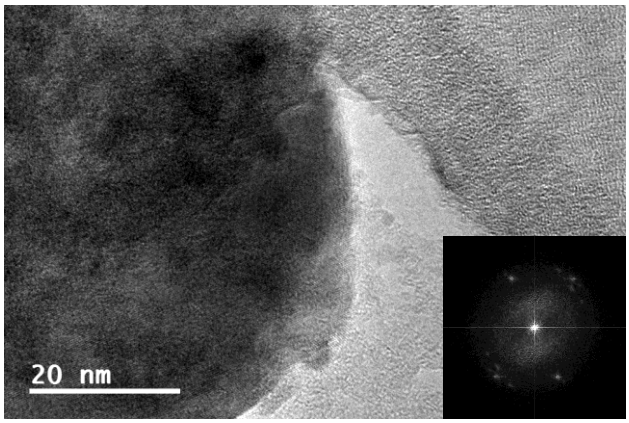

Figure 3.4. SEM image of ZnAl LDH-L_4^{O2} showing the amorphous and crystalline morphology of the sample; inset = the FFT (fast fourier transform) pattern of the image.

Further evidence for the formation of an amorphous Al species was provided by scanning electron microscopy (SEM), where a mixture of amorphous and crystalline phases were observed (**Figure 3.4**).

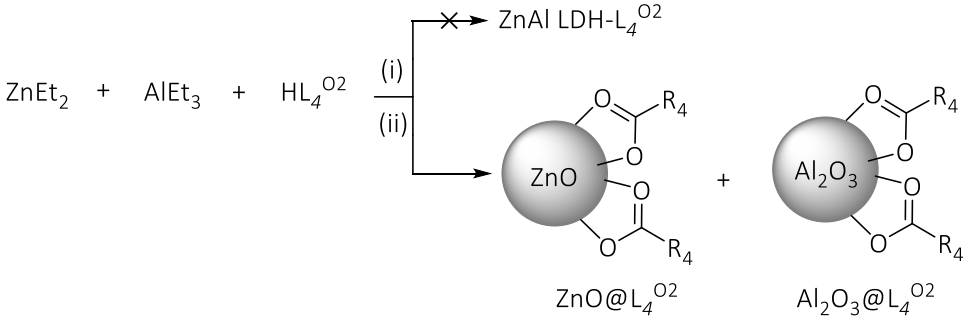

Figure 3.5. The reaction mixture of $ZnEt_2$, $AlEt_3$ and HL_4^{O2} were found to form a mixture of very small crystalline particles of ZnO@L_4^{O2} NPs alongside amorphous Al_2O_3@L_4^{O2}. The synthesis of ZnAl LDH-L_4^{O2} was not achieved. (i) Toluene, 25 °C, 16 h, (ii) H_2O, 25 °C, 3 h. HL_4^{O2} = 2-(2-methoxyethoxy)acetic acid and L_4^{O2} = 2-(2-methoxyethoxy)acetate.

The combined data indicate that the organometallic hydrolysis yields small ZnO@L_4^{O2} nanoparticles and amorphous Al_2O_3@L_4^{O2} when a mixture of $ZnEt_2$, $AlEt_3$ and HL_4^{O2} is hydrolysed under an inert atmosphere. It was hypothesised that the desired layered double hydroxides might have been formed as a pre-phase of the oxide nanoparticles, it's just that the two separate phases are more stable than LDH under the applied reaction conditions (**Figure 3.5**).

3.2.1.2 Attempted Synthesis of Cu(I) doped Layered Zinc Hydroxides

As outlined above, the organometallic route to ZnAl LDH materials was not successful. Consequently, the stepwise doping of ZnAl LDH materials with copper was also unfeasible. To tackle this problem, copper doped LZHs were targeted as precursors to CO_2 reduction catalysts.

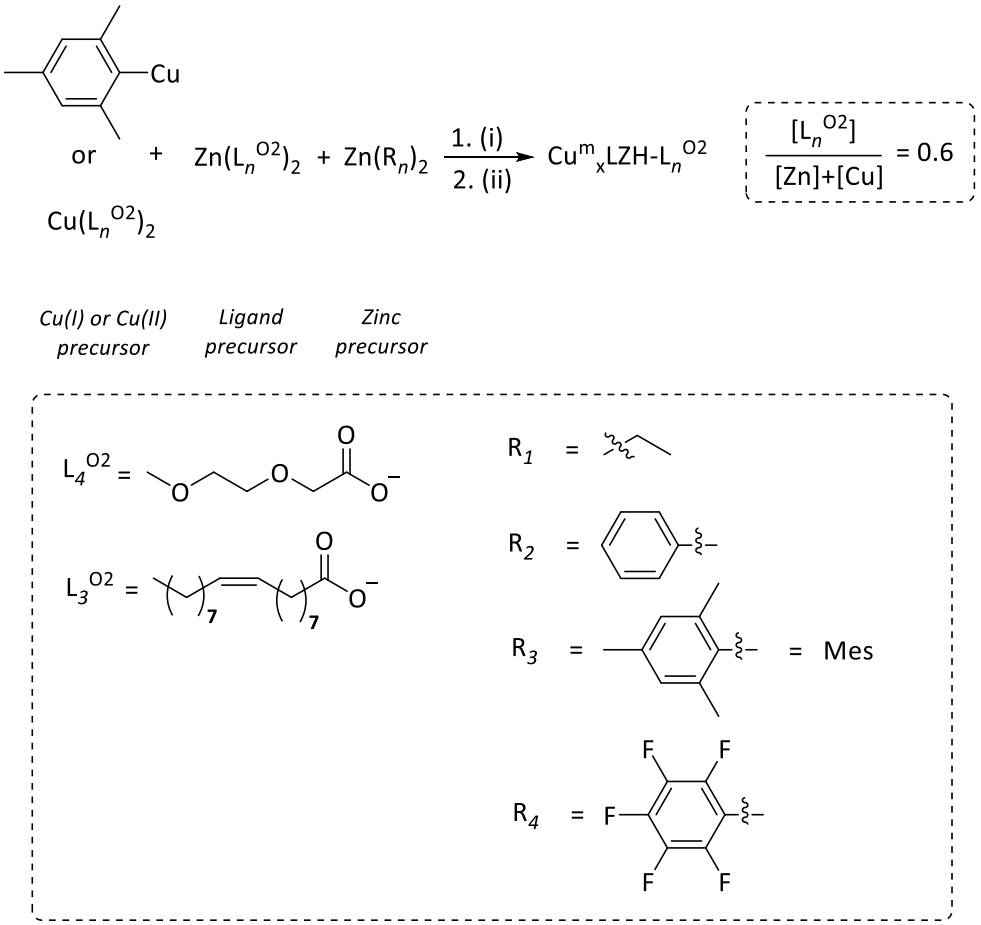

Scheme 3.3. Overview of the synthetic routes to Cu(I) or Cu(II) doped LZHs (Cu^m_xLZH-R_n with m = I or II). (i) Toluene, room temperature, overnight (ii) H_2O, room temperature, overnight.

The proposed routes involve substituting x mol% of $ZnEt_2$ for a Cu(I) precursor, or substituting x mol% of the zinc precursor, Zn(L$_n^{O2}$)$_2$, for a Cu(II) carboxylate precursor (**Scheme 3.3**).

3.2.1.2.1. Zn and Cu Catalyst Precursor Syntheses

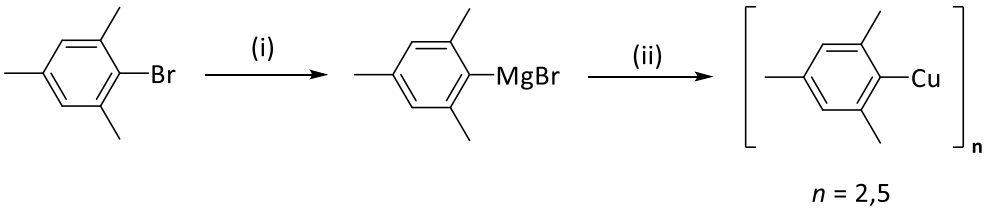

Scheme 3.4. Synthesis of CuMes from mesitylbromide. (i) Mg, Tetrahydrofuran, room temperature, 4 h; (ii) CuCl, Tetrahydrofuran, –20 °C – room temperature. Modified from Ref.[13]

Mesitylcopper (CuMes) was selected as a suitable Cu(I) precursor because an inert yet volatile byproduct, mesitylene, is generated upon hydrolysis, which can be removed under reduced pressure. It was synthesised from CuCl and mesitylmagnesium bromide according to the literature procedure, and was isolated as orange crystals in 57% yield after recrystallisation from toluene at –35 °C.[13] The ^{1}H NMR spectrum of CuMes showed the expected mixture of dimeric and pentameric species (**Figure 3.10**, top).

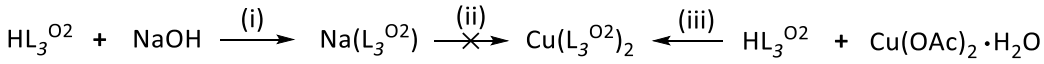

Scheme 3.5. Synthesis of bis(oleate)copper. (i) Ethanol, 50 °C; (ii) $CuCl_2$, H_2O; (iii) Toluene, 120 °C, 5 h. HL_3^{O2} = oleic acid and L_3^{O2} = oleate.

Bis(oleate)copper, ($Cu(L_3^{O2})_2$), was selected as a Cu(II) precursor due to its high solubility and the presence of oleate ligands which had previously proved effective in LZH preparations. Elemental analysis showed that the reaction between $Na(L_3^{O2})$ and $CuCl_2$ was not successful. (**Scheme 3.5**). However, the reaction between cupric acetate and HL_3^{O2} allowed the isolation of a turquoise gummy solid which was verified by elemental analysis to be $Cu(L_3^{O2})_2$, and thus subsequently used as the Cu(II) precursor (**Scheme 3.5**). NMR spectroscopy was unsuitable due to the paramagnetism of cupric acetate.

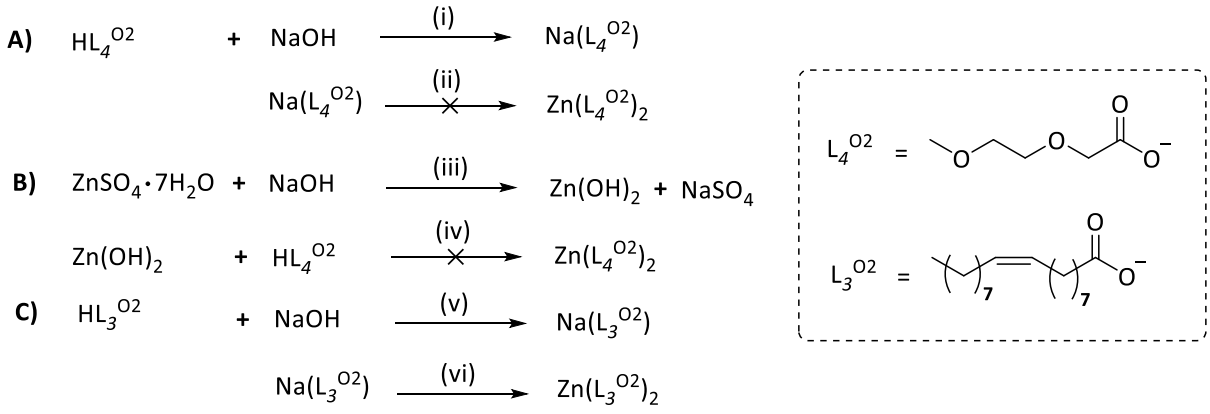

Scheme 3.6. Syntheses of zinc carboxylates. A) First attempt to synthesise bis(2-(2-methoxyethoxy)acetyl)zinc ($Zn(L_4^{O2})_2$), following a modified literature procedure to bis(oleate)zinc[14] B) Second attempt to synthesise $Zn(L_4^{O2})_2$, following a modified literature protocol for preparing bis(hexanoate)zinc[15] C) Synthesis of bis(oleate)zinc (($Zn(L_3^{O2})_2$) according to Ref.[14] . i) 1 h, 60 °C, Ethanol, ii) $ZnCl_2$ in H_2O, and B iii) H_2O, iv) *n*-Octane or Toluene, reflux, 2 h, v) ethanol, 50 °C, vi) $ZnCl_2$, H_2O HL_3^{O2} = oleic acid; HL_4^{O2} = bis(2-(2-methoxyethoxy)acetic acid.

Bis(2-(2-methoxyethoxy)acetyl)zinc, $Zn(L_4^{O2})_2$, was the target source of Zn(II) to ensure the products would be soluble in polar solvents. However, its synthesis from 2-(2-methoxyethoxy)acetic acid, HL_4^{O2}, in the presence of NaOH and $ZnCl_2$ in ethanol proved difficult (**Scheme 3.6**, A). The modified procedure requires water during the workup to extract the desired product from NaCl, but the polar nature of ether linkages in $Zn(L_4^{O2})_2$ did not allow its isolation by precipitation from ethanol with water. As a result, the crude mixture was dried and extracted with dichloromethane. After the dichloromethane solution was filtered and dried, a colorless crystalline powder was obtained.

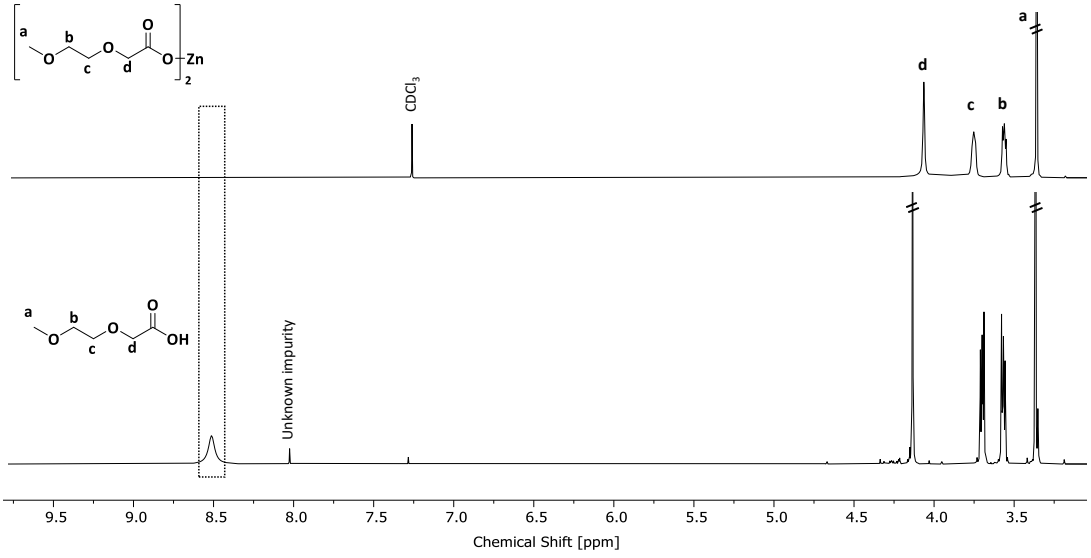

Figure 3.6. ^1H NMR spectrum of (2-(2-methoxyethoxy)acetic acid, HL_4^{O2}, in $CDCl_3$ (bottom) and bis(2-(2-methoxyethoxy)acetyl)zinc, $Zn(L_4^{O2})_2$, from dichloromethane extraction (top).

Comparison of the ^{1}H NMR spectra of the product and free carboxylic acid suggested the formation of the target product because the broad resonance representing the carboxylic acid moiety at 8.5 ppm was no longer present (**Figure 3.6**). Elemental analysis implied the same, given the C:H ratio was in the expected range (Elem. Anal. $C_{10}H_{18}O_8Zn$: C, 36.22; H, 5.47; found C, 29.00; H, 4.59). However, the low amount of carbon suggests that there is still some NaCl present.

In consequence, the synthesis of $Zn(L_4^{O2})_2$ from freshly prepared $Zn(OH)_2$ and HL_4^{O2} was investigated as an alternative route (**Scheme 3.6**, B). However, water, which was generated as a byproduct during the reaction, could not be removed following drying under reduced pressure, washing, recrystallization of the isolated product or lyophilisation. Further, changing the reaction solvent from *n*-octane to toluene was explored, since it is known to form an azeotrope with water. However, this did not facilitate the isolation of water-free $Zn(L_4^{O2})_2$.

Based on the unsuccessful attempts outlined above, bis(oleate)zinc ($Zn(L_3^{O2})_2$) was targeted as the zinc precursor. It's synthesis from freshly prepared sodium oleate, ($Na(L_3^{O2})$, and $ZnCl_2$ has previously been reported.[14]

Diethylzinc ($ZnEt_2$) has been used in previous studies as the $Zn(R_n)_2$ source, however, a 1:1 mixture of CuMes and $ZnEt_2$ in a NMR tube was unstable. A black precipitate was obtained after 1.5 h. It is proposed that diethylzinc reacts with CuMes to produce Cu(0) species, likely *via* initial mesityl/ethyl ligand scrambling, followed by β-hydride elimination. Considering the proposed decomposition mechanism, it was proposed that diphenylzinc ($ZnPh_2$) might be a more suitable zinc precursor. It is commercially available and it generates benzene as a volatile and inert byproduct that can be easily removed from the reaction mixture. However, CuMes proved to be unstable in the presence of $ZnPh_2$, as verified by ^{1}H NMR spectroscopy. An exchange of the mesityl ligand on CuMes, with a phenyl ligand on $ZnPh_2$ may form unstable CuPh. Reduction of Cu(I) to Cu(0) may be initiated by an ortho-hydride elimination.

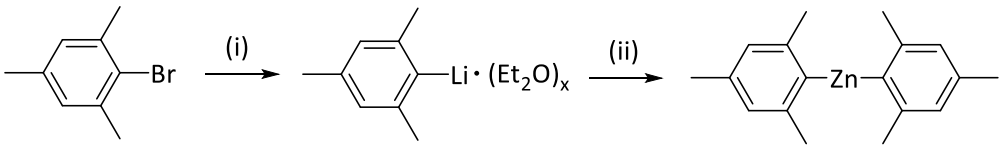

Scheme 3.7. Two step synthesis of $ZnMes_2$. (i) Adopted from Ref.[16]; *n*-BuLi, room temperature, Diethylether (ii) Modified from Ref.[17]; $ZnBr_2$, room temperature, Tetrahydrofuran.

Next, di(mesityl)zinc was targeted *via* reaction of mesityllithium with $ZnBr_2$ at room temperature (Scheme 3.7). Mesityllithium was isolated as a white powder by lithiation of mesitylbromide with *n*-BuLi at room temperature, as previously described in the literature.[16] The reaction between mesityllithium and $ZnBr_2$ at room temperature in THF-d_8 was analysed by ^1H and ^{13}C NMR spectroscopy. Immediately after the reaction was commenced a single set of new resonances were observed, indicating quantitative formation of the desired product. Furthermore, the ^1H NMR spectrum of synthesised $ZnMes_2$ in C_6D_6 was in good agreement with that reported in the literature.[16]

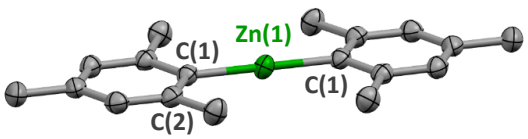

Bond	Bond Length [Å]	Angle [°]
Zn(1)-C(1)	1.9405(17)	-
C(1)-Zn(1)-C(1)	-	180
Zn(1)-C(1)-C(2)	-	120.63(12)

Figure 3.7. X-ray crystal structure of $ZnMes_2$ (Structure measured and analysed by Dr. Andreas Phanopoulos). In line with associated bond lengths and angles reported in the literature.[18]

Colourless, needle-like crystals of X-ray quality were obtained from a saturated toluene solution at –25 ˚C over three days. Single crystal X-ray diffraction (SCXRD) data confirmed the successful formation of $ZnMes_2$.

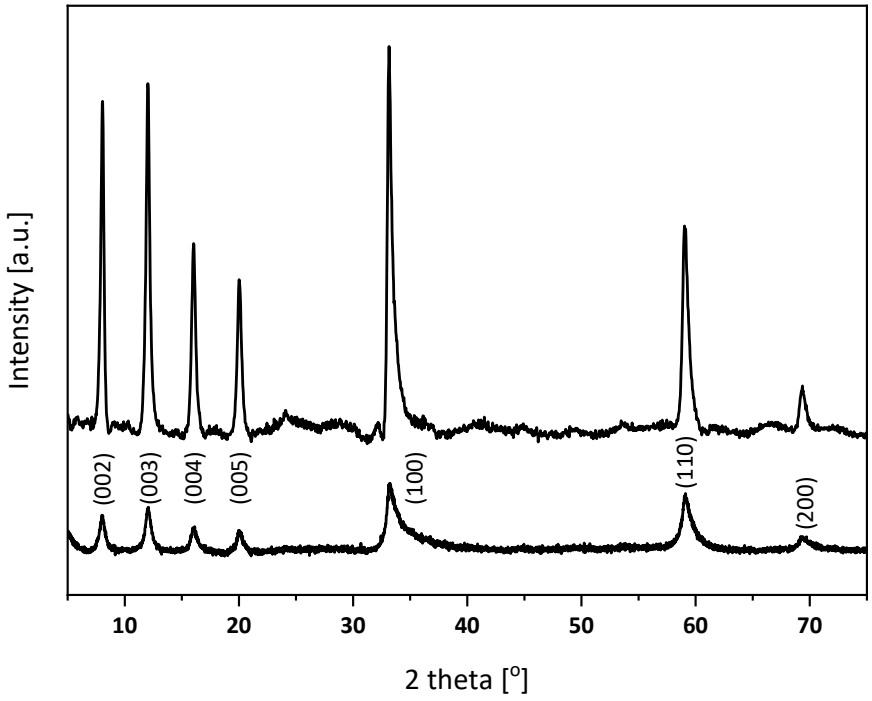

Figure 3.8. Powder X-ray diffraction pattern of LZH-L_3^{O2} synthesised from $ZnEt_2$ (bottom) and from $ZnMes_2$ (top).

Using $ZnMes_2$ in the synthesis of LZH yielded a pale-coloured powder; the resulting diffractogram was in reasonable agreement with powder patterns recorded using $ZnEt_2$ as the organometallic zinc precursor (**Figure 3.8**).

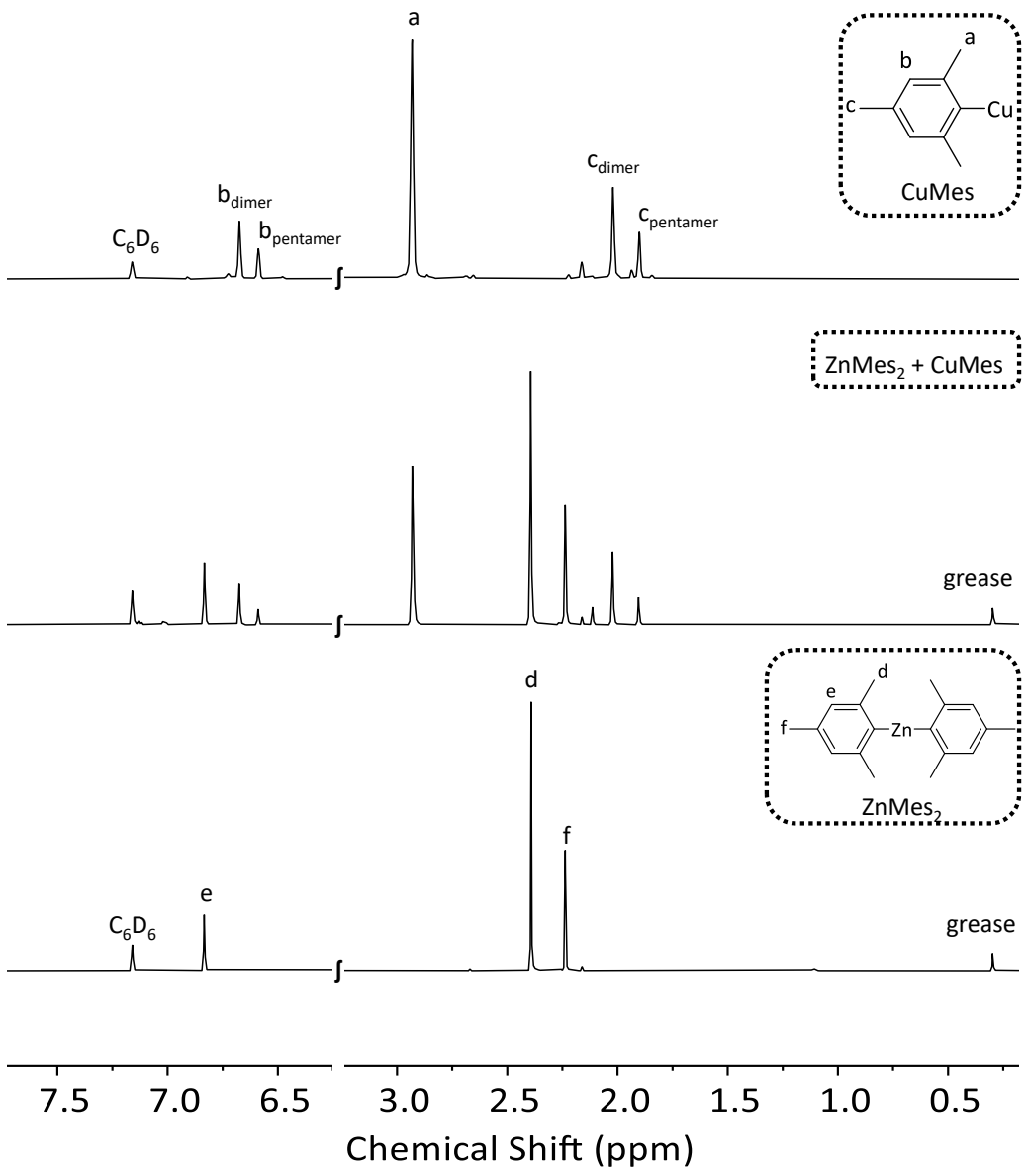

Figure 3.9. ^{1}H NMR spectra in C_6D_6 of $ZnMes_2$ (bottom), $ZnMes_2$ + CuMes (middle), and CuMes (top).

In addition, a 1:1 mixture of CuMes and $ZnMes_2$ in C_6D_6 did not show any black precipitation associated with Cu(0) as previously observed for mixtures with $ZnEt_2$ or $ZnPh_2$ (*vide supra*). Also, the resulting ^{1}H NMR spectrum only showed resonances associated with the individual precursors (**Figure 3.9**, middle). Therefore, $ZnMes_2$ appeared to be an appropriate zinc precursor for the targeted copper doped LZH *via* an organometallic synthetic route.

However, deployment of $ZnMes_2$ as a Zn precursor gave rise to a series of undesirable unidentified reaction products during the attempted synthesis of Cu-doped LZH materials (*vide infra*,

Figure 3.12). Therefore, we turned our attention to commercially available $Zn(C_6F_5)_2$ as an alternative zinc precursor.

A 1:1 mixture of CuMes and $Zn(C_6F_5)_2$ in C_6D_6 afforded a red precipitate which could not be identified *via* pXRD analysis. Since it's ^{1}H NMR spectroscopic analysis showed broadened resonances of CuMes, a dynamic behaviour in the reaction mixture was suggested; perhaps caused by reversible Mes/C_6F_5 ligand exchange (**Figure 3.10**). Note, no black precipitate was observed, indicating no formation of undesired Cu(0).

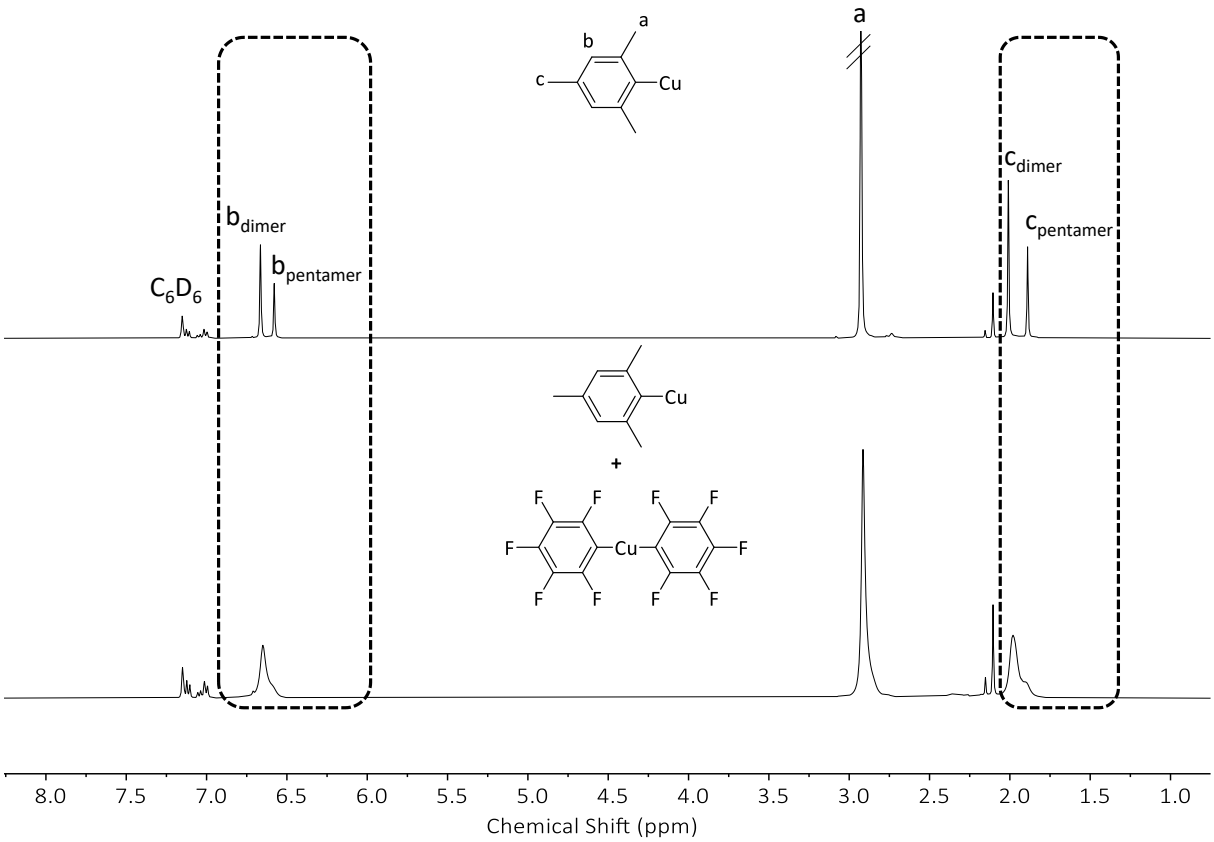

Figure 3.10. ^{1}H NMR spectra of CuMes (top) and CuMes + $Zn(C_6F_5)_2$ (bottom) in C_6D_6.

Furthermore, $Zn(C_6F_5)_2$ was found to be an appropriate zinc precursor for the synthesis of LZH-L_3^{O2} (**Figure 3.11**), and was therefore identified as the most promising zinc source.

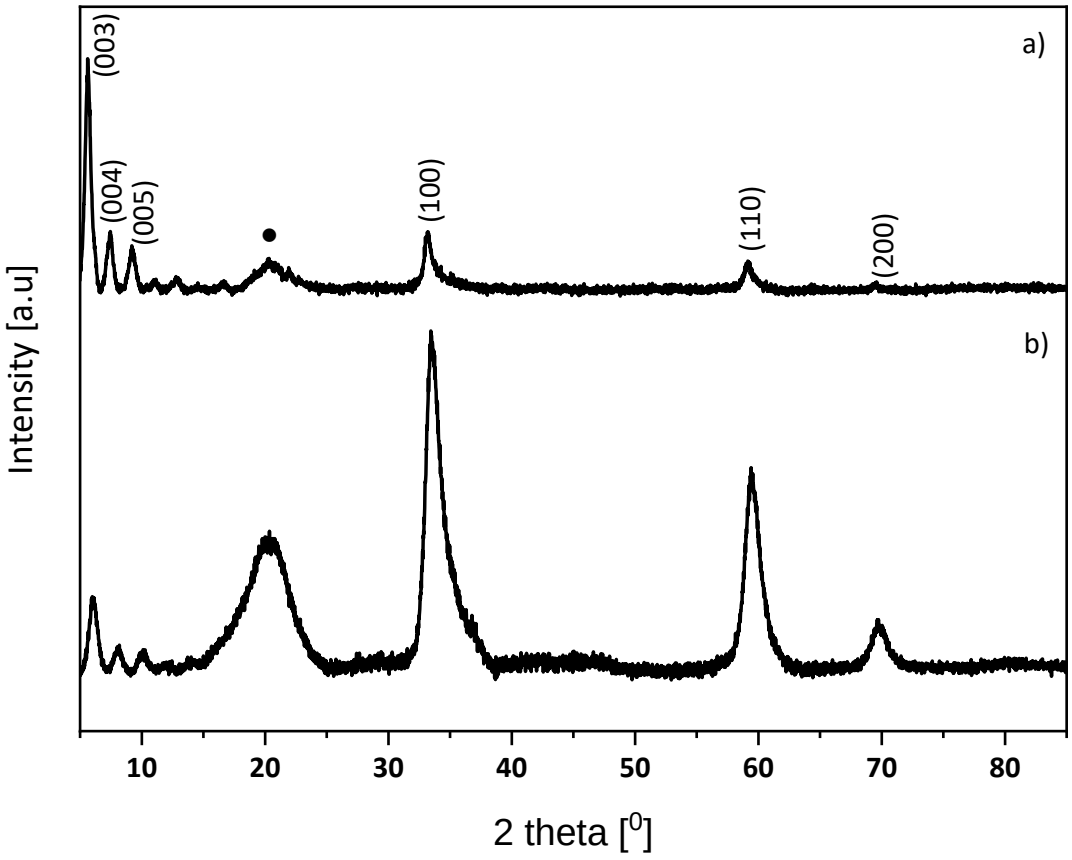

Figure 3.11. Powder X-ray diffraction pattern of a) LZH-L_5^{O2} from $ZnEt_2$ as the reference and b) from $Zn(C_6F_5)_2$. Broad reflection indexed as '·' is caused by the hydrocarbon chain of longer carboxylates.[1]

3.2.1.2.2. Attempted Cu(I) doping of LZH Materials

Cu(I) doped LZH materials are not known in the literature, therefore, we aimed for similar doping levels (2-10 mol % copper) reported for Cu(II) doped LZH-NO_3 synthesised from $Zn(NO_3)_2$ and $Cu(NO_3)_2$ in aqueous solutions with NaOH.[19] In that regard, we attempted to synthesise Cu^{I}_{x}LZH-L_3^{O2} with X = 5, 7.5 and 10 by stirring a precursor mixture of $ZnMes_2$ or $Zn(C_6F_5)_2$, $Zn(L_3^{O2})_2$, and CuMes in toluene at room temperature overnight under an N_2 atmosphere; a ligand loading of $[L_3^{O2}]/[Zn]+[Cu] = 0.6$ was used. Degassed HPLC grade water was added and the reaction mixture was stirred overnight, affording orange solutions. Moreover, the solutions appeared darker in colour with higher levels of doping.

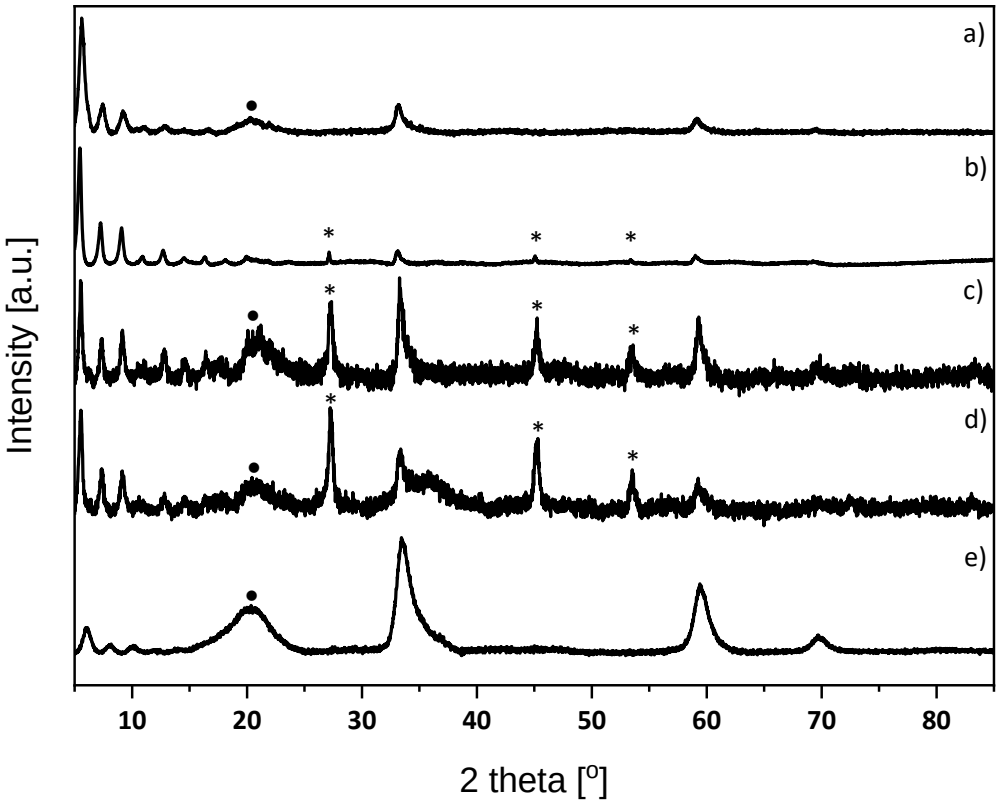

Figure 3.12. Powder X-ray diffraction pattern of Cu^{I}_{x}LZH-L_3^{O2} with a) X = 0 synthesised from $ZnEt_2$ (reference, undoped material) and b) X = 5, c) X = 7.5, d) X = 10 synthesised with $ZnMes_2$ and e) X = 10 synthesised from $Zn(C_6F_5)_2$. Reflections marked with '*' is due to impurities from $Zn(C_9H_{11})_2$ and reflections marked with '•'is due to hydrocarbon chain of longer carboxylates.[1]

The isolated orange solids of Cu^{I}_{x}LZH-L_3^{O2} after drying under reduced pressure showed similar powder diffractograms to white LZH-L_3^{O2} synthesised from $ZnEt_2$ (**Figure 3.12**).[1] However, additional reflections at 27, 45 and 53 2Θ [°] marked with '*' were observed which could not be identify but are speculated to derive from either impurities in $ZnMes_2$ or form during the reaction as undesired byproducts. Changing the zinc precursor and using $Zn(C_6F_5)_2$, which had been identified as the most promising source earlier (*vide supra*), finally enabled the synthesis of impurity-free copper doped LZH (Cu^{I}_{10}LZH-L_3^{O2}) (**Figure 3.12**, e).

Whereas differing intensities of reflections in the powder X-ray diffraction pattern can be attributed to the fact that certain orientations of microcrystalline particles are preferred, and reflection broadening can be caused by the particle size, shifted reflections are generally due to changes in the lattice parameters. Therefore, shifted reflections in the powder X-ray diffraction pattern can be indicative of successful doping. The extent in which the reflections are shifted is related to the nature and quantity of the dopant, which is described in Vegard's law.[20]

Table 3.1: Ionic radii of metal ions with different coordination numbers.[21]

Ion	Coordination	Ionic radius [*r*/pm)
Zn(II)	IV	0.6
	VI	0.74
Cu(I)	IV	0.6
	VI	0.77
Cu(II)	IV	0.57
	VI	0.73

The absence of a second phase based on copper in the powder X-ray diffraction pattern is suggestive of successful incorporation of copper into the zinc lattice. However, it was difficult to verify successful Cu(I) doping by PXRD because it was difficult to determine if a shift in the (110) and (100) reflections occurred. It is possible that the low doping levels paired with very similar ionic radii for 4- and 6-coordinate copper and zinc ions don't provide a clear indication of successful doping based on powder XRD pattern (**Table 3.1**).

Inductively coupled plasma mass spectrometry (ICP-MS) is known for its high sensitivity for detecting atoms at low concentration. Therefore, $Cu^{I}_{10}LZH\text{-}L_3^{O2}$ was analysed by Alaa Abdul-Sada at the University of Sussex to determine the amount of copper present in the sample. The zinc concentration was 21.20 wt.%, which is in reasonable agreement with the calculated zinc content (22.15 wt.%), but the value found for copper (1.44 wt.%) is lower than the expected wt.% of 2.4 %. This led to the hypothesis that the copper is not distributed homogeneously in the sample.

A

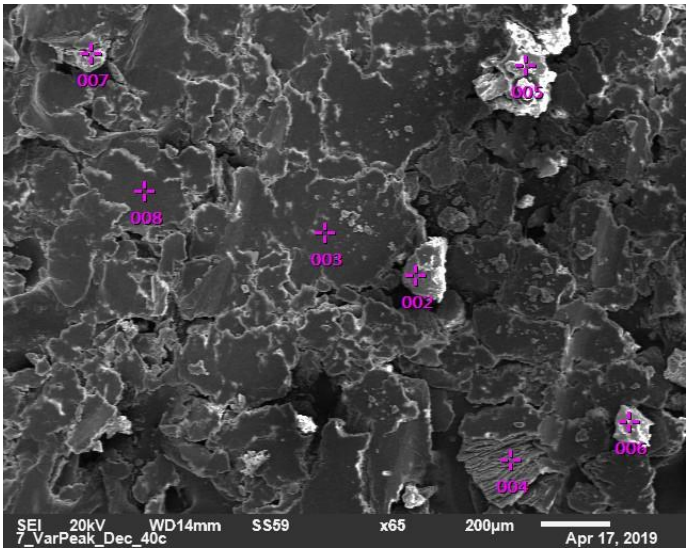

B

Point location	Cu [mol%]
002	-
003	0.81
004	0.86
005	-
006	0.94
007	-
008	0.83
009	0.76

Figure 3.13. (A) SEM image of $Cu^{I}_{5}LZH@\text{-}L_3^{O2}$. (B) Table showing the copper content in [mol%] from Energy Dispersive X-Ray Analysis (EDX) analysis at randomly picked point locations (00X).

Energy-Dispersive X-ray Spectroscopy (EDX) and SEM for a sample of $Cu^{I}_{5}LZH\text{-}L_3^{O2}$ was found to contain different amounts of copper in different selected point locations on the sample (**Figure 3.13**). This is most likely representative of all Cu(I) doping attempts and confirms the presumption that copper is not homogeneously distributed.

Based on these findings, it is concluded that Cu(I) cannot be incorporated into the lattice of layered zinc hydroxide materials *via* the applied organometallic synthesis approach. Instead, Cu_2O nanoparticles and LZH may be formed simultaneously in the one pot synthetic procedure, and Cu_2O isn't

apparent in the pXRD pattern due to both its comparably low fraction of the sample and its very small crystallite size.

3.2.1.3. Attempted Synthesis of Cu(II) doped LZH

As mentioned earlier, Cu(II) doped LZH materials were reported with doping levels ranging from 2-10 mol % copper and were synthesised by co-precipitation of $Zn(NO_3)_2$ and $Cu(NO_3)_2$ in aqueous solutions with NaOH.[19] Thus, the synthesis of Cu^{II}_xLZH-L_3^{O2} with X = 5 and 10 was targeted by the controlled hydrolysis of a mixture consisting of $ZnMes_2$, $Zn(L_3^{O2})_2$ and $Cu(L_3^{O2})_2$, in toluene at room temperature, and a ligand loading of $[L_3^{O2}]/[Zn]+[Cu] = 0.6$. Higher doping levels with X = 15 and 20 were investigated as well to: a) find the Cu(II) doping limit and b) form a Cu-rich single-phase catalyst precursor for CO_2 to methanol conversion. (Note, $ZnMes_2$ was used in this study since $Zn(C_6F_5)_2$ was not identified as a precursor yet).

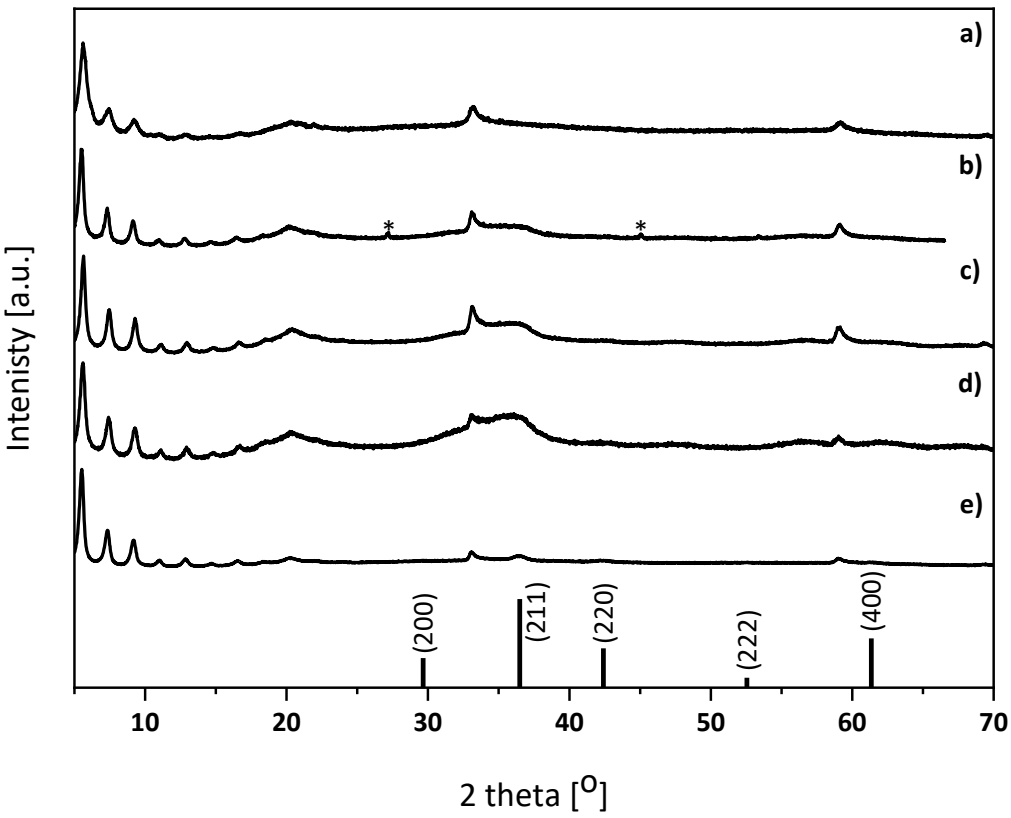

Figure 3.14. Powder X-ray diffraction pattern of (a) LZH-L_3^{O2} synthesised from $ZnEt_2$; Cu^{II}_xLZH-L_3^{O2} with b) X = 5, c) X = 10, d) X = 15, and e) X = 20 synthesised with $ZnMes_2$ as the zinc source. Reflections marked with '*' may be due to impurities from $ZnMes_2$.

Again, as previously seen for Cu(I) doping, the powder X-ray diffraction patterns of Cu^{II}_xLZH-L_3^{O2} are in good agreement with LZH-L_3^{O2}, but a clear shift in the (110) and (100) reflections to confirm the successful incorporation of Cu(II) ions was not possible (**Figure 3.14**). However, it seems likely that the Cu(II) doping limit was <20 mol% due to detection of Cu_2O as a separate phase at higher doping levels. This result is surprising as $Cu(L_3^{O2})_2$ was used as the copper precursor, and *in situ* formation of Cu_2O requires reduction of Cu(II) to Cu(I).

Due to the inconclusive outcome of the Cu(II) doping experiments in this work, previously presented strategies in the literature remain the desired pathway to prepare Cu-containing LZH.[19]

3.3. SUMMARY, CONCLUSIONS AND FUTURE DIRECTIONS

The catalytic activity, selectivity, lifetime and poison resistance of Cu-based catalysts are linked to their method for preparation.[22] Here, an organometallic synthetic approach to Cu-containing hydrotalcite like materials were explored in attempts to deliver catalysts for CO_2 reduction to methanol.

Cu- and Al organometallic reagents were added, in variable stoichiometries, to mixtures of diorgano-zinc reagents and the carboxylic acid. The combined organometallic mixture was hydrolysed and the product characterise. Unfortunately, none of the routes were proven to produce the target doped LZH materials nor to yield LDH. For example, substituting 25 mol % of the $ZnEt_2$ precursor with $AlEt_3$ was investigated as a route to LDH nanosheets. The analytical techniques suggested that amorphous Al_2O_3 was generated alongside very small ZnO nanoparticles, suggesting phase separation was more stable. As ZnAl LDH materials are very well known, it is concluded that LDHs are not accessed in the fully exfoliated state and rather these conditions yield nanoparticles. The attempts to prepare a CuZn htl like materials showed that only specific zinc precursors were stable with respect to CuMes decomposition. Amongst the zinc precursors, bis(pentafluorophenyl)zinc ($Zn(C_6F_5)_2$) was found to be the best choice. However, the formation of a monophasic Cu^{I}_{10}LZH-L_4^{O2} could not be verified by powder X-ray analysis, ICP-MS or EDX. The synthesis of Cu^{II}_{x}LZH-L_4^{O2} was rather inconclusive as Cu_2O nanoparticles were formed as a second phase together with LZH. Consequently, new strategies need to be explored in the future for the synthesis of exfoliated and doped LZH materials. A detailed study on intermediates formed before the controlled hydrolysis of the reaction mixture may help to identify the right conditions to access a monophasic Cu-containing layered material in a one pot synthesis.

3.3 REFERENCES

[1] A. H. M. Leung, S. D. Pike, A. J. Clancy, H. C. Yau, W. J. Lee, K. L. Orchard, M. S. P. Shaffer, C. K. Williams, *Chem. Sci.* **2018**, *9*, 2135-2146.

[2] S. A. Said, C. S. Roberts, J. K. Lee, M. S. P. Shaffer, C. K. Williams, *Adv. Funct. Mater.* **2021**, 2102631.

[3] A. H. M. Leung, *PhD Thesis* **2018**.

[4] K. L. Orchard, *PhD Thesis* **2011**.

[5] P. Gao, F. Li, F. Xiao, N. Zhao, N. Sun, W. Wei, L. Zhong, Y. Sun, *Catal. Sci. Technol.* **2012**, *2*, 1447-1454.

[6] J. Toyir, P. R. r. de la Piscina, J. L. G. Fierro, N. s. Homs, *Appl. Catal. B* **2001**, *34*, 255-266.

[7] G. Chinchen, K. Waugh, *J. Catal.* **1986**, *97*.

[8] J. Yoshihara, C. T. Campbell, *J. Catal.* **1996**, *161*, 776-782.

[9] F. De Luca, R. Menzel, J. J. Blaker, J. Birkbeck, A. Bismarck, M. S. Shaffer, *ACS Appl. Mater. Interfaces* **2015**, *7*, 26783-26791.

[10] A. Lilić, T. Wei, S. Bennici, J. F. Devaux, J. L. Dubois, A. Auroux, *ChemSusChem.* **2017**, *10*, 3459-3472.

[11] D. Lee, H. Takahashi, A. S. Thankamony, J.-P. Dacquin, M. Bardet, O. Lafon, G. De Paëpe, *J. Am. Chem. Soc.* **2012**, *134*, 18491-18494.

[12] S. Miao, R. N. d'Alnoncourt, T. Reinecke, I. Kasatkin, M. Behrens, R. Schlögl, M. Muhler, *Eur. J. Inorg. Chem.* **2009**, 910-921.

[13] E. M. Meyer, S. Gambarotta, C. Floriani, A. Chiesi-Villa, C. Guastini, *Organometallics* **1989**, *8*, 1067-1079.

[14] S. Barman, S. Vasudevan, *J. Phys. Chem. B* **2007**, *111*, 5212-5217.

[15] O. Berkesi, I. Dreveni, J. A. Andor, J. Mink, *Inorg. Chim. Acta* **1992**, *195*, 169-173.

[16] J. E. Borger, M. S. Bakker, A. W. Ehlers, M. Lutz, J. C. Slootweg, K. Lammertsma, *Chem. Commun.* **2016**, *52*, 3284-3287.

[17] M. Hayashi, M. Bolte, M. Wagner, H. W. Lerner, *Z. anorg. Allg. Chem.* **2011**, *637*, 646-649.

[18] S. C. Cole, M. P. Coles, P. B. J. D. T. Hitchcock, *Dalton Trans.* **2003**, 3663-3664.

[19] M. Y. Ghotbi, N. Bagheri, S. Sadrnezhaad, *Adv. Powder Technol* **2012**, *23*, 279-283.

[20] C. F. Holder, R. E. Schaak, *ACS Nano* **2019**, *13*, 7359−7365.

[21] *http://abulafia.mt.ic.ac.uk/shannon/ptable.phpaccessed (accessed November 2021)*.

[22] J. Zhong, X. Yang, Z. Wu, B. Liang, Y. Huang, T. Zhang, *Chem. Soc. Rev.* **2020**, *49*, 1385-1413.

Chapter 4:

Novel Catalysts for CO_2/PO Ring Opening Copolymerisation

4 NOVEL CATALYSTS FOR CO_2/PO RING OPENING COPOLYMERISATION

4.1 BACKGROUND AND SCOPE

The primary objective of this chapter is to identify, synthesise and test new zinc-based heterogeneous catalysts for the ring opening copolymerisation (ROCOP) of propylene oxide (PO) and carbon dioxide to form poly(propylene carbonate) (PPC). Ideal catalytic systems should be cost effective, non-toxic, easy to prepare and handle, generate colourless materials with minimal by-products and allow good control over the yield, molecular mass and microstructure of the generated polymers.[1]

Zinc glutarate (ZnGA) is a well known heterogeneous catalyst, with the active site proposed to combine a Zn-carboxylate scaffold and Zn-hydroxyl initiating species.[1-3] Catalytic activity depends strongly upon factors including: the choice of precursor, high ZnGA surface area, high degree of crystallinity and surface structures showing Zn–Zn distances of 4.3–5 Å (please refer to the introduction for more details). Until today it is the most powerful zinc based heterogeneous catalyst for the copolymerisation of PO with CO_2.

Less active zinc based heterogeneous catalysts were either prepared from $ZnEt_2$/mono-carboxylic mixtures or dicarboxylic acids other than glutaric acid, (please refer to the introduction). In 2011 our group revisited monocarboxylic zinc based catalytic systems by studying well-defined ethylzinc acetate complexes with ligand stoichiometries of 1:1 [EtZn(OAc)] and 3:2 $[Zn_5(OAc)_6(Et)_4]$ in the copolymerisation of CO_2 with PO.[4] Preliminary tests showed no catalytic activity for PO/CO_2 copolymerisation but low conversions (24 – 41 mol polymer/mol epoxide) towards cyclohexene

oxide/CO_2 copolymerisation. Polymers formed at 15 atm CO_2, 80 °C over 7.5 h contained up to 66 % carbonate linkages.[4]

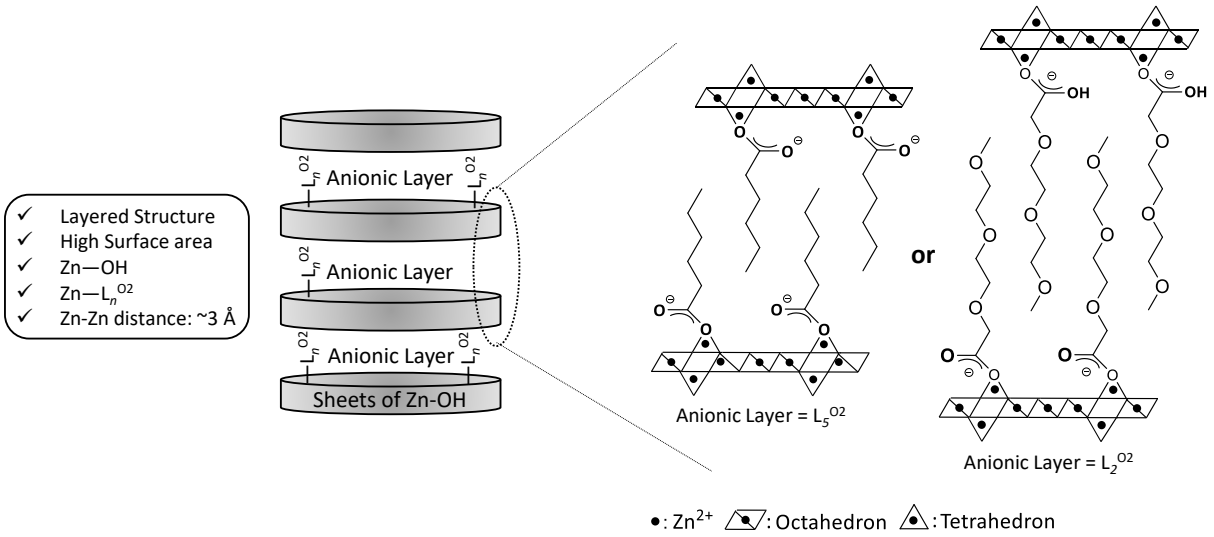

Scheme 4.1. Schematic structure of layered zinc hydroxides (LZH) comprised of edge sharing octahedral sheets of zinc cations contain hydroxide ions on the vertices that connect to form infinite 2D sheets and intercalated anions (L_n^{O2}, n = 2 or n = 5). Enlargement of the interlayer spacing when hexanoate (L_5^{O2}) or 2-[2-(2-Methoxyethoxy)ethoxy]acetate (L_2^{O2}) is used. Zn—Zn distance was obtained from multiplying the d_{110} spacing (calculated using Bragg equation) by a factor of 2.

Controlled hydrolysis of $ZnEt_2$:carboxylate complexes with a ligand loading of 0.6 ([COOR]/[Zn]) were found later to yield layered zinc hydroxide materials (LZH) intercalated by monocarboxylates.[5,6] Layered materials have previously been used as efficient support materials in ethylene polymerisation catalysis.[7-10] In this work the crystalline LZH material was identified as a potential catalyst for copolymerisation as it features both Zn-hydroxide and Zn-carboxylate groups, and has a Zn–Zn distance of ~3 Å (determined from the 110 Bragg reflection in the powder X-ray diffractogram). Exfoliation into 2D nanosheets would yield a material with high surface area (Scheme 4.2).

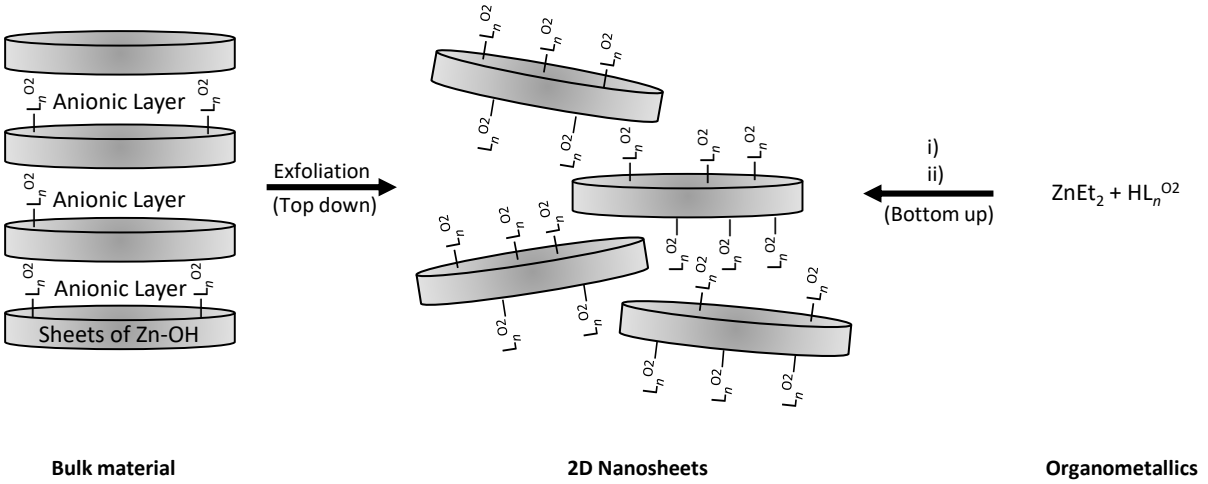

Scheme 4.2. Accessing monolayers of layered materials *via* exfoliation of bulk material or *via* the organometallic synthesis approach by the controlled hydrolysis of $ZnEt_2$ with 0.6 eq. HL_n^{O2}. With i) Toluene, 20 °C, 16 h, ii) 1.6 equiv. of H_2O (relative to zinc), 20 °C, 3 h.[6]

Conventional exfoliation of LZH materials to 2D nanosheets requires rather damaging conditions, including reflux in high temperature solvents, ultra-sonication, high-shear ball milling, or use of exfoliating agents (Scheme 4.2, top down).[5,6] Such conditions are required due to the strongly coordinating carbonates found between the interlayer galleries, formed either directly during the synthesis or by reactions of intercalated water with atmospheric CO_2.[5,6] In contrast, we recently reported a direct, synthesis of exfoliated LZH *via* the hydrolysis of dialkyl zinc reagents (Scheme 4.2, bottom up).[5] The extent of exfoliation was strongly dependent on the carboxylate and solvent.[6] Carboxylic acids bearing hydrophobic alkyl chains formed exfoliated nanosheets in apolar solvents, whereas hydrophilic alkyl ether carboxylic acids resulted in LZH exfoliation in polar solvents.[28,29] Here, the exfoliated nanosheets of LZH-L_5^{O2} and LZH-L_2^{O2}, will be tested in catalysis. These species should show different extents of exfoliation due to the different substituents; LZH-L_2^{O2} is expected to result in greatest catalyst surface area. As control reactions, the catalytic activity of zinc bis(hexanoate), $Zn(L_5^{O2})_2$, and ZnO nanoparticles, capped with hexanoate, ZnO@L_5^{O2}, will be investigated; as the hydrolysis of $ZnEt_2$ in the presence of carboxylates forms 50 wt% LZH, ZnO (6 wt.%) and zinc bis(carboxylate) (44 wt.%), with the latter species proposed to be located between the layers (determined using UV-Vis spectroscopy and elemental analysis respectively).[5]

This chapter outlines the synthesis and activity of LZH and the control species ZnO@L_5^{O2} and zinc bis(hexanoate), $Zn(L_5^{O2})_2$, to be tested as catalysts for PO/CO_2 ROCOP. The structures are illustrated in **Table 4.1**.

Table 4.1. Simplified structures of catalyst tested in Copolymerisation of PO/CO_2.

Hexanoate Series	Polyethylenglycol Series
$[Zn_5(OH)_8(L_5^{O2})_2]\cdot L_5^{O2}$ LZH-L_5^{O2} M = 808.4 [g/mol]	$[Zn_5(OH)_8(L_2^{O2})_2]\cdot L_2^{O2}$ LZH-L_2^{O2} M = 994 [g/mol]
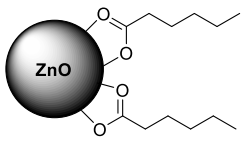 ZnO@L_5^{O2} M = 92 [g/mol]	
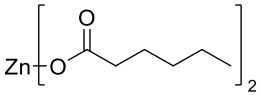 $Zn(L_5^{O2})_2$ M = 295.68 [g/mol]	

Catalyst performance criteria include activity, productivity and selectivity. The polymer selectivity describes the relative amounts of poly(propylene carbonate) (PPC) vs. propylene carbonate (PC – 5 membered heterocycle, which is stable with respect to any further polymerisation). It is typically measured using NMR spectroscopy of the crude reaction product by comparing the relative integrals for PPC against PC and makes use of an internal standard (mesitylene). Catalysts productivity is typically assessed as the quantity of polymer yielded (g) per weight of zinc added (g). Productivity may be enhanced by optimising of the reaction conditions, such as changing CO_2 pressure, temperature, and catalyst loading. The catalysis will be benchmarked against the literature data for the known zinc glutarate ZnGA catalyst, synthesised from $ZnEt_2$.

4.2 Catalyst Synthesis and Characterisation

The synthesis and characterisation of LZH-L_n^{O2} (n = 4 or n = 5) was already reported (**Scheme 4.3**).[5,6] The synthesis involves the controlled hydrolysis (1.6 equiv. H_2O relative to [Zn]) of diethyl zinc in the presence of either HL_2^{O2} or $Zn(L_5^{O2})_2$ at a molar ratio of ligand to metal, $[HL_n^{O2}/Zn] = 0.6$ (n = 4 or n = 5). The reaction was scaled-up by 20 times compared to the reported procedure which required the addition of water to be at 0 °C to prevent the formation of a by-product. The by-product shows basal reflections (00*l*) at lower 2 theta [°] (<20°) perhaps originating from different ligand chain orientations or other formed molecular species.

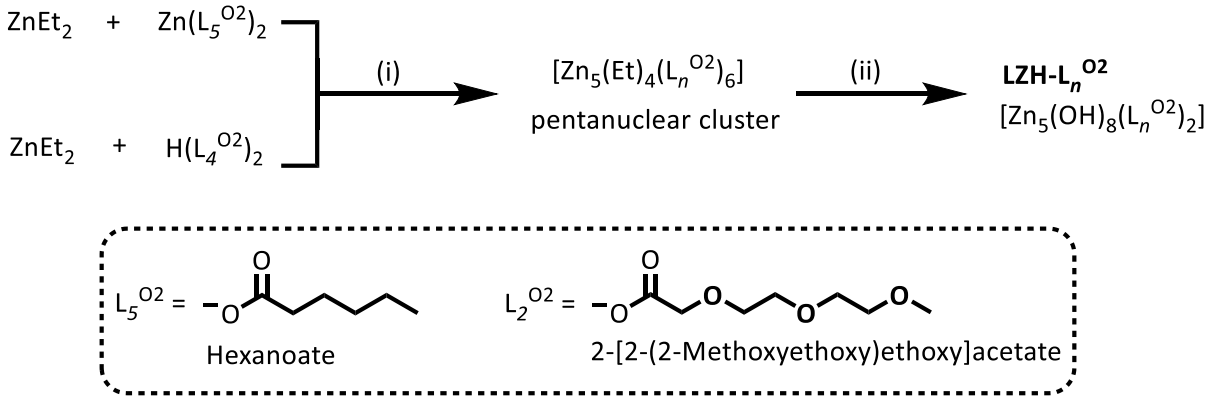

Scheme 4.3. Synthesis of LZH-L_n^{O2} (n = 4 or n = 5) catalysts for copolymerisation of PO/CO_2. Organometallic synthesis of LZH-L_5^{O2} and LZH-L_2^{O2} with i) Toluene, 20 °C, 16 h; ii) 1.6 equiv. of H_2O relative to [Zn], 0 °C, 3 h.

Thus, the two new catalysts were synthesised by adding a solution of $ZnEt_2$ to a solution of HL_2^{O2}, or $Zn(L_5^{O2})_2$, in toluene. The reaction is known to form a mixture of a pentanuclear organometallic cluster compound, $[Zn_5(Et)_4(L_n^{O2})_6]$, together with unreacted $ZnEt_2$. The addition of stoichiometric amounts of milli-Q water, relative to zinc, allowed the formation of LZH-L_n^{O2} (n = 4 or n = 5). Removal of toluene from the crude reaction mixture yielded the catalysts as white solids. Product characterisation by means of powder X-ray analysis (**Figure 4.1**) and IR spectroscopy (**Figure 4.2**) confirmed the formation of LZH-L_n^{O2} (n = 4 or n = 5) with constant composition.

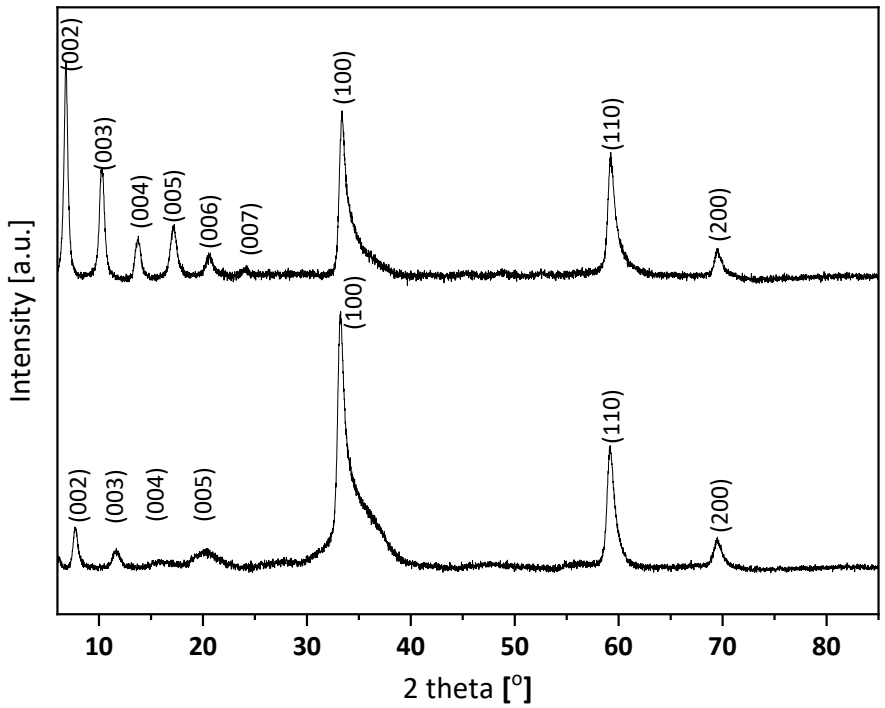

Figure 4.1. Powder X-ray diffractograms of LZH-L_2^{O2} (top) and LZH-L_5^{O2} (bottom).

Powder X-ray diffraction confirmed the formation of LZH-L_n^{O2} (n = 4 or n = 5) as the only crystalline product (**Figure 4.1**). The characteristic equally spaced basal reflections (00*l*) with *l* = 1,2,3, etc. at low 2 theta [°] (<20°), as well as the in-plane reflections (100), (110) and (200), are fully consistent with previous reports of LZH.[5,6]

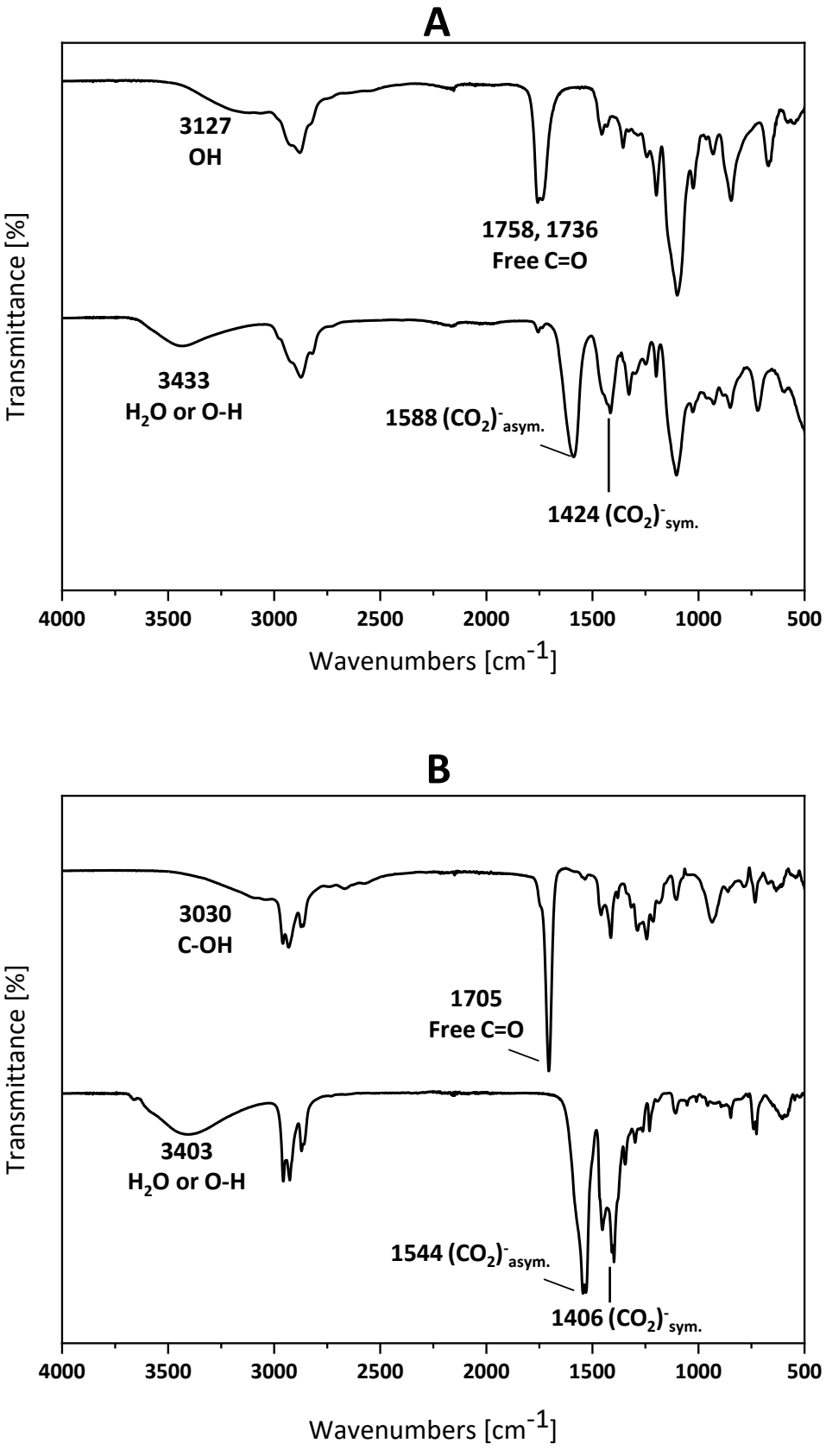

Figure 4.2. FT-IR spectra of A) HL_2^{O2} (top) and LZH-L_2^{O2} (bottom); B) HL_5^{O2} (top) and LZH-L_5^{O2} (bottom).

The Fourier-transform infrared (FTIR) spectra of both samples showed broad O–H stretches (ν = 3433 cm^{-1} for LZH-L_2^{O2} and 3403 cm^{-1} for LZH-L_5^{O2}) assigned to surface hydroxyl groups (O–H) and water molecules. The successful coordination of L_n^{O2} (n = 2,5) as a carboxylate was confirmed by the disappearance of stretches associated with free carboxylic acid, at 1758, 1736 cm^{-1} for LZH-L_2^{O2} and 1705 cm^{-1} for LZH-L_5^{O2}, and by the presence of stretches associated with surface coordinated carboxylate ligands ($\nu_{asym.}$ CO_2^- 1588, $\nu_{sym.}$ CO_2^- 1424 cm^{-1} for LZH-R_2^{O2} and $\nu_{asym.}$ CO_2^- 1544, $\nu_{sym.}$ CO_2^- 1406 cm^{-1} for LZH-R_5^{O2} see **Figure 4.2**, A and B respectively)

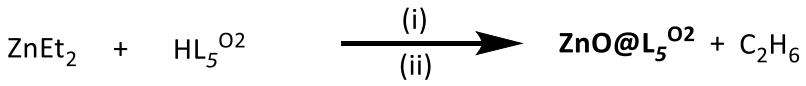

Scheme 4.4. Organometallic synthesis of ZnO@L_5^{O2} with i) Toluene, 2 h, 20 °C; ii) 0.4 M H_2O in acetone, 2 ; centrifugation, 3 x re-dissolving in toluene, precipitation with acetone.

To make the zinc oxide nanocatalyst control sample, ZnO@L_5^{O2} was synthesised (**Scheme 4.4**).[11,12] $ZnEt_2$ was reacted with 0.1 equiv. of the corresponding carboxylic acid (HL_5^{O2}) in toluene. After 2 h the dropwise addition of water, in acetone (0.4 M), results in the release of ethane gas and the formation of the ligated zinc oxide nanoparticles. A cloudy mixture was obtained after 2 h, indicating complete hydrolysis. The nanoparticles were isolated by centrifugation, at 3900 rpm for 10 minutes, and the residue was repeatedly (re-)dissolved in toluene, and precipitated using acetone 3 times. Finally, the sample was dried in vacuo, overnight to remove any solvent residues.

The product is Wurtzite ZnO nanoparticles using powder XRD (**Scheme 4.3**, A). The crystallite size was determined to be ~5 nm for ZnO@L_5^{O2} by applying the Scherrer equation. Evidence for surface coordination of $[L_5^{O2}]^-$ is provided by the change to the carbonyl stretches for free acid (ν C=O 1705 cm^{-1}) and the asymmetric (ν_{asym} CO_2^- 1544 cm^{-1}) and symmetric (ν_{sym} CO_2^- 1406 cm^{-1}) zinc-carboxylate stretches.

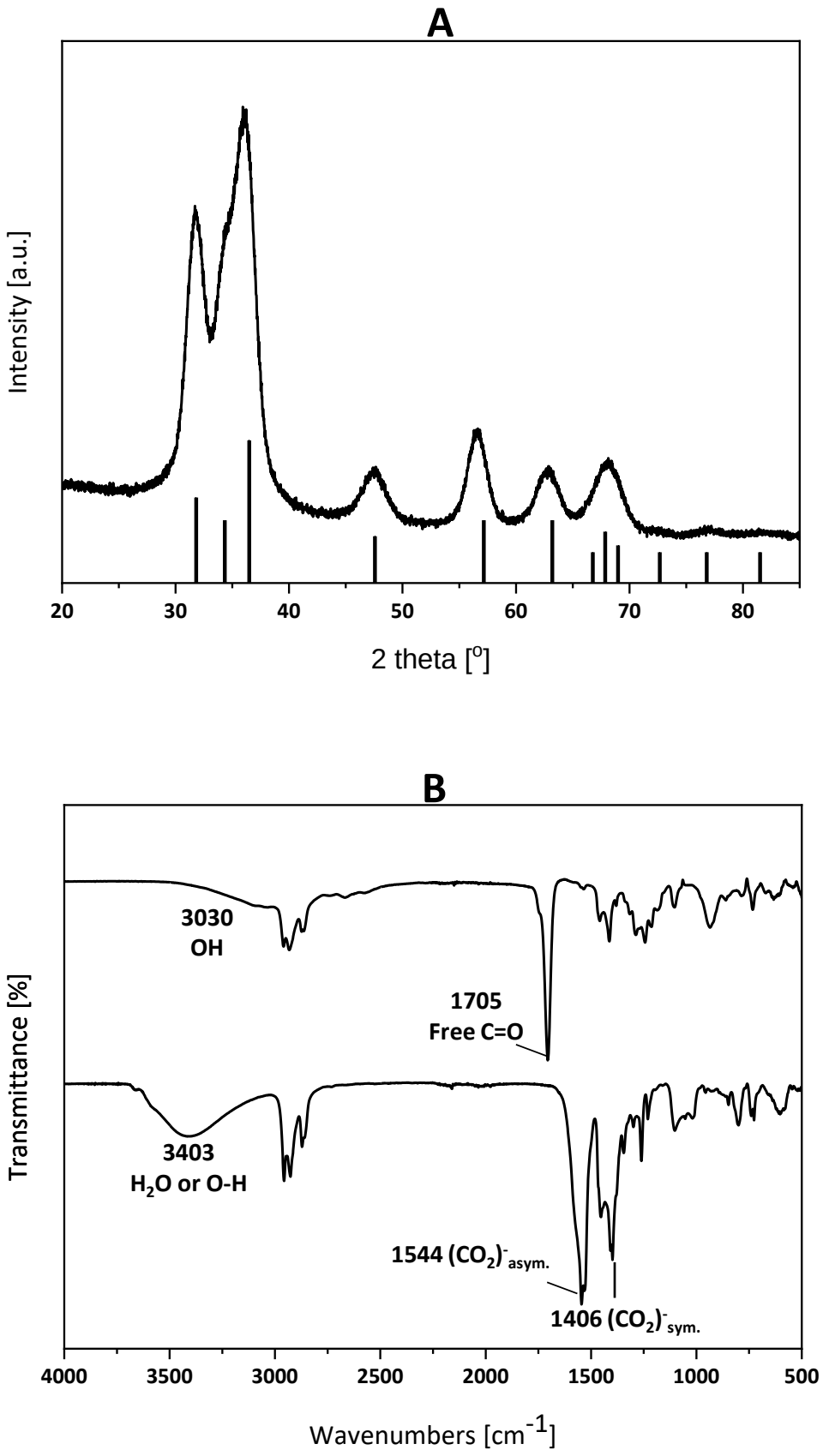

Figure 4.3. A) Powder X-ray diffractograms of ZnO@L_5^{O2} indexed against ZnO (JCPDS card no.: 00-001-1136). B) FT-IR spectra of HL_5^{O2} (top) and ZnO@L_5^{O2} (bottom).

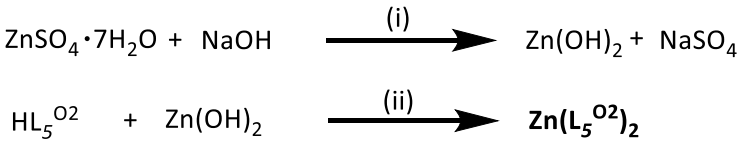

Scheme 4.5. Synthesis of $Zn(L_5^{O2})_2$ with i) water, ii) 126 °C, 20 min, *n*-Octane.

$Zn(L_5^{O2})$ was isolated following a two-step literature procedure (**Scheme 4.5**).[13] Firstly, $Zn(OH)_2$ was freshly prepared by the reaction of $ZnSO_4{\cdot}7H_2O$ and NaOH. Next, 1 equiv. $Zn(OH)_2$ was reacted with 3 equiv. L_5^{O2} in boiling *n*-octane. A white solid formed, which was isolated by filtration, dissolved in hot chloroform and filtered to remove any unreacted $Zn(OH)_2$. As the chloroform supernatant cooled, the product formed as a precipitate, was filtered and dried (air), and used as such.

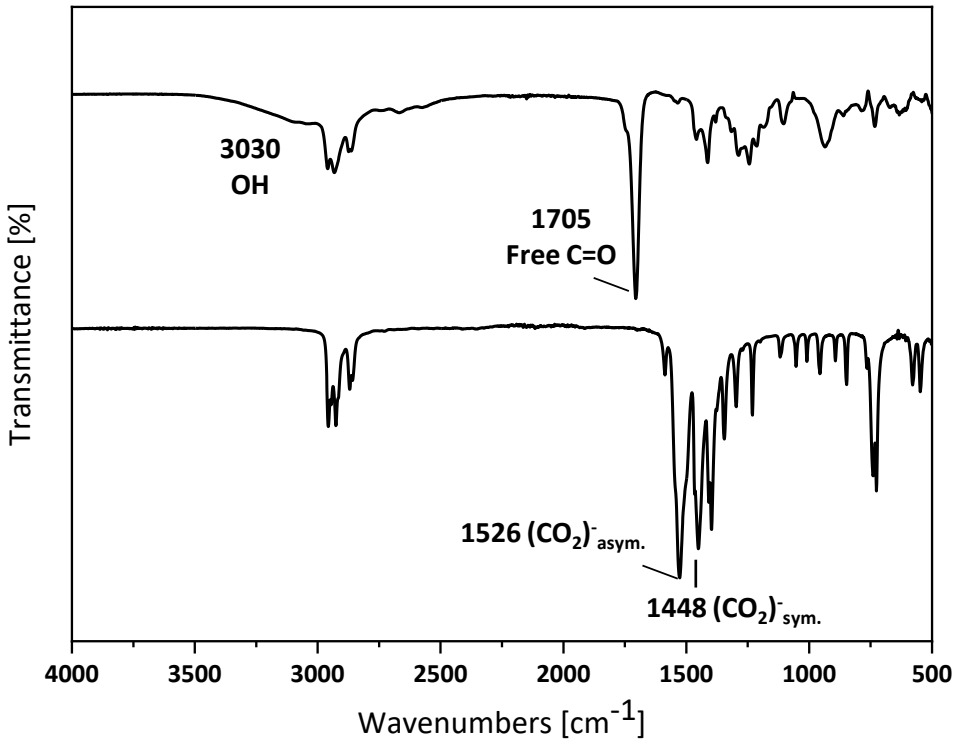

Figure 4.4. FT-IR spectra of HL_5^{O2} (top) and $Zn(L_5^{O2})_2$ (bottom).

The zinc carboxylate product $Zn(L_5^{O2})_2$ shows a Fourier-transform infrared (FTIR) spectrum free from any stretches associated with free HL_5^{O2} (ν C=O 1705 cm^{-1}) and showing stretches consistent with coordinated carboxylate groups ($\nu_{asym.}$ CO_2^- 1526 cm^{-1} and $\nu_{sym.}$ CO_2^- 1448 cm^{-1}, **Figure 4.4**). The product purity was good as assessed by elemental analysis ($ZnC_{12}O_2H_{22}$ C, 48.7; H, 7.5; O, 21.6 found C, 48.8; H, 7.5; O, 20.8).

4.3 CATALYTIC TESTING

All catalysts were tested in the ROCOP of CO_2 with PO (**Scheme 4.6** and **Table 4.2**). The polymerisations were carried out at 50 °C, using 0.1 g of $[Zn]_0$, at 40 bar CO_2 pressure and using neat propylene oxide (20 mL). These conditions were found to give the best activities in previous investigations using the heterogeneous catalyst ZnGA.[14]

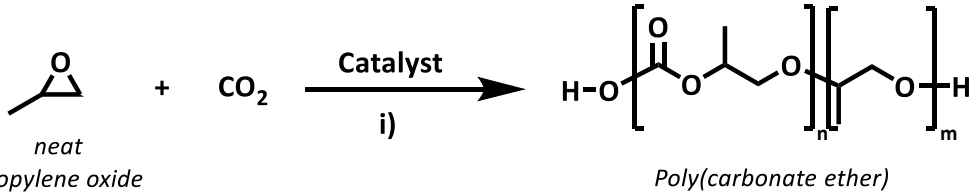

Scheme 4.6. Polymerisation catalysis using propylene oxide (PO) and CO_2 to make PPC. Where n = number of carbonate linkages and m = number of ether linkages. i) 50 °C, 40 bar, 0.1 g $[Zn]_0$.

All catalysts were active and formed polymer with moderate/low yields (0.05 – 1.15 g) after prolonged reaction times (68 – 119 hours). The LZH catalysts both show higher productivity than the control compounds and LZH-L_2^{O2} shows the highest productivity of the series. The polymers all show high CO_2 uptake with the percentage of carbonate linkages >80% in all cases. All polymers showed the same regiochemistry, with slight head-to-tail enrichment (77%) compared to tail-to-tail (12%) or head-to-head (11%) linkages (**Table 4.2**).

Table 4.2. Catalyst performance data in the ROCOP of CO_2/PO.

Entry	Catalyst	Time [h]	Yield [g][c]	F_{CO2} [%][d]	Productivity[e] [g/g]	Microstucture (TT/HT/HH) [%][f]	M_n [Đ] [g/mol][i]
1[a]	$Zn(L_5^{O2})_2$	119	0.05 (±0.003)	89	0.5 (±0.03)	n.d	16500 [3.5]
2[a]	$ZnO@L_5^{O2}$	88	0.20 (±0.010)	98	1.9 (±0.10)	12/77/11	21300 [7.2]
3[a]	LZH-L_5^{O2}	68	0.50 (±0.025)	98	5.0 (±0.25)	13/77/10	n.d.
4[b]	LZH-L_2^{O2}	78	1.15[g] (±0.058)	73[h]	11.5 (±0.58)	11/78/11	7600 [12.8]

[a]Reaction conditions: Catalyst (0.1 g $[Zn]_0$; 461 mg $Zn(L_5^{O2})_2$/145.5 mg $ZnO@L_5^{O2}$/256.4 mg LZH-L_5^{O2}), PO (20 mL), 40 bar CO_2, 50°C. [b]Reaction conditions: Catalyst (0.1 g $[Zn]_0$; 320 mg LZH-L_2^{O2}), PO (20 mL), 40 bar CO_2, 50°C, 100 µL Mesitylene was used as an internal standard. [c]Grams of polymer isolated per 0.1 g Zn. [d]Carbonate content of polymers, determined by ^{1}H NMR spectroscopy. [e]Productivity = grams polymer/grams of $[Zn]_0$. [f]TT = Tail to Tail, HT = Head to Tail, HH = Head to Head connectivity determined by ^{13}C {^{1}H} NMR of polymers. [g]Grams of alternating poly(propylene carbonate) determined from crude ^{1}H NMR compared with mesitylene [h]Carbonate content of polymers determined from the relative integrals in the crude ^{1}H NMR spectra of PPC (4.92 ppm) compared with ether linkages (3.46-3.32 ppm). [i]Determined by GPC analysis, in THF, calibrated with poly(methyl methacrylate) standards.

$Zn(L_5^{O2})_2$ displays the lowest activity with a productivity of 0.5 g/g $[Zn]_0$ but is more active than catalytic systems based on $ZnEt_2$–carboxylic acid (1:1) where it was reported that only traces of polymer was detected.[15] ZnO@L_5^{O2} shows a slightly greater productivity (1.9 g/g $[Zn]_0$), whereas LZH-L_5^{O2} shows a marked improvement in productivity to 5 g/g $[Zn]_0$. The results indicate there are benefits to applying these layered materials in this polymerisation catalysis and it may arise from greater catalyst surface areas and/or more accessible active sites. Changing the hexanoate ligand (L_5^{O2}) for the more polar 2-[2-(2-methoxyethoxy)ethoxy]acetate ligand, $[L_2^{O2}]^-$, resulted in a two-fold increase in productivity (5 vs. 11.5 g/g $[Zn]_0$). The productivity enhancement is tentatively attributed to the polar alkylether carboxylate ligand, which may result in greater exfoliation in the polar propene oxide medium and hence form a greater density of active sites.

To test the notion that the most productive catalyst was exfoliated under the conditions of the catalysis, a sample of LZH-L_2^{O2} in PO was examined. The sample formed a transparent solution and Tyndall scattering was observed which is consistent with the formation of a stable colloidal solution of exfoliated LZH-L_2^{O2} (**Figure 4.5**, right). In contrast, LZH-L_5^{O2} in PO formed a precipitate and no light scattering was observed (**Figure 4.5**, left) – i.e. there is unlikely to be significant catalyst exfoliation during reaction. The notion that an increase in catalyst surface area enhances activity is in line with previous observations using ZnGA.[2]

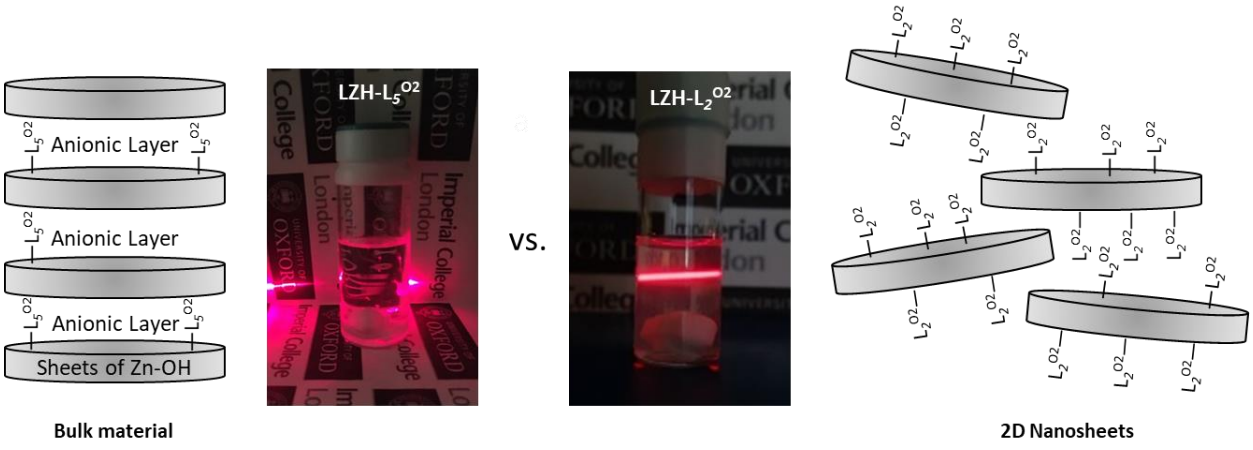

Figure 4.5. Tyndall effect using solutions/suspensions of LZH-L_5^{O2} (left) and LZH-L_2^{O2} (right) in PO.

The catalyst LZH-L_2^{O2} also formed a greater proportion of ether linkages (27%). These linkages form by sequential epoxide insertion and can signal an increase in the Lewis acidity of the Zn active site. It may be that the carboxylate ligand influences the electron density at the zinc active sites, as well as controlling the extent of sheet exfoliation.

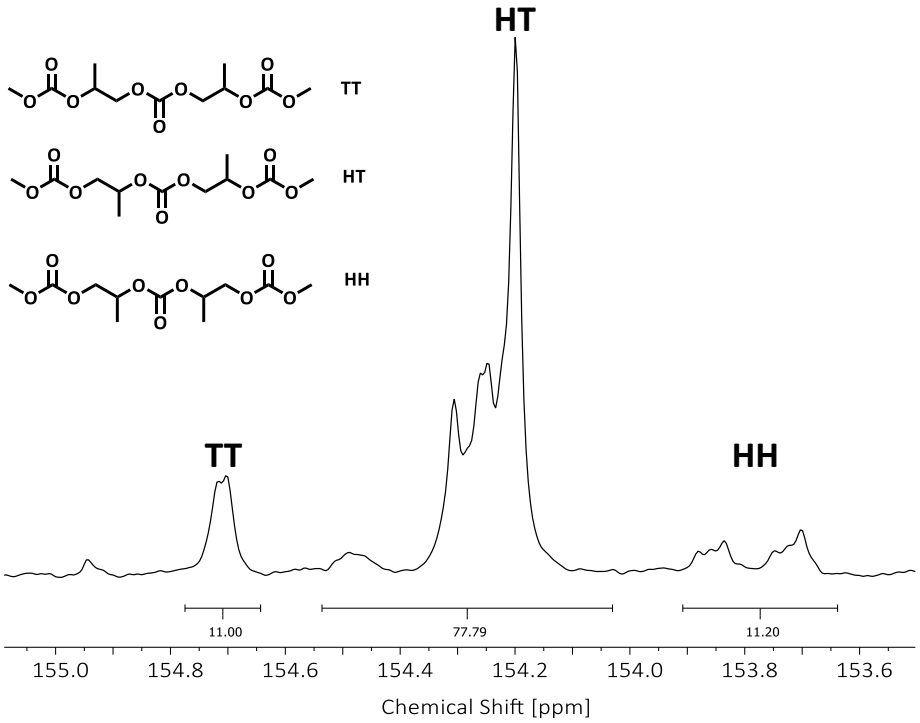

Figure 4.6. Exemplar ^{13}C {^{1}H} NMR spectrum of poly(propylene carbonate) synthesised by LZH-L_2^{O2}.

In addition quantitative ^{13}C {^{1}H} NMR spectroscopy of PPC, isolated when using the catalysts LZH-L_2^{O2}, revealed that the polymers are head-to-tail linkage enriched (up to 78 %) (**Table 4.2** and **Figure 4.6**). Compared with heterogeneous catalysts the regioselectivity is more consistent with double metal cyanide catalysts (Zn-Co-DMC forms mostly head-to-tail linkages) than ZnGA (30:60:30; TT:HT:HH).[16,17]

Since LZH-L_2^{O2} was the most productive catalyst and showed good regioselectivity, it warranted further optimisation despite the comparable lower molar mass (7600 g/mol) and highest polydispersity ($Đ$ = 12.8) of the resulting polymer.

4.3.1 EFFECT OF CO_2 PRESSURE

The effect of CO_2 pressure on the catalytic performance of LZH-L_2^{O2} was investigated from 1 to 40 bar, at 50 °C, using 0.05 g $[Zn]_0$ per 10 mL PO, over 78 hours (**Table 4.3**).

Table 4.3. Catalytic data for the ROCOP of CO_2/PO with LZH-L_2^{O2} at different scales and pressures.

Entry	CO_2 Pressure [bar]	Conv. [%][c]	CO_2 [%][d]	Polym. [%][e]	Yield [g][f]	F_{CO2} [%][g]	Productivity [g/g][h]	M_n [Đ] [g/mol][i]
1[a]	1	6.3	61	56	0.2 (±0.01)	n.d	6.5 (±0.33)	6700 [10.9]
2[a]	10	9.9	74	66	0.7 (±0.04)	n.d	14.1 (±0.71)	n.d.
3[a]	20	11.0	80	66	0.8 (±0.04)	n.d	16.4 (±0.0.8)	6900 [13.2]
4[b]	20	10.7	80	66	1.6 (±0.08)	78	16.3 (±0.82)	n.d.
5[b]	40	7.0	79	65	1.2 (±0.06)	83	11.5 (±0.58)	7500 [12.8]

[a]Reaction conditions: Catalyst (0.05 g $[Zn]_0$ = 160 mg LZH-L_2^{O2}), 50°C, 78 h, 50 µL mesitylene as an internal standard. [b]Reaction conditions: Catalyst (0.1 g $[Zn]_0$ = 320 mg LZH-L_2^{O2}), 50°C, 78 h, 50 µL mesitylene as an internal standard. [c]PO conversion determined from the sum of the relative integrals in the crude ^{1}H NMR spectra of PPC (4.92 ppm), PC (77 ppm) and ether (3.46-3.32 ppm) compared to mesitylene. [d]CO_2 selectivity determined by the relative integrals from the crude ^{1}H NMR spectra of PPC (4.92 ppm) and PC (4.77 ppm) compared with ether linkages (3.46-3.32 ppm). [e]Polymer selectivity determined from the relative integrals in the crude ^{1}H NMR spectra of PPC (4.92 ppm) and PC (4.77 ppm). [f]Grams of alternating poly(propylene carbonate) determined from the crude ^{1}H NMR spectra compared with mesitylene. [g]Carbonate contents of polymers determined from the ^{1}H NMR of the polymers. [h]Productivity = grams polymer/grams Zn. [i]Determined by GPC analysis, in THF, calibrated with poly(methyl methacrylate) standards.

Catalyst LZH-L_2^{O2} was active across the pressure range 1 – 40 bar. CO_2-uptake increased from 1 – 20 bar (60 - 80%) suggesting some CO_2 insertion rate dependence at lower CO_2 pressures, which has been seen in a double metal cyanide catalyst.[18] Consequently, a slight reduction in cyclic carbonate formation is observed from 1 to 10 bar, and, over the same pressure range, an increase in productivity is observed (6.5 – 14.1 g/g $[Zn]_0$). A slight reduction in productivity is observed at 40 bar (11.5 g/g $[Zn]_0$), which might be attributed to pressure induced solvent swelling in the sub-supercritical regime which reduces the overall catalyst concentration.[19]

4.3.2 Effect of Reaction Temperature

The polymerisation temperature influence on the catalytic activity of LZH-L_2^{O2} was investigated over 10 °C increments from 50 to 80 °C. A catalyst loading of 0.05 g $[Zn]_o$ in 10 mL PO was used (**Table 4.4**).

Table 4.4. Catalytic data for the ROCOP of CO_2/PO with LZH-L_2^{O2} and the influence of temperature T [°C] and CO_2 pressure [bar].[a]

Entry	T [°C]	CO_2 Pressure [bar]	Conv. [%][b]	CO_2 [%][c]	Polym. [%][d]	Yield [g][e]	Productivity [g/g][f]	M_n [Đ] [g/mol][g]
1	50	20	10.7	80	66	1.6 (±0.08)	16.3 (±0.82)	4100 [18.5]
2	60	20	14.0	79	62	1.0 (±0.05)	20.0 (±1.00)	9200 [9.8]
3	70	20	31.0	73	41	1.4 (±0.07)	27.1 (±1.36)	6900 [4.2]
4	70	30	25.5	81	53	1.6 (±0.08)	31.0 (±1.55)	7600 [6.8]
5	70	40	32.0	80	54	2.1 (±0.11)	42.0 (±2.10)	4800 [5.5]
6	80	40	54.0	77	13	1.5 (±0.08)	31.0 (±1.55)	4700 [4.6]

[a]Reaction conditions: PO (10 mL), Catalyst (0.05 g [Zn]; 160 mg LZH-L_2^{O2}), 78 h, 50 µL mesitylene as an internal standard. [b]PO conversion determined from the sum of the relative integrals in the crude ^{1}H NMR spectra of PPC (4.92 ppm), PC (77 ppm) and ether (3.46-3.32) compared to mesitylene. [c]CO_2 selectivity determined from the relative integrals in the crude ^{1}H NMR spectra of PPC (4.92 ppm) and PC (4.77 ppm) compared with ether linkages (3.46-3.32). [d]Polymer selectivity determined from the relative integrals in the crude ^{1}H NMR spectra of PPC (4.92 ppm) and PC (4.77 ppm). [e]Grams of alternating poly(propylene carbonate) determined from the crude ^{1}H NMR spectra compared with mesitylene. [f]Grams polymer/grams Zn. [g]Determined by GPC analysis, in THF, calibrated with poly(methyl methacrylate) standards.

Increasing the temperature from 50°– 70°C (at 20 bar) led to an increase in productivity (16.3 – 27.1 g/g $[Zn]_0$). CO_2-uptake remained largely constant (~70 – 80%) however, polymer selectivity decreased from 66% to 41%. The decrease in selectivity is expected as the cyclic carbonate is the thermodynamic product of epoxide/carbon dioxide coupling. To try to address the reduced polymerisation selectivity at higher temperatures, the CO_2 pressure was subsequently increased. One way that the cyclic carbonate can form is through polymer chain backbiting reactions from the alkoxide intermediate, which usually indicates issues with the carbon dioxide insertion rate.[20] Since it is unclear how the new catalysts react and the rate determining step is unknown, it is reasonable to test the notion that carbon dioxide insertion may be limiting, particularly at elevated temperatures. Increasing the pressure from 20 to 40 bar at 70 °C resulted in an improved polymer selectivity (41% – 54%) and also gave rise to a large increase in productivity (27.1 g/g $[Zn]_0$ to 42 g/g $[Zn]_0$). Increasing the temperature

further to 80 °C resulted in a significant drop in both polymer selectivity (13%) and productivity (31 g/g $[Zn]_0$). It is not reasonable to increase the pressure above 40 bar due to the likelihood of entering the sub-supercritical regime (gas expansion issues) and due to limitations in standard experimental set-up.

Polymer molecular masses ranged between 4100 and 9200 g/mol and higher temperatures seemed to narrow polymer dispersity. However, in all cases dispersity values were very broad, as is typical for surface catalysed polymerisations.

Next, attention turned to the characterisation of the catalyst before and after polymerisation. It is noted that LZH-L_2^{O2} can decompose into ZnO upon heating (>40 °C) in air at atmospheric pressure, and this was concerning given the temperatures used during the polymerisations.[6] Powder X-ray analysis shows no evidence for this decomposition, instead it indicates the retention of a layered structures after catalysis, given by the preserved in-plane reflections at 33°, 59° and 69° 2 theta, corresponding to (100), (110) and (200) respectively (**Figure 4.7**, A). However, the characteristic basal reflections (00*l*) associated with intercalated $[L_2^{O2}]^-$ were missing after catalysis. Instead, one broad reflection at ~12 2 theta [°] is observed, indicating the formation of a LZH material intercalated by carbonate anions (LZH-CO_3, **Figure 4.7**, A). A similar peak has been reported for carbonate intercalated Zn-Al layered double hydroxides.[21]

The FT-IR spectrum (**Figure 4.7**, Ba) shows a stretch at 1380 cm^{-1} which is close to the stretching mode reported at 1365 cm^{-1} for interlayer carbonate anions in Zn-Al layered double hydroxides.[21] Stretches associated with intercalated carboxylate ligand, $[L_2^{O2}]^-$, were absent after catalysis, which can be seen by comparing spectra a with b in **Figure 4.7**, where the asymmetric and symmetric stretches of CO_2^- at 1588 and 1423 cm^{-1} were missing. This indicates that the original ligands were replaced by carbonate anions and are now present as free carboxylic acid HL_2^{O2}, indicated by the C=O stretch at 1755 cm^{-1} (compare **Figure 4.7** Ba with Bc as a reference for HL_2^{O2}).

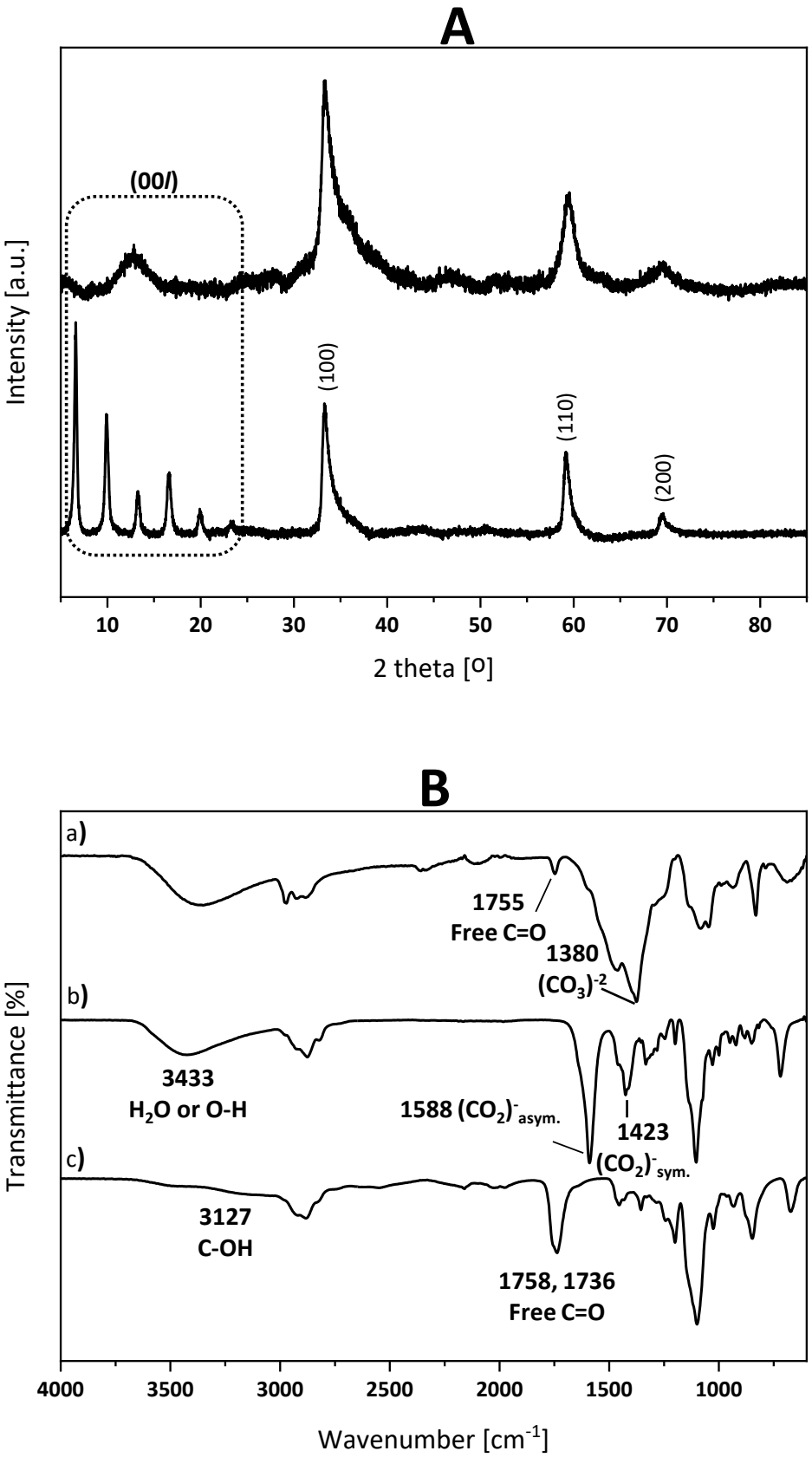

Figure 4.7. A) pXRD of LZH-L_2^{O2} before catalysis (bottom) and after catalysis (50 °C and 40 bar CO_2 pressure, top). B) FT-IR spectra of a) LZH-L_2^{O2} after catalysis, b) LZH-L_2^{O2} before catalysis and c) HL_2^{O2}. (00*l*) defines basal reflections at low 2 theta [°].

4.3.3 Effect of Catalyst Loading

Table 4.5 demonstrates the influence of catalyst loading for polymerisations conducted at 70 °C and 40 bar CO_2 pressure using LZH-L_2^{O2}.

Table 4.5. Catalytic data for the ROCOP of CO_2/PO using different loadings of the catalyst LZH-L_2^{O2}.[a]

Entry	Catalyst loading [g] Zn	Conv. [%][b]	CO_2 [%][c]	Polym. [%][d]	Yield [g][e]	Productivity [g/g][f]	M_n [Đ] [g/mol][g]
1	0.025	13	82	66	0.9 (±0.05)	37 (±1.85)	n.d.
2	0.05	32	80	54	2.1 (±0.11)	42 (±2.05)	4800 [5.5]
3	0.1	50	86	38	2.1 (±0.11)	21 (±1.05)	n.d.

[a]Reaction conditions: PO (10 mL), Catalyst (0.025 g [Zn]; 80 mg LZH-L_2^{O2}/0.05 g [Zn]; 160 mg LZH-L_2^{O2}/0.1 g [Zn]; 320 mg LZH-L_2^{O2}), 40 bar CO_2, 70 °C, 78 h, 50 µL mesitylene as an internal standard. [b]PO conversion determined from the sum of the relative integrals in the crude ^{1}H NMR spectra of PPC (4.92 ppm), PC (77 ppm) and ether (3.46-3.32 ppm) compared to mesitylene. [c]CO_2 selectivity determined from the relative integrals in the crude ^{1}H NMR spectra of PPC (4.92 ppm) and PC (4.77 ppm) compared with ether linkages (3.46-3.32 ppm). [d]Polymer selectivity determined from the relative integrals in the crude ^{1}H NMR spectra of PPC (4.92 ppm) and PC (4.77 ppm). [e]Grams of alternating poly(propylene carbonate) determined from the crude ^{1}H NMR spectra compared with mesitylene. [f]Grams polymer/grams Zn. [g]Determined by GPC analysis, in THF, calibrated with poly(methyl methacrylate) standards.

As expected, increasing the catalyst loading from 0.025 g $[Zn]_0$ to 0.1 g $[Zn]_0$ resulted in higher conversions. The polymers show very similar CO_2-uptake (82% vs. 86%). With increasing catalyst concentration, the polymer selectivity decreases (66% - 38%), resulting in lower polymer productivity. This drop in selectivity may be due to higher catalyst loadings resulting in faster reaction and, at fixed time, the polymerisation reaching higher conversions (~40-50%) which increases the solution viscosity and may hinder epoxide/carbon dioxide coordination (diffusion limitation) but does not influence the back-biting reaction (which is unimolecular).

4.3.4 COMPARING LZH-L_2^{O2} WITH ZNGA

The catalytic activity of ZnGA is known to be strongly dependent on the zinc precursor. Early reports describe the formation of ZnGA from $ZnEt_2$ and glutaric acid (GA).[15,22] Later, other zinc precursors such as $Zn(OH)_2$, $Zn(OAc)_2$, ZnO or $Zn(NO_3)_2{\cdot}6H_2O$ were found to yield ZnGA of higher activity due to improved crystallinity (for more details please refer to the introduction). To ensure fair comparisons, in this work ZnGA and LZH-L_n^{O2} (n = 2 or 5) were both compared using $ZnEt_2$ as the precursor. Compared to previous reports of this ZnGA catalyst, LZH-L_2^{O2} showed greater productivity.

Table 4.6. Comparative Polymerisation Catalysis Data for ZnGA and LZH-L_2^{O2}.

#	Precursors	Catalyst	$[Zn]_0$ [g]	PO [mL]	CO_2 [bar]	Temp. [°C]	Time [h]	Yield [g]	Pro-ductivity [g/g][f]	M_n [Đ] [g/mol][g]
1[a]	$ZnEt_2$-GA[22]	ZnGA	0.33[c]	100	52	60	40	2.5[d]	7.6[d]	11000 [11.3]
2[b]	$ZnEt_2$-HL_2^{O2}	LZH-L_2^{O2}	0.05	10	20	60	78	1.00[e]	20.0	9200 [9.8][h]
3[b]	$ZnEt_2$-HL_2^{O2}	LZH-L_2^{O2}	0.05	10	40	70	78	2.1[e]	42.0	4800 [5.5][h]

[a]Reaction conditions: Catalyst (0.33 g $[Zn]_0$; 1 g ZnGA). [b]Reaction conditions: Catalyst (0.05 g $[Zn]_0$; 160 mg LZH-L_2^{O2}), 50 µL Mesitylene as an internal standard. [C]Calculated from the weight of catalyst. [d]Calculated from the reported yield [g/g of Cat]. [e]Grams of polymer determined from the crude ^{1}H NMR spectra (with the internal standard). [f]Grams polymer/grams Zn. [g]Measured by GPC calibrated with polystyrene standards. [h]Determined by GPC analysis, in THF, calibrated with poly(methyl methacrylate) standards.

ZnGA yielded 2.5 g alternating poly(propylene carbonate) within 40 hours, at 52 bar CO_2 pressure and 60 °C. At the same temperature, LZH-L_2^{O2} yielded 1 g polymer using lower CO_2 pressure (51 vs. 20 bar). The LZH catalyst productivity is ~2.5 times greater than for ZnGA synthesised from $ZnEt_2$. Another consideration is that the LZH comprises only ~50 wt.% layered material (ZnO and $Zn(L_2^{O2})_2$ are side products of the synthesis, *vide supra*) and this makes the productivity values perhaps even greater. The optimum conditions for these LZH catalysts were at 70 °C and 40 bar CO_2 pressure which enabled isolation of ~2 g polymer and resulted in a catalytic productivity of 42 g/g $[Zn]_0$. These values are competitive with leading ZnGA catalysts, synthesised from ZnO as the metal precursor (Table 1.2 entry 8 and 9 in chapter 1).

4.4 Polymer Properties

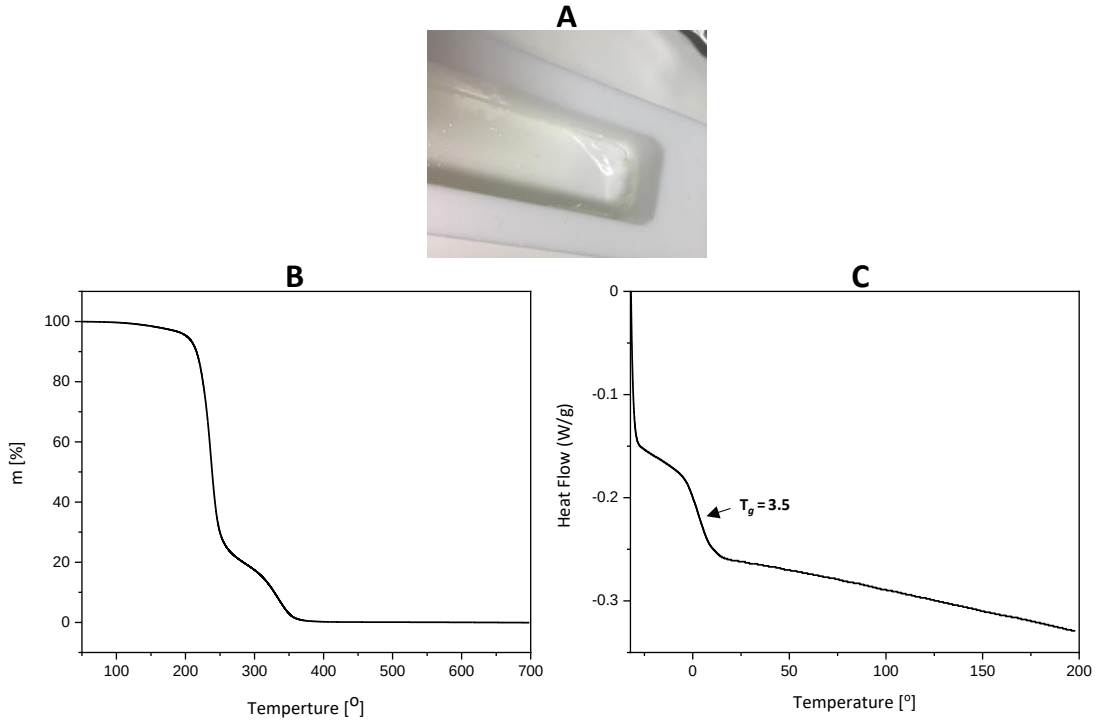

Figure 4.8. A) Polymer film in PTFE mould, B) TGA analysis and C) DSC analysis of polymer isolated with LZH-L_2^{O2} at 70 °C and 40 bar CO_2 pressure.

The polymer isolated with LZH-L_2^{O2} at 70 °C and 40 bar CO_2 pressure was found to be a fully transparent, colourless stretchy film (**Figure 4.8**, A). Its thermal stability was probed using TGA analysis, and the thermal decomposition temperature, $T_{d,5\%}$, was determined to be 200 °C (**Figure 4.8**, B). This is in reasonable agreement with other reported data on PPC.[1] The second step in the TGA profile between 300 °C and 400 °C might result from ether linkages in the isolated polymer.

The glass temperature, T_g, for PPC is reported within a relatively broad interval, generally spanning from 25 – 45 °C.[1] Factors such as different molecular weights, microstructures and the amount of ether linkages in the polycarbonate are addressed to explain the dependencies. As PPC comprising of 40–60% ether linkages and a viscosity-average molecular weight (M_v) of 41700 g/mol led to a T_g of 8 °C, the low glass temperature of 3.5 °C, measured in this study, might be due to the low molar mass of the polymer (M_n = 4800 g/mol) and high degree of ether linkages (~20%, **Figure 4.8**, C).[23]

4.5 CONCLUSION

The application of LZH materials in the ring-opening copolymerisation of CO_2 with propylene oxide is reported for the first time. Hydrophilic co-ligands such as 2-[2-(2-methoxyethoxy)ethoxy)acetate $[L_2^{O2}]^-$ was demonstrated to enhance activity compared to less hydrophilic co-ligands, $[L_3^{O2}]^-$, as a result of excellent exfoliation and therefore higher surface area. Under optimised conditions, a maximum productivity of 41 g/g $[Zn]_0$ was obtained with 40 bar CO_2 pressure at 70 °C.

This material (LZH-L_2^{O2}) proved competitive to ZnGA synthesised from $ZnEt_2$ with a reported activity of 7.6 g/g $[Zn]_0$.[22] Furthermore, the layered structure proved pivotal to activity as previous investigations into zinc-clusters by our group proved inactive for CO_2-PO ROCOP and showed poor turn-over for cyclohexene oxide.[4]

This work describes a new zinc system alongside Zn-carboxylates and Zn–Co double metal cyanide complexes. Further investigations may include using mixed metal layered structures and understanding if catalyst recycling would be possible (see Chapter 5 for more details.)

4.6 REFERENCES

[1] G. A. Luinstra, *Polym. Rev.* **2008**, *48*, 192-219.

[2] S. Klaus, M. W. Lehenmeier, E. Herdtweck, P. Deglmann, A. K. Ott, B. Rieger, *J. Am. Chem. Soc.* **2011**, *133*, 13151-13161.

[3] J. Marbach, T. Höfer, N. Bornholdt, G. A. Luinstra, *Open Chem. J.* **2019**, *8*, 828-839.

[4] K. L. Orchard, J. E. Harris, A. J. White, M. S. Shaffer, C. K. Williams, *Organometallics* **2011**, *30*, 2223-2229.

[5] A. H. M. Leung, S. D. Pike, A. J. Clancy, H. C. Yau, W. J. Lee, K. L. Orchard, M. S. P. Shaffer, C. K. Williams, *Chem. Sci.* **2018**, *9*, 2135-2146.

[6] S. A. Said, C. S. Roberts, J. K. Lee, M. S. P. Shaffer, C. K. Williams, *Adv. Funct. Mater.* **2021**, 2102631.

[7] P. Kenyon, D. J. Leung, M. Lyu, C. Chen, Z. R. Turner, J.-C. Buffet, D. O'Hare, *J. Catal.* **2021**, *402*, 94-100.

[8] F.-A. He, L.-M. Zhang, *J. Colloid Interface Sci.* **2007**, *315*, 439-444.

[9] J.-C. Buffet, N. Wanna, T. A. Arnold, E. K. Gibson, P. P. Wells, Q. Wang, J. Tantirungrotechai, D. O'Hare, *Chem. Mater.* **2015**, *27*, 1495-1501.

[10] J.-C. Buffet, Z. R. Turner, R. T. Cooper, D. O'Hare, *Polym. Chem.* **2015**, *6*, 2493-2503.

[11] N. Brown, J. Weiner, K. Hellgardt, M. Shaffer, C. Williams, *Chem. Commun.* **2013**, *49*, 11074-11076.

[12] S. D. Pike, A. García-Trenco, E. R. White, A. H. M. Leung, J. Weiner, M. S. P. Shaffer, C. K. Williams, *Catal. Sci. Technol.* **2017**, *7*, 3842-3850.

[13] O. Berkesi, I. Dreveni, J. A. Andor, J. Mink, *Inorg. Chim. Acta* **1992**, *195*, 169-173.

[14] J. Marbach, B. Nörnberg, A. Rahlf, G. Luinstra, *Catal. Sci. Technol.* **2017**, *7*, 2897-2905.

[15] M. Kobayashi, S. Inoue, T. Tsuruta, *J. Polym. Sci Polym. Chem. Ed.,* **1973**, *11*, 2383-2385.

[16] M. H. Chisholm, D. Navarro-Llobet, Z. Zhou, *Macromolecules* **2002**, *35*, 6494-6504.

[17] L. Gao, Y. Luo, Y. Lin, T. Su, R. Su, J. Feng, *J. Polym. Res.* **2015**, *22*, 1-7.

[18] J. Langanke, A. Wolf, J. Hofmann, K. Böhm, M. Subhani, T. Müller, W. Leitner, C. Gürtler, *Green Chem.* **2014**, *16*, 1865-1870.

[19] S. Foltran, E. Cloutet, H. Cramail, T. Tassaing, *J. Supercrit. Fluids* **2012**, *63*, 52-58.

[20] D. J. Darensbourg, A. D. Yeung, *Polym. Chem.* **2014**, *5*, 3949-3962.

[21] J. Liu, J. Song, H. Xiao, L. Zhang, Y. Qin, D. Liu, W. Hou, N. Du, *Powder Technol.* **2014**, *253*, 41-45.

[22] M. Ree, J. Bae, J. Jung, T. Shin, *J. Polym. Sci.,Part A: Polym. Chem.* **1999**, *37*, 1863-1876.

[23] L. Lu, K. Huang, *Polym. Int.* **2005**, *54*, 870-874.

Chapter 5:

Conclusions and Outlook

5 CONCLUSIONS AND OUTLOOK

5.1 CONCLUSIONS

Organometallic routes to produce colloidal nano-materials were studied with the long-term objective of using them as either catalyst precursors or as catalysts in CO_2 utilization for the production of fuels or polymers (polypropylene carbonate).

Stable colloidal Cu and Cu_2O nanoparticles, formed from mesitylcopper(I), were synthesised with substoichiometric amounts of bidentate ligands. The size of the nanoparticles was reproducible and ranged between 3 and 4 nm. The formation of small and stable Cu_2O nanoparticle colloids may offer the potential for integration with 3-D printing methods. Cu_2O nanoparticles showed a maximum solubilility in toluene of 200 mg/mL when coordinated by 2-[2-(2-methoxyethoxy)ethoxy]acetate. This oligoether functionalised carboxylate ligand was also useful for low temperature ligand removal from nanoparticle surfaces (at 150 °C). A series of carboxylate/dithiocarboxylate ligands were explored and exchange reactions carried out on Cu and Cu_2O nanoparticles which indirectly probed their surface properties. These studies showed for each system: a) the best ligands for producing soluble and stable nanoparticle colloids and b) indications of ligand, and substrate binding, at the nanoparticles surface during catalysis. The thiocarboxylate ligands were more strongly coordinated to metallic copper nanoparticles than carboxylate ligands, perhaps because Cu is a 'soft' metal according to Hard-Soft Lewis Acid/Base theory. Whereas, Cu_2O nanoparticles were best stabilized using carboxylate ligands.

Preliminary photocatalytic results using Cu_2O nanoparticles demonstrated some proof-of-principle activity. Cu_2O nanoparticles, homogeneously distributed within a matrix of single walled carbon nanotubes (SWCNT), were synthesised and will be tested in future as electrocatalysts. A composite catalyst consisting of Cu_2O nanoparticles mixed with a conjugated, photoactive polymer (p(^{t}Bu)TA-Ph, *vide supra*) showed promising activity in photocatalysis, producing CO. Finally, Cu_2O nanoparticles were

spray coated onto graphite electrodes, and are currently being tested as electrocatalysts with Shell Global (Amsterdam).

Exfoliated and soluble Layered Zinc Hydroxides were synthesised following a modified procedure from the literature.[1] These were tested as novel catalytic systems for the ring opening copolymerisation (ROCOP) of propylene oxide (PO) and CO_2, to produce polypropylene carbonate (PPC). When using 2-[2-(2-methoxyethoxy)ethoxy]acetate as the exfoliating ligand, a stable colloidal solution in PO was formed. This material showed the highest productivity of all the catalysts, with 41 g/g $[Zn]_0$ at 70 °C and 40 bar CO_2 pressure. Its high catalytic activity was attributed to the high catalyst surface area in solution. Solution-casting of the polymer yielded a transparent elastomeric film with a molecular weight of 4788 (g/mol^{-1}), a polydispersity of Đ = 5.53, a decomposition temperature, $T_{d,5\%}$, of 200 °C and a T_g of 3.5 °C.

5.2 Outlook

It is important to continue to develop well-controlled syntheses of copper-based nanoparticles. In particular, developing synthetic conditions which control the nanoparticle solubility, surface chemistry, size, and crystallinity are important since such factors will influence catalytic activity and surface chemistry.

The organometallic precursor may influence the size of the nanoparticles since different Cu-X bonds will show different rates of reaction during initiation (and growth). For example, $[Cu(C_6F_5)]_n$ or $[Cu\{N(SiMe_3)_2\}]_n$ are alternative precursors since their reaction with hydrogen or air will form inert side-products (HC_6F_5 and $HN(SiMe_3)$ respectively). It is also amenable to react with protic ligands, such as carboxylates. Since the reactivity of a Cu-C vs. Cu-N bond should be different, and the latter are also highly sterically congested, there could be potential to exploit size control by varying the initiation/seeding of nanoparticle precursors. It may also be possible to moderate the nanoparticle particle sizes by changing the concentration of the metallic precursor, in line with the LaMer Theory.[2]

Future work should also be directed towards a direct synthesis protocol to produce Cu_2O nanoparticles by the addition of water to a mixture consisting of any copper precursor and protic ligand precursor. This method might yield Cu_2O nanoparticles directly and thereby obviate the production of Cu nanoparticles which requires use of hydrogenation. This route would be beneficial as it would accelerate Cu_2O nanoparticles production and might scale-up more easily.

5.2.1 LIGAND DESIGN STRATEGIES ON CU AND CU_2O NANOPARTICLES

The property of colloidal nanoparticles is determined as much by their coordinated ligands as by the metal/metal oxide surfaces. Therefore, control over the surface coverage of the ligands, their electronic and steric features are important in controlling the resulting colloidal NP catalytic activity and selectivity.

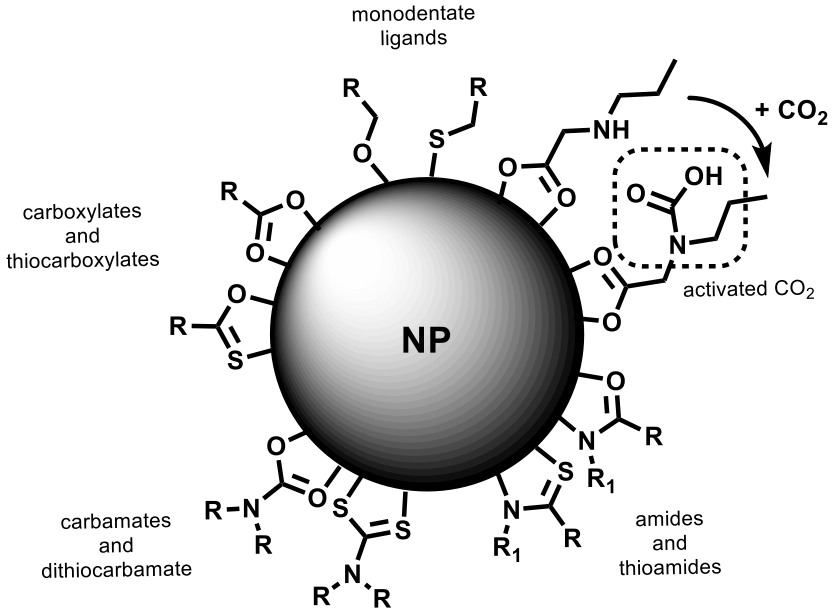

Scheme 5.1. Proposed routes to moderate ligands for Cu and/or Cu_2O nanoparticles. R = alkyl and R_1 = alkyl.

To date, the use of bidendate carboxylate or phosphinate ligands have been investigated and have produced nanoparticles with good colloidal stability.[3] In future, it's important to continue to develop such ligands, for example moderating the alkyl chain to include branched groups like 2-ethyl

hexyl or testing aromatic substituents (and moderating electro donor/acceptor properties using well-known rules). It is still an open question, the extent to which stable chelating ligands may saturate surface sites important to catalysis, thus the investigation of monodentate anionic ligands, such as alcohol or thiol groups, should be prioritised for comparative studies. It is noted that alkoxide surface capping ligands would likely be susceptible to hydrolysis and thus may be better suited to syntheses conducted under anaerobic conditions (i.e. Cu NP).

This thesis has established the potential for Cu nanoparticles coordinated by either carboxylates or dithiocarboxylates. In future, it would be interesting to investigate the use of thiocarboxylic acid ligands which feature both *O* and *S* donors. It might be expected that such ligands are compatible with Cu_2O and Cu nanoparticle surfaces. It would also be of interest to investigate other chelating, anionic donor ligands, such as carbamates, dithiocarbamates, amides and thioamides, to understand the influences of the coordinating heteroatoms and ligand electronics over nanoparticle surface properties.

As a next step, ligands or chemical functionalities that coordinate and pre-activate CO_2 could be installed to accelerate catalysis by increasing the local concentration of activated substrates at the nanoparticles surface. Commercially available N-propyl gycine is suggested as a starting point for testing this concept using Cu_2O nanoparticles. The internal amine may activate CO_2 as a carbamate group – other possible ligands featuring secondary amines could also be envisaged/bought.

5.2.2 *Cu_2O NANOPARTICLES AS CROSS LINKERS BETWEEN SWCNTS*

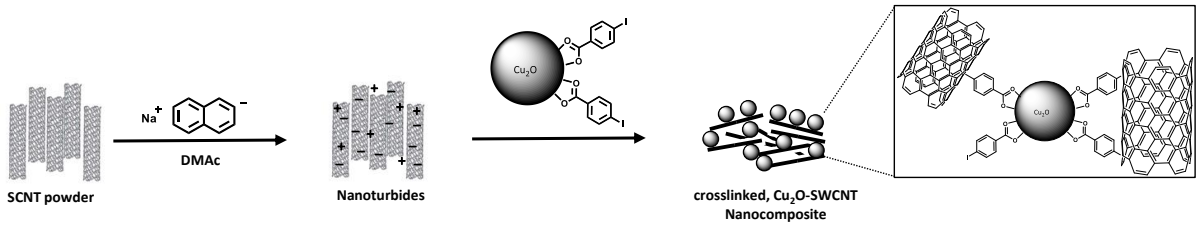

Scheme 5.2. Simplified synthesis approach to use Cu_2O nanoparticles as a cross-linker between SWCNT.

Chapter 2 reported that a Cu_2O-SWCNT nanocomposite was obtained by mixing of the cuprous oxide colloidal nanoparticles and the nanotubes. Since these composites feature a highly conductive nano-carbon and well dispersed Cu_2O catalysts, a priority should be to undertake electrochemical testing of the substrates. It will be of interest, also, to perform photoelectrochemical testing of these materials. Another future option, could be to investigate the chemical bonding between the Cu_2O nanoparticle and the nanotube. Such a strategy may inhibit any problems which could occur due to interfacial electron transfer and charge recombination. It might be possible to design a synthesis of Cu_2O nanoparticles coordinated by iodobenzoate ligands. This could be achieved using 4-iodobenzoic acid as the ligand and an organometallic synthesis route. Such iodio–functionalised nanoparticles could be covalently attached to the SWCNT using modifications to a recently reported protocol where *p*-diiodobenyene acts as the cross-linker for related SWCNT systems (**Scheme 5.2**).[4]

5.2.3 *FUTURE DIRECTIONS ON USING LZH AS A CATALYST FOR THE ROCOP OF PO AND CO_2*

Having demonstrated that LZH can be used as a catalyst for the ring opening copolymerisation of propylene oxide and CO_2, a future challenge would be to investigate catalyst stability and speciation after reaction and recycling. Powder X-ray and FT-IR analysis on the post-catalyst samples suggested the formation of carbonate intercalated LZH. It is possible that this species could still serve as polymerisation initiators or could be re-activated by exposure to more carboxylic acid ligands. Such a process would be

akin to the typical 'conditioning' treatments used to activate double metal cyanide polymerisation catalysts.

Double metal cyanide complexes based on Zn(II) and Co(III) are reported to be highly active heterogenous catalysts in the ring opening polymerisation of epoxides and CO_2.[5] Inspired by this, the synthesis of a zinc and cobalt containing layered double hydroxide material could be a useful catalyst target. Since aggregated LDH catalysts offer little advantage over existing high performance catalysts, the goal would be to make exfoliated LZH structures, doped with Co(III/II) ions. The successful organometallic route, yielding exfoliated LZH nanomaterials, should be investigated using Co(II) precursors (e.g. $Co(OAc)_2$) as a means to 'dope' cobalt into the structure. It may also be possible to introduce the exfoliating carboxylate ligand into the structure using the cobalt precursor compound (e.g. $Co(hexanoate)_2$ or $Co(2\text{-}[2\text{-}(2\text{-methoxyethoxy})ethoxy]acetate)_2$.

5.3 REFERENCES

[1] S. A. Said, C. S. Roberts, J. K. Lee, M. S. P. Shaffer, C. K. Williams, *Adv. Funct. Mater.* **2021**, 2102631.
[2] S. Arshadi, J. Moghaddam, M. Eskandarian, *Korean J. Chem. Eng.* **2014**, *31*, 2020-2026.
[3] S. D. Pike, E. R. White, A. Regoutz, N. Sammy, D. J. Payne, C. K. Williams, M. S. P. Shaffer, *ACS Nano* **2017**, *11*, 2714-2723.
[4] M. De Marco, F. Markoulidis, R. Menzel, S. M. Bawaked, M. Mokhtar, S. A. Al-Thabaiti, S. N. Basahel, M. S. P. Shaffer, *J. Mater. Chem. A* **2016**, *4*, 5385-5389.
[5] L. Grefe, E. Mejía, *Tetrahedron* **2021**, *98*, 132433.

Chapter 6:

Experimental Section

6 EXPERIMENTAL SECTION

General procedure: All reactions were carried out using standard Schlenk techniques and/or using a glovebox operating under a nitrogen atmosphere. Unless otherwise noted, all starting materials were purchased from commercial sources and used without further purification. $ZnEt_2$ (≥52 wt% Zn basis), $AlEt_3$ (93 %), bis(pentafluorophenyl)zinc (97 %), hexanoic acid (≥ 99%) and copper(I) acetate (97%) were purchased from Sigma Aldrich, 2-(2-methoxyethoxy)acetic acid (98 %) were purchased from Fluorochem, sodium hydroxide pellets were purchased from Fisher Scientific, and zinc sulfate heptahydrate (99%) was purchased from ACS reagent. 2-[2-(2-Methoxyethoxy)ethoxy]acetic acid (technical grade) was purchased from Sigma Aldrich and distilled prior to use. Bromomesitylene (99%) was purchased from Alfa Aesar, distilled under vacuum and degassed by bubbling N_2 through the solution prior to use. Mg turnings (99 %) were purchased from Lancaster and stirred overnight under nitrogen prior to use. Propylene oxide (>99%) was purchased from Alfa Aesar, dried overnight over calcium hydride at room temperature and distilled prior to use. Mesitylene (98 %) was purchased from Sigma Aldrich, dried overnight over calcium hydride at room temperature and distilled prior to use. Carbon dioxide (BOC, 99.9 %) was dried through a drierite column and two additional drying columns (Micro Torr, Model number: MC1-804FV) in series before use in copolymerisation studies. Solvents such as toluene, THF and Et_2O were obtained from a Solvent Purification System (SPS), degassed and stored over molecular sieves (3 Å) under a nitrogen atmosphere. Acetone was dried over molecular sieves (3 Å) and distilled prior to use. Chlorobenzene was degassed prior to use. Deuterated solvents ($CDCl_3$ and C_6D_6) were dried over calcium hydride by stirring overnight at room temperature and distilled prior to use. $Zn(L_3^{O2})_2$,[1] LZH-L_4^{O2},[2] LZH-L_5^{O2},[3] $Zn(L_5^{O2})_2$[4] and $MesLi{\cdot}(Et_2O)_{0.12}$[5] were synthesised according to literature procedures. HL_1^{S2} was synthesised by Dr Bradley E. Cowie from 1-bromooctane, Mg and CS_2.

^{1}H NMR spectra were recorded on a *Bruker AVIII 400* MHz spectrometer. ^{13}C{H} NMR spectra were recorded on a *Bruker AVIII HD 500* MHz spectrometer. Chemical shifts are expressed in parts per million (ppm) and referenced relative to residual *protio*-solvent signals (^{1}H NMR: $CDCl_3$ = 7.27;

C_6D_6 = 7.16, ^{13}C NMR: $CDCl_3$ = 77.0; C_6D_6 = 128.0. NMR spectra were processed and analysed using MestReNova.

Powder X-ray diffraction (XRD) analyses was performed on dried samples on a *PANalytical Xpert PRO* diffractometer (Cu Kα radiation at 40 mA and 40 kV) with a step size of 0.033° 2θ, scan step time of 70 s and scan range of 5–90° 2Θ. For the analysis of air sensitive materials an air-tight sample holder was used. Baseline corrections and other manipulations were made using Fityk software. Scherrer equation ($\tau = \kappa\lambda/(\beta_\tau \cos(\theta))$ with $\kappa = 0.89$, β_τ as the FWHM of the target reflection and the X-ray wavelength λ with 1.54 Å for Cu Kα was used to calculate the crystallite sizes. Bragg equation ($n\lambda = 2d \cdot \cos(\theta)$) with n = 1, λ = 1.54 Å for Cu Kα, θ = scattering angle and d = interlayer distance was used to estimate interlayer distance.

UV-Vis absorption spectra were recorded on an Agilent Technologies Cary 60 UV-Vis spectrophotometer using a Young's tap quartz cuvette.

Scanning electron microscopy (SEM) images and energy disperse X-ray (EDX) analysis were obtained on a *JEOL JSM 6010 LA* at Imperial College London by mounting the sample onto stubs using carbon tape and sputtered with gold.

Thermogravimetric analyses (TGA) were carried out using *Mettler Toledo TGA/DSC 1 STAR* or *TA TGA5500* with a heating rate of 10 °C/min in air, flowing at 100 mL/min.

FT-IR measurements were obtained for dried samples on either a *Perkin-Elmer 100* Spectrometer (Chapter 1) or a *Shimadzu IRSpirit* spectrometer (installed inside the glove box) using a single reflection ATR accessory.

For differential scanning calorimetry, a *TA DSC25* was used under a N_2 flow (100 mL/min). Samples were heated, at a rate of 20 °C/min, from –80 to 200 °C. Glass transition temperatures (T_g) were determined from the midpoint of the transition of the second heating curve.

X-ray photoelectron spectroscopy (XPS) was performed on a *Thermo Scientific K-Alpha X-ray photoelectron* spectrometer system operating at $1x10^{-8}$ mbar base pressure. This system incorporates a monochromated, microfocused Al Kα X-ray source (hν = 1486.6 eV) and a 180° double focusing hemispherical analyser with a 2D detector. An X-ray spot size of 400 µm was used and the X-ray source was operated at 6 mA emission current and 12 kV anode bias. A flood gun was used to minimise sample charging. Samples were mounted using conductive carbon tape and transferred to the spectrometer using a special glove box module which ensured that samples were never exposed to air. Data were collected at 200 eV pass energy for survey, 20 eV pass energy for core level and 15 eV pass energy for valence spectra. All data were analysed using the Avantage software package and performed by Dr Anna Regoutz (University College London).

Gel permeation chromatography analysis was conducted using an *Agilent Infinity II MDS* instrument, with two PLgel mixed C columns (300 x 7.5 mm) and a PLgel 5 µm guard column. The eluent was THF and 0.01 % BHT (butylated hydroxytoluene) additive. Samples were run at 1 mL/min at 30 °C. Poly(methyl methacrylate) was used for calibration. Samples were analysed by Dr Daniel Lester at Warwick Scientific Services.

Elemental analysis was performed by either Dr Nigel Howard at the Microanalysis in Cambridge or Stephen Boyer at the London Metropolitan University.

6.1 CHAPTER 2

In order to synthesise colloidal Cu@L_n^{X2} (n = 1, 2; X = S, O) it was important to remove any O_2 or moisture from the H_2 Schlenk line prior to use. Heating both manifolds of the H_2 Schlenk line with a heat gun whilst under dynamic vacuum, followed by applying dynamic vacuum overnight, and bubbling hydrogen gas through for 30 minutes prior to use, was effective for removing potential moisture from the line.

Synthesis of Cu@L_1^{X2} (X = O or S). A solution of the appropriate acid HL_1^{X2} (28.5 mg of HL_1^{O2} or 17.1 mg of HL_1^{S2}, 0.18 mmol) in toluene (40 mL) was added to a solution of CuMes (329 mg, 1.8 mmol) in toluene (10 mL) into a Young's tap ampoule. The solution was degassed by three freeze-pump-thaw cycles and then frozen at –196 °C. H_2 (1 bar) was introduced while the solution was frozen and fully submerged in liquid N_2, which gives rise to a pressure of 3 bar. The sealed reaction vessel was allowed to warm to room temperature before being heated for 2.5 h in a 110 °C pre-heated oil bath. The solution was then allowed to cool to room temperature and the excess H_2 was removed by quickly exposing the system to vacuum (x3), ensuring not to remove any solvent. The colloidal solution of Cu@L_1^{X2} was dried under reduced pressure. The remaining residue was dissolved in a minimal volume of toluene, and the desired Cu@L_1^{X2} nanoparticles were precipitated from solution through the addition of excess acetone. The resulting suspension was centrifuged at 3000 rpm for 30 minutes. The supernatant was decanted off and the nanoparticles were re-dissolved in toluene and evaporated to dryness under reduced pressure. Powder X-ray diffraction shows expected peaks for metallic copper (2θ (°) = 44, 51 and 74; JCPDS 01-085-1326) with an estimated particle size of 3.2 nm for Cu@L_1^{O2}, and 3.0 nm for Cu@L_1^{S2} nm (Scherrer equation). FT-IR [cm^{-1}] Cu@L_1^{O2} 2924 (ν CH), 1421,1410 ($\nu_{asym}CO_2^-$) and 1306 ($\nu_{sym.}CO_2^-$), Cu@L_1^{S2} 2920 (ν CH), 1044,1011 ($\nu_{asym.}CS_2^-$) and 847 ($\nu_{sym.}CS_2^-$). UV-Vis [nm] Cu@L_1^{O2} SPR at 567, L_1^{S2} SPR at 586.

Synthesis of Cu@L_2^{O2}: A solution of HL_2^{O2} (32.1 mg, 0.18 mmol) in toluene (40 mL) was added to a solution of CuMes (329 mg, 1.8 mmol) in toluene (10 mL) into a Young's tap ampoule. The solution was

degassed by three freeze-pump-thaw cycles and then frozen at –196 °C and left under high vacuum. H_2 (1 bar) was introduced while the solution was frozen and fully submerged in liquid N_2, which gives rise to a pressure of 3 bar. The sealed reaction mixture was allowed to warm to room temperature before being heated for 2.5 h in a 110 °C pre-heated oil bath. The solution was then allowed to cool to room temperature, and excess H_2 was removed by quickly exposing the system to vacuum (x3), ensuring not to remove any solvent. The colloidal solution of Cu@L_2^{O2} was dried under reduced pressure and used as such. Note: The polar ligand chain does not allow reprecipitation from a toluene solution with excess acetone. Powder X-ray diffraction shows expected peaks for metallic copper (2θ (°) = 44, 51 and 74; JCPDS 01-085-1326) with an estimated particle size of 3.1 nm for Cu@L_2^{O2}. FT-IR [cm^{-1}] 2877 (ν CH), 1425 ($\nu_{asym.}CS_2^-$) and 1408 ($\nu_{sym.}CS_2^-$). UV-Vis [nm] SPR at 567.

Synthesis of $Cu_2O@L_1^{O2}$ in Air. A freshly prepared 36 mM solution of crude Cu@L_1^{O2}, prepared as described above, was exposed to air and stirred at room temperature overnight. The original deep red colloidal solution turns green and remains colloidal. The colloidal solution of $Cu_2O@L_1^{O2}$ was dried under reduced pressure and the remaining residue was isolated by re-dissolving in toluene and precipitating the desired $Cu_2O@L_1^{O2}$ with excess acetone. The resulting suspension was centrifuged at 3000 rpm for 30 minutes, yielding the desired nanoparticles as a dark black coloured solid. The supernatant was decanted off and the remaining nanoparticles were re-dissolved in toluene and dried under reduced pressure. Powder X-ray diffraction shows expected peaks for cuprous oxide (2θ (°) = 30, 37, 42, 53, 61, 74, 78; JCPDS 05-0667) with an estimated particle size of 2.4 nm for $Cu_2O@L_1^{O2}$ (Scherrer equation). FT-IR [cm^{-1}] 3390 (ν H_2O or OH, br), 2922 (ν CH), 1541, 1429 ($\nu_{asym}CO_2^-$) and 1313 ($\nu_{sym.}CO_2^-$).

Synthesis of $Cu_2O@L_1^{O2}$ with O_2. The nitrogen headspace of a freshly prepared 36 mM solution of Cu@L_1^{O2} was exchanged for O_2 at room temperature by flushing the headspace for 10 minutes with O_2. The reaction mixture stirred overnight at room temperature. The original deep red colloidal solution turned dark green/turquoise within seconds and remained colloidal. Powder X-ray diffraction shows expected peaks for cuprous oxide (2θ (°) = 30, 37, 42, 53, 61, 74, 78; JCPDS 05-0667) with an estimated

particle size of 2.4 nm for $Cu_2O@L_1^{O2}$ (Scherrer equation). FT-IR [cm^{-1}] 3390 (ν H_2O or OH, br), 2922 (ν CH), 1541, 1429 ($\nu_{asym.}CO_2^-$) and 1313 ($\nu_{sym.}CO_2^-$).

Synthesis of $Cu_2O@L_2^{O2}$ in Air. A freshly prepared 36 mM solution of crude $Cu@L_2^{O2}$, prepared as described above, was exposed to air and stirred at room temperature overnight. The original deep red colloidal solution turns green and remains colloidal. The colloidal solution of $Cu_2O@L_2^{O2}$ was dried under reduced pressure and used as such as the polar nature of the ligand chain did not allow precipitation from toluene with acetone. The desired nanoparticles were obtained as a dark black coloured solid. Powder X-ray diffraction shows expected peaks for cuprous oxide (2θ (°) = 30, 37, 42, 53, 61, 74, 78; JCPDS 05-0667) with an estimated particle size of 3.2 nm for $Cu_2O@L_2^{O2}$ (Scherrer equation). FT-IR [cm^{-1}] 3462 (ν H_2O or OH, br), 2919 (ν CH) and 1589 ($\nu_{asym}CO_2^-$) and 1409 ($\nu_{sym.}CO_2^-$).

Synthesis of $Cu_2O@L_2^{O2}$ with O_2. The nitrogen headspace of freshly prepared 36 mM solution of $Cu@L_2^{O2}$ was exchanged for O_2 at room temperature by flushing the headspace for 10 minutes with O_2. The reaction mixture stirred overnight at room temperature. The original deep red colloidal solution turned dark green/turquoise within seconds and remained colloidal. Powder X-ray diffraction showed the expected peaks for cuprous oxide (2θ (°) = 30, 37, 42, 53, 61, 74, 78; JCPDS 05-0667) with an estimated particle size of 3.8 nm (Scherrer equation). FT-IR [cm^{-1}] 3462 (ν H_2O or OH, br), 2872 (ν CH) and 1589 ($\nu_{asym}CO_2^-$) and 1409 ($\nu_{sym.}CO_2^-$).

Attempted Synthesis of $Cu_2O@L_1^{S2}$ in Air. A freshly prepared 36 mM solution of crude $Cu@L_1^{S2}$, prepared as described above, was exposed to air and stirred at room temperature overnight. The original deep red colloidal solution turned black and a precipitate formed. No colloidal solution was obtained.

$Cu@(L_1^{O2})_{0.1}$ + 0.1 equiv. HL_1^{S2}: HL_1^{S2} (7.2 mg, 0.038 mmol) was added to $Cu@(L_1^{O2})_{0.1}$ (30 mg, 0.38 mmol) in toluene (10 mL) at room temperature. The mixture was stirred for 1 h inside the glove box at room temperature before dried under reduced pressure and analysed by UV-Vis and FT-IR spectroscopy.

Cu@(L_1^{S2})$_{0.1}$ + 0.1 equiv. HL_1^{O2}: HL_1^{O2} (5.7 mg, 0.036 mmol) was added to Cu@(L_1^{S2})$_{0.1}$ (30 mg, 0.36 mmol) in toluene (10 mL) at room temperature. The mixture was stirred for 1 h under inert atmosphere at room temperature before dried under reduced pressure and analysed by UV-Vis and FT-IR spectroscopy.

Cu@(L_1^{S2})$_{0.1}$ + 0.5 equiv. HL_1^{O2}: HL_1^{O2} (28.5 mg, 0.180 mmol) was added to Cu@(L_1^{S2})$_{0.1}$ (30 mg, 0.36 mmol) in toluene (10 mL) at room temperature. The mixture was stirred for 1 hour under inert atmosphere at room temperature before dried under reduced pressure and analysed by UV-Vis and FT-IR spectroscopy.

Cu_2O@(L_1^{O2})$_{0.1}$ + 0.1 equiv. HL_1^{S2}: HL_1^{S2} (3.6 mg, 0.019 mmol) was added to Cu_2O@(L_1^{O2})$_{0.1}$ (30 mg, 0.19 mmol) in toluene (10 mL) at room temperature. The mixture was stirred for 1 hour under an inert atmosphere at room temperature before being dried under reduced pressure and analysed by UV-Vis and FT-IR spectroscopy.

Solubility test: Freshly prepared, crude, colloidal solutions of $Cu_2O@L_n^{O2}$ (n = 1 or 2) were dried under reduced pressure, yielding nanoparticles as dark black solids. The corresponding nanoparticles (20-250 mg) were re-dissolved in 1 mL of either toluene, tetrahydrofuran, acetone or methanol followed by gently stirring. The resulting saturated supernatants were decanted off from undissolved residuals after standing for 2 h. The solubility limit [mg/ml^{-1}] was determined by removing 0.5 mL of the saturated colloidal nanoparticle solution and evaporating to dryness under reduced pressure in a pre-weighed vial.

Deposition of Crosslinked SWCNT film and Cu_2O infusion: (carried out by David M Stringer at Imperial College of London). *p*-Diiodobenzene (1 mg, 0.003 mmol) was dissolved in minimal amount of DMAc and added to carbon nanotubide (1.8 $_{mgSWCNTs}$ $mL_{DMAc\text{-}1}$) (200 µL), giving equimolar quantities of crosslinker to Na. 100 µL of this gelling nanotubide was then promptly drop cast (using a 200 µL micropipette), onto pre-silanised glass substrates (26 x 26 mm). The substrate was stored within a DMAc saturated atmosphere (formed by covering the wall of a glass jar with a sheet of filter paper soaked in

DMAc), for 18 h. $Cu_2O@L_2^{O2}$ nanoparticles, suspended in toluene (100 uL, 36 mM), were then drop cast onto the surface of the SWCNT film and left to infuse for a further 24 h. The film was removed from the glovebox in a sealed vacuum flask and residual charge quenched by injection of dry oxygen gas (20% balance nitrogen) through a suba seal. The film was then subjected to a series of solvent exchanges through submersion (MeOH, IPA/water (50/50), acetone), before supercritical drying with liquid CO_2.

Sample preparation for photocatalytic testing or Cu_2O nanoparticles: $Cu_2O@L_2^{O2}$ nanoparticles, suspended in toluene (36 mM), were drop cast onto a pre-weighed glass slide (1.5 x 1 cm) and dried in air. The process was repeated until 2 mg of dried sample was deposited on the glass slide. The annealed sample was prepared the same way followed by thermal ligand removal at 150 °C for 30 minutes in air.

Synthesis of 5wt% $Cu_2O@(L_2^{O2})$-p(^{t}Bu)TA-Ph nanocomposite and sample preparation for photocatalytic testing : (carried out by Floriana Moruzzi, University of Oxford). 3 mg of p(^{t}Bu)TA-Ph were dissolved in a minimum amount of chloroform together with 10 uL of a colloidal solution of $Cu_2O@L_2^{O2}$ in chlorobenzene (36 mM), drop casted onto a glass slide (1.5 x 1 cm) and dried in air.

Photocatalytic testing: (carried out by Floriana Moruzzi, University of Oxford). The photocatalytic testing was carried out using a home-built photocatalytic gas phase set-up with a reactor volume of 25 mL and a 5 cm^2 quartz window for illumination with a 300 W Xe lamp equipped with 1.5 AM filter. Samples were inserted in the reactor and left under vacuum for 1 hour, followed by a purge with hydrogen gas at a flow rate of 10 sscm for 1 hour. Then a 3:1 H_2 to CO_2 gas mixture was flowed through for 30 minutes before the reactor was shut to build up a pressure of 1.5 bar. The measurements were taken in batch at an overpressure of 1.5 bar and released gasses injected into the GC (Agilent 8860 equipped with a jetanizer on the FID and TCD detector).

6.2 CHAPTER 3

Attempts to synthesise ZnAl LDH with a Zn:Al ratio of 3:1: A 0.5 M solution of $ZnEt_2$ in toluene and a 0.5 M solution of $AlEt_3$ in toluene was added dropwise to a 0.5 M solution of 2-(2-methoxyethoxy)acetic acid (HL_4^{O2}) in toluene (see **Table 6.1** for the quantities added). The reaction mixture was stirred for 16 h, at room temperature, under an N_2 atmosphere. Under a flow of N_2, HPLC-grade degassed water (35 µL, 1.94 mmol) was slowly added and the formation of a white solid was observed immediately. The reaction mixture was stirred for another 3 h, and the solvent was removed, under reduced pressure, to afford a white powder.

Table 6.1. Amounts of HL_4^{O2}, $ZnEt_2$, $AlEt_3$, toluene and degassed water used to attempt the synthesis of ZnAl LDHs.

Carboxylate loading $[HL_4^{O2}]/[Zn][Al]$	HL_4^{O2} (0.5 M in C_7H_8) [mmol]/[mL]	$ZnEt_2$ (0.5 M in C_7H_8) [mmol]/[mL]	$AlEt_3$ (0.5 M C_7H_8) [mmol]/[mL]	C_7H_8 [mL]	H_2O [mmol]/[µL]
0.25	0.46/0.92	1.38/2.76	0.46/0.92	6.56	1.94/35
0.3	0.55/1.10	1.38/2.76	0.46/0.92	6.38	1.94/35
0.35	0.65/1.29	1.38/2.76	0.46/0.92	6.19	1.94/35
0.4	0.74/1.47	1.38/2.76	0.46/0.92	6.00	1.94/35
0.6	1.10/2.21	1.38/2.76	0.46/0.92	5.27	1.94/35

Synthesis of CuMes: This methodology was modified from a literature procedure.[6] Bromomesitylene (7.5 mL, 49 mmol) was added dropwise to a suspension of Mg turnings (1.5 g, 60.5 mmol) in THF (30 mL) at 0 °C. After 1 h, the water/ice bath was removed and the mixture was stirred for an additional 4 h, forming a brown solution with some black Mg powder remaining unreacted. CuCl (5.5 g, 55.6 mmol) was suspended in THF (30 mL) and the MesMgBr solution was added dropwise over the course of 10 minutes *via* cannula at –35 °C. The reaction was allowed to warm to room temperature and stirred overnight. 1,4-Dioxane (20 mL) was added and the mixture stirred for 30 min, affording a yellow solution with a grey precipitate. The mixture was allowed to settle for 30 min before being filtered *via* cannula and washed through with additional THF (20 mL). The yellow solution was evaporated to dryness under reduced pressure, affording a yellow powder. This was dissolved in a

minimum volume of hot (80 °C) toluene (approx. 20 mL), and the solution was filtered *via* filter cannula while hot into a Schlenk flask and allowed to crystallise in the freezer (–35 °C). CuMes crystallised as yellow/orange crystals over several days, which were isolated *via* filter cannula, washed with cold toluene (3 x 3 mL) and dried under reduced pressure. The supernatant and washings were collected, concentrated and placed in the freezer for several weeks, affording a second batch of yellow/orange crystals that were worked-up identically to the first. Total yield across two batches was 5.90 g (32.3 mmol, 59.4%) which was stored in the freezer in the glovebox. In solution, CuMes exists as a mixture of dimeric and pentameric species. ^{1}H NMR (C_6D_6, 400 MHz): δ 1.90 (s, 3H, *para*-$CH_3^{pentamer}$), 2.02 (s, 3H, *para*-CH_3^{dimer}), 2.93 (s, 6H, *ortho*-$CH_3^{pentamer}$), 2.93 (s, 6H, *ortho*-CH_3^{dimer}), 6.59 (s, 2H, $CH^{pentamer}$), 6.67 (s, 2H, CH^{dimer}).

Synthesis of Cu(L_3^{O2})$_2$: Oleic acid HL_3^{O2} (1.58 mL, 5.0 mmol), $Cu(Ac)_2{\cdot}H_2O$ (0.45 mL, 2.5 mmol) and toluene (100 mL) were heated to 150 °C. Upon boiling, a mixture of water, acetic acid, and toluene was azeotropically distilled for 5 h. The remaining toluene was removed under reduced pressure, yielding a viscous green/blue residue. The residue was dissolved in ethanol and water was added causing an oily precipitation after letting it sit at room temperature overnight. The top solution was decanted off and the residue was re-dissolved in toluene. The organic phase was dried over $MgSO_4$, filtered and concentrated. $Cu(L_3^{O2})_2$ was isolated as a sticky blue solid in 53 % yield. Melting point: 164 °C. Elemental analysis: $C_{36}H_{66}O_4Cu$ C, 69.02; H, 10.62; found C, 68.81; H, 10.30.

Attempts to synthesise Zn(L_4^{O2})$_2$: *Attempt 1* – NaOH (0.35 g, 8.8 mmol) was added to a solution of 2-(2-methoxyethoxy)acetic acid HL_4^{O2} (1mL, 8.8 mmol) in 70 mL of ethanol. The reaction mixture was stirred at 50 °C for 1 h. $ZnCl_2$ (0.6 g, 4.4 mmol) in water (111 mL) was added slowly and the reaction mixture stirred for 1 h at 50 °C before it was dried under reduced pressure, yielding a sticky solid. All efforts to isolate the desired $Zn(L_4^{O2})_2$ proved to be unsuccessful.

Attempt 2 – $Zn(OH)_2$ was freshly prepared by slowly adding a 1 M solution of NaOH (52 mL) to $ZnSO_4{\cdot}7H_2O$ (7.5 g, 26.1 mmol) in Milli-Q water (100 mL). The reaction mixture was stirred for 1 h at

room temperature, affording an off-white coloured precipitate, which was filtered and washed with water and isopropanol. The white powder was then dried in air overnight. Next, HL_4^{O2} (5.2 mL, 45.3 mmol) was added to a suspension of $Zn(OH)_2$ (1.5 g, 15.1 mmol) in *n*-octane (50 mL). The reaction mixture was heated for 2 h at 130 °C, yielding a brownish oil. However, the desired $Zn(L_4^{O2})_2$ could not be isolated.

Synthesis of ZnMes₂: A solution of mesityllithium (0.45 g, 3.3 mmol, 2 eq.) in THF (5 mL) was added dropwise to a solution of $ZnBr_2$ (0.37 g, 1.6 mmol, 1 eq.) in THF (15 mL) at room temperature, and the reaction was stirred overnight. The translucent mixture was dried and extracted with toluene. The solution was filtered *via* syringe filter and concentrated under reduced pressure. The desired compound was crystallised at –25 ˚C overnight, affording colourless needles. The supernatant was decanted off and the needles were washed with cold toluene. Crystals suitable for single crystal X-ray diffraction were grown from a concentrated toluene solution of $Zn(Mes)_2$ in toluene at –25 ˚C. ^{1}H NMR (400 MHz, C_6D_6): δ [ppm] 6.83 (s, 2H; Ar-*H*), 2.39 (s, 6H; *o*-CH_3), 2.24 (s, 3H; *p*-CH_3). $^{13}C\{^1H\}$ NMR (100 MHz, C_6D_6): δ [ppm] 148.61, 145,29, 138.21, 126.65, 26.95, 21.46.

Synthesis of LZH-L₄^O2 from Zn(Mes)₂: 2-(2-Methoxyethoxy)acetic acid (68 µL, 0.6 mmol) was added dropwise to a suspension of $Zn(Mes)_2$ (0.3 g, 1 mmol) in 10.6 mL of toluene, yielding a clear solution. The reaction mixture was stirred at room temperature overnight. Under a flow of N_2, HPLC-grade degassed water (28.8 µL, 1.6 mmol) was slowly added and the reaction mixture was stirred for 3 h, which yielded a milky, translucent solution. The solvent was removed under reduced pressure and a pale-coloured powder was obtained. The powder X-ray diffraction pattern was in agreement with data reported in the literature for LZH-L_4^{O2}.[2]

Synthesis of LZH-L₃^O2 from Zn(C₆F₅)₂: $Zn(L_3^{O2})_2$ (880 mg, 0.14 mmol) was added to $Zn(C_6F_5)_2$ (130 mg, 0.33 mmol) in toluene (3.1 mL). The reaction mixture was stirred at room temperature overnight, yielding a milky, translucent solution. Under a flow of N_2, HPLC-grade degassed water (13.4 µL, 0.8 mmol) was slowly added and the reaction mixture stirred at room temperature overnight.

After drying the reaction mixture under reduced pressure, a white solid was isolated. The powder X-ray diffraction pattern was in agreement with data reported in the literature for LZH-L_3^{O2}.[3]

Attempts to synthesise Cu^{I}_{x}LZH: The Zn and Cu precursors were dissolved in toluene (Table 6.2), and the reaction mixture was stirred overnight at room temperature. Under a flow of N_2, HPLC-grade degassed water was added slowly and the reaction mixture stirred for an additional 12 hours at room temperature. The resulting translucent yellow/orange solution was dried under reduced pressure, yielding a sticky yellow/orange solid.

Table 6.2. Amounts of Zn precursor, Cu precursor, toluene and HPLC-grade degassed water used to attempt the synthesis of $Cu^{m}_{xMol\%}$LZH-L_3^{O2} (m = I or II).'*' 1 M CuMes in toluene.

	Zn-Precursor		Cu-Precursor		Toluene	HPLC-grade H_2O
	ZnR_n	$Zn(L_3^{O2})_2$	CuR_3	$Cu(L_3^{O2})_2$		
$Cu^{I}_{5Mol\%}$LZH-L_3^{O2}; n = 3	274.7 mg, 0.9 mmol	261.4 mg, 0.42 mmol	8.7 mg, 0.05 mmol	-	14 mL	39.4 µL, 1.6 mmol
$Cu^{I}_{7.5Mol\%}$LZH-L_3^{O2}; n = 3	245.8 mg, 0.81 mmol	239.0 mg, 0.41 mmol	71.4 µL* 0.07 mmol	-	13 mL	37.1 µL, 1.6 mmol
$Cu^{I}_{10Mol\%}$LZH-L_3^{O2}; n = 3	239.0 mg 0.79 mmol	239.0 mg, 0.41 mmol	91.5 µL* 0.09 mmol	-	13 mL	37.1 µL, 1.6 mmol
$Cu^{I}_{10Mol\%}$LZH-L_3^{O2}; n = 4	314.3 mg, 0.79 mmol	239.0 mg, 0.41 mmol	91.5 µL* 0.09 mmol	-	13 mL	37.1 µL, 1.6 mmol
$Cu^{II}_{5Mol\%}$LZH-L_3^{O2}; n = 3	275 mg, 0.9 mmol	231 mg, 0.37 mmol	-	29.8 mg, 0.9 mmol	20 mL	39.4 µL, 2.2 mmol
$Cu^{II}_{10Mol\%}$LZH-L_3^{O2}; n = 3	72 mg, 0.24 mmol	59 mg, 0.1 mmol	-	6.5 mg, 0.01 mmol	7 mL	9.7 µL, 0.54 mmol
$Cu^{II}_{15Mol\%}$LZH-L_3^{O2}; n = 3	72 mg, 0.24 mmol	56 mg, 0.09 mmol	-	9.8 mg, 0.016 mmol	9 mL	9.7 µL, 0.54 mmol
$Cu^{II}_{20Mol\%}$LZH-L_3^{O2}; n = 3	72 mg, 0.24 mmol	52.3 mg, 0.08 mmol	-	13 mg, 0.02 mmol	9 mL	9.7 µL, 0.54 mmol

6.3 CHAPTER 4

CO_2/Epoxide Co-polymerisations: The individual reaction mixtures comprising of catalyst, propylene oxide and mesitylene (if used as an internal standard) were stirred for 30 minutes in the glovebox before being transferred to either a Parr 5500 HP Compact Reactor (25 mL or 100 mL) for reactions requiring 10-40 bar of CO_2 pressure, or an ampule equipped with a Young's tap for reaction requiring 1 bar of CO_2 pressure. The nitrogen headspace of the reactors/ampoule was exchanged with CO_2, partially pressurised to half of the aimed CO_2 pressure [bar], heated to the desired temperature and finally brought to full pressure. The polymerisations were conducted under a static CO_2 pressure and were quenched after 78 h by placing the reaction vessel into an ice bath; the pressure was released once cooled to room temperature. The crude reaction mixture was analysed by ^{1}H NMR spectroscopy, and the polymers isolated by precipitation of a CH_2Cl_2 solution into cold pentane. GPC, TGA and DSC data was collected for purified samples. The polymeric film was obtained by dissolving the isolated polymer in $CHCl_3$. The concentrated solution of polymer was then poured into a PTFE mould, which was left at room temperature for 20 h to allow the solvent to evaporate slowly.

Synthesis of ZnO@L_5^{O2}: $ZnEt_2$ (1.28 g, 10.35 mmol) was added dropwise to hexanoic acid (HL_5^{O2}, 120.24 mg, 1.04 mmol) in toluene (69 mL) and stirred for 2 h at room temperature. A solution of HPLC grade degassed water in dry acetone was added slowly to the precursor solution. The reaction mixture was stirred for a further 2 h before being centrifuged for 15 min at 3000 rpm. The supernatant was decanted off, and the remaining residue was re-suspended in toluene and precipitated with acetone three times. The isolated white solid was then dried for 3 h under reduced pressure. Powder X-ray diffraction showed the expected peaks for zinc oxide (2θ (°) = 32, 34, 37, 48, 57, 63, 67, 68, 69, 73, 77, 82, 90, 93, 96, 98, 104, 107, 110, 116; JCPDS 00-001-1136). FT-IR [cm^{-1}] 3387 (ν H_2O and OH), 2917 (ν C-H), 1544, 1399 ($\nu_{asym.}CO_2^-$).

Synthesis of LZH-L_2^{O2}: The synthesis was scaled up and modified from a literature procedure.[2] $ZnEt_2$ (2.5 g, 20.2 mmol) was added dropwise to 2-[2-(2-Methoxyethoxy)ethoxy]acetate, (HL_2^{O2}, 2.16 mg, 12.15 mmol) in toluene (135 mL) and stirred over night at room temperature. The reaction mixture was cooled in a water-ice bath prior to the addition of HPLC grade degassed water (583.52 µL, 32.4 mmol) under a flow of nitrogen. Once the addition was complete the cooling bath was removed and the reaction mixture was allowed to warm to room temperature. After stirring overnight, the solvent was removed under reduced pressure and LZH-L_2^{O2} was isolated as a sticky white solid. The powder X-ray diffraction pattern was in agreement with data reported in literature for LZH-L_2^{O2}.[2] FT-IR [cm^{-1}] 3429 (ν H_2O and OH), 2870 (ν C-H), 1589 ($\nu_{asym.}CO_2^-$), 1414 ($\nu_{sym.}CO_2^-$), 1103 (COC).

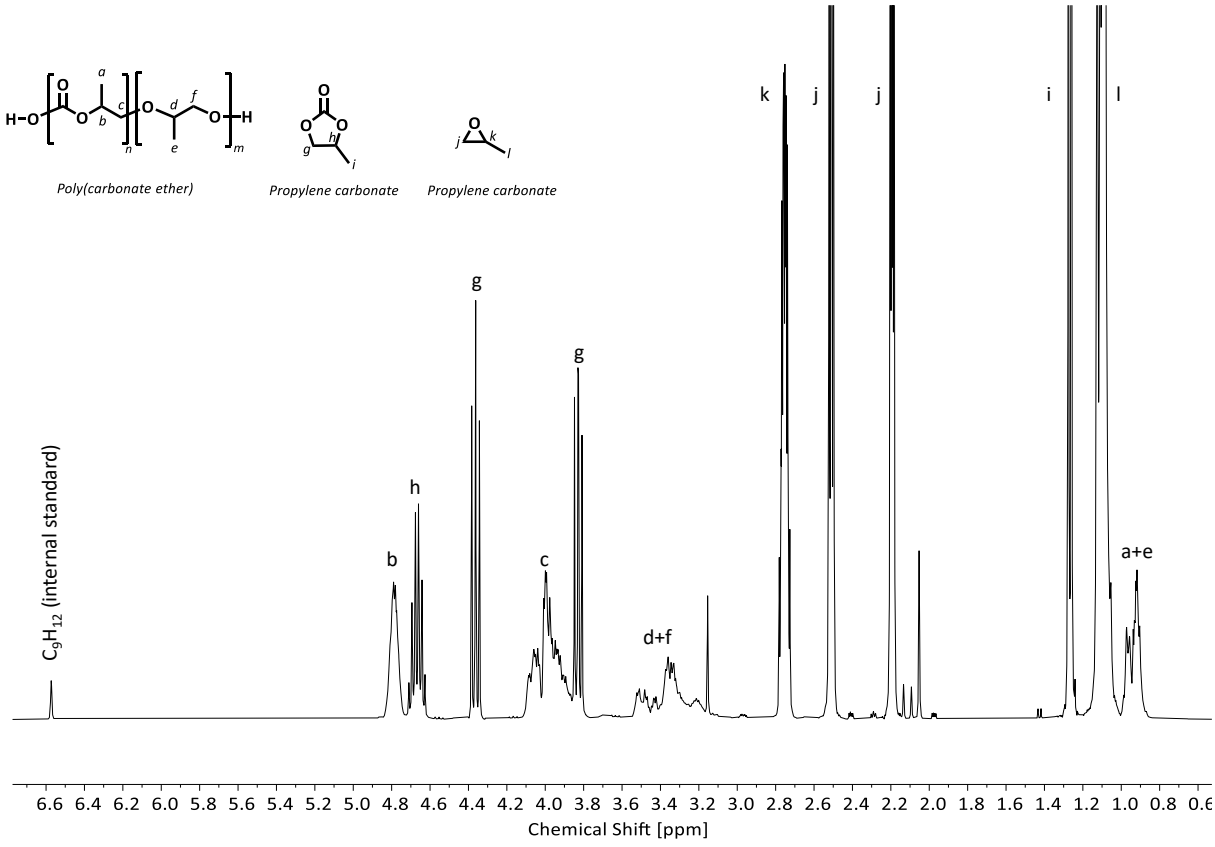

Figure 6.1. Representative example of crude ^1H NMR spectrum of a typical PO-CO_2 ring opening copolymerisation formation both poly(carbonate ether) and propylene carbonate. Mesitylene is used as an internal standard.

6.4 REFERENCES

[1] S. Barman, S. J. T. J. o. P. C. B. Vasudevan, *J. Phys. Chem. B* **2007**, *111*, 5212-5217.
[2] S. A. Said, C. S. Roberts, J. K. Lee, M. S. Shaffer, C. K. J. A. F. M. Williams, **2021**, 2102631.
[3] A. H. M. Leung, S. D. Pike, A. J. Clancy, H. C. Yau, W. J. Lee, K. L. Orchard, M. S. P. Shaffer, C. K. Williams, *Chem. Sci.* **2018**, *9*, 2135-2146.
[4] O. Berkesi, I. Dreveni, J. Andor, J. J. I. c. a. Mink, **1992**, *195*, 169-173.
[5] J. E. Borger, M. S. Bakker, A. W. Ehlers, M. Lutz, J. Chris Slootweg, K. Lammertsma, *Chem. Commun.* **2016**, *52*, 3284-3287.
[6] E. M. Meyer, S. Gambarotta, C. Floriani, A. Chiesi-Villa, C. J. O. Guastini, *Organometallics* **1989**, *8*, 1067-1079.

Chapter 7:

Appendix

7.1 LICENSES FOR REPRODUCING FIGURES